Distributed Protocols, Nonlinear State-Dependent Networks, and Human-Swarm Interactions

Eric Alan Schoof

A dissertation

submitted in partial fulfillment of the

requirements for the degree of

Doctor of Philosophy

University of Washington

2017

Reading Committee:

Mehran Mesbahi, Chair

Behçet Açikmeşe

Howard Chizeck

Program Authorized to Offer Degree:

Aeronautics and Astronautics

University of Washington

Abstract

Distributed Protocols, Nonlinear State-Dependent Networks, and Human-Swarm Interactions

Eric Alan Schoof

Chair of the Supervisory Committee:

Dr. Mehran Mesbahi

Aeronautics and Astronautics

This dissertation aims to explore intuitive control mechanisms for distributed protocols over networks with a goal of understanding state-dependent networks and attaining high-level human-swarm interactions. Two canonical models for network dynamics are examined from the perspective of intuitive coarse input control, namely, the linear advection dynamics with applications including formation control and load balancing; and a pair of nonlinear complex-valued dynamics which describes phase locking in coupled oscillators. Dynamic invariance properties and the topology of the basins of attraction are shown to relate to the underlying network topology which can then be exploited for coarse control. A novel bearing-compass

protocol for formation control, relying only on bearing measurements between agents, is introduced which is particularly suitable for manipulation due to its translation and scaling invariance features. This formation control dynamics can be framed as a state-dependent network, with weighted edges in the network dependent on relative measurements between the pairs of nodes incident to each edge. Formulating measures that quantify the effective access points within the network, leader selection algorithms are provided relying on submodular optimization theory. Key to understanding the bearing-compass dynamics is bearing rigidity theory which is used to describe the information content of the bearing measurements within the network. Optimizing the graph topology and access point selection with respect to rigidity measures, performant bearing-compass dynamics is generated which is well suited to external manipulation by coarse control. Generalized notions of rigidity formed from different measurements are derived and give rise to generalized measurement-based distributed protocols - a family of state-dependent network dynamics. Supporting the theory developed in this dissertation, a distributed unicycle ground vehicles platform was developed and exercised with a subset of the aforementioned distributed protocols.

Contents

Nomenclature iv

Acknowledgments vi

Dedication viii

Introduction 1

Part I. Analysis of Existing Protocols 5

Part II. Bearing Measurements and Intuitive Manipulation 6

Part III. Designing for Bearing Rigidity 7

Preliminaries 8

0.1. General Notation 8

0.2. Network Topology 10

0.3. Introduction to Submodularity 15

0.4. Voronoi Partitioning 17

0.5. Hardware Testbed 19

Part 1. From Dynamics to Coarse Control 27

Chapter 1. Advection 29

1.1. Background and Model 30

1.2. Load Balancing and Advection Properties 31

1.3. Concluding Remarks 33

Chapter 2. MDP Switching Control 35

2.1. Pattern Characterization 40

2.2. MDP Formulation for Pattern Control 43

2.3. Results for Ginzburg-Landau Dynamics 46
2.4. Concluding Remarks 48

Part 2. Bearing Measurements and Intuitive Manipulation 51

Chapter 3. Analysis of the Bearing-Compass Dynamics 53
3.1. Bearing Measurements on a Graph 53
3.2. Statement of Dynamics 56

Chapter 4. Controlling a Bearing-Compass Dynamics 67
4.1. Additive Control 67
4.2. Rotational Control 69

Chapter 5. Leader Selection for Internal Manipulation 73
5.1. Translation and Scale 73
5.2. Information Propagation 75
5.3. Pure Translation and Scale 76
5.4. Examples 79
5.5. Concluding Remarks 82

Part 3. Rigidity-Centered Design 83

Chapter 6. Edge Selection for Network Dynamic Performance 85
6.1. Selection for Bearing Rigidity 88
6.2. Selection for Convergence 89
6.3. Weight Selection 95

Chapter 7. Leader Selection for External Manipulation 98
7.1. Selection for Anchor Rigidity 100
7.2. Selection for Convergence 102
7.3. Weight Selection 103

Chapter 8. Generalizing Rigidity 107

8.1. Information Content of Relative Measurements 107
8.2. Rigidity Based Dynamics 114
8.3. Concluding Remarks 117

Final Remarks 118

Chapter 9. Conclusion and Future Work 119
Concluding Remarks 119
Future Work 121

Appendices 125

Appendix A. Bearing Rigidity Matrix Derivation 126

Bibliography 128

Nomenclature

$\mathbf{sgn}\,(c)$	Sign of scalar c.
$\mathbf{v}$	Bold lowercase roman letters indicate a vector.
$\mathbf{0}$	Vector of all zeros.
$\mathbf{1}$	Vector of all ones.
$\mathbf{e}_i$	Vector with 1 in element i and all other elements 0.
$[\mathbf{v}]_i$	Element in the ith row of vector $\mathbf{v}$.
$\lvert\mathbf{v}\rvert$	Cardinality of vector $\mathbf{v}$.
$\lVert\mathbf{v}\rVert$	2-norm, or magnitude, of vector $\mathbf{v}$.
I	Identity matrix.
$[M]_{ij}$	Element in the ith row and jth column of matrix M.
$\hat{\mathbf{v}}$	Unit-length vector of $\mathbf{v}$.
$\mathbf{w}^{\perp}$	Vector perpendicular to vector $\mathbf{w} \in \mathcal{R}^2$.
$\mathrm{Proj}_{\mathbf{b}}\mathbf{a}$	Projection of vector $\mathbf{a}$ onto vector $\mathbf{b}$.
$\mathrm{diag}(\mathbf{v})$	Diagonal matrix with elements from $\mathbf{v}$.
$\mathrm{vec}(D)$	Vector from the diagonal entries of matrix D.
$\mathcal{D}_i[M(i)]$	Block diagonal matrix of blocks $M(i)$.
$A \succ 0$	Matrix A is positive definite.
$A \succeq 0$	Matrix A is positive semi-definite.
$A \otimes B$	Kronecker product of matrices A and B.
$S \cap T$	Intersection of sets S and T.
$S \cup T$	Union of sets S and T.
$\mathcal{G}$	Undirected graph.
$\mathcal{N}(v_i)$	Set of nodes adjacent to i.

$\delta(i)$	Degree of node $i \in V$ for graph $\mathcal{G}$.
$\Delta(\mathcal{G})$	Degree matrix for graph $\mathcal{G}$.
$A(\mathcal{G})$	Adjacency matrix for graph $\mathcal{G}$.
$H(\mathcal{G})$	Incidence matrix for graph $\mathcal{G}$ with associated agent states $x \in \mathbb{R}$.
$\mathcal{L}(\mathcal{G})$	Laplacian matrix for graph $\mathcal{G}$.
$d(v_i, v_j)$	Minimum path length between v_i and v_j.
$\mathcal{D}$	Directed graph.
$\mathcal{N}_{\text{in}}(i)$	In-degree neighborhood set of node $i \in V$.
$\mathcal{N}_{\text{out}}(i)$	Out-degree neighborhood set of node $i \in V$.
$\delta_{\text{in}}(i)$	In-degree of node v_i in digraph $\mathcal{D}$.
$\delta_{\text{out}}(i)$	Out-degree of node v_i in digraph $\mathcal{D}$.
$\Delta_{\text{in}}(\mathcal{D})$	In-degree matrix of digraph $\mathcal{D}$.
$\Delta_{\text{out}}(\mathcal{D})$	Out-degree matrix of digraph $\mathcal{D}$.
$A(\mathcal{D})$	Adjacency matrix of weighted digraph $\mathcal{D}$.
$\mathcal{L}_{\text{in}}(\mathcal{D})$	In-degree graph Laplacian or Laplacian matrix of digraph $\mathcal{D}$.
$\mathcal{L}_{\text{out}}(\mathcal{D})$	Out-degree graph Laplacian or Laplacian matrix of digraph $\mathcal{D}$.
$\mathcal{A}$	Set of actions in a Markov decision process.
$\mathcal{R}$	Set of rewards in a Markov decision process.
$\mathcal{S}$	Set of states in a Markov decision process.
$\mathcal{T}$	Set of transition probabilities between all states $s, s' \in \mathcal{S}$ given action $a \in \mathcal{A}$ in a Markov decision process.
$\Pr(\cdot)$	Probability of a given event.
$\pi(s)$	Optimal policy for a Markov decision process $(\mathcal{S}, \mathcal{A}, \mathcal{T}, \mathcal{R})$ in state $s \in \mathcal{S}$.

Acknowledgments

Not many people return to academia from industry [citation needed], but Professor Mehran Mesbahi was able to entice me to do just that. After taking his multi-variable controls course I was hooked, and the rest is, as they say, history. Prof. Mesbahi was not just my adviser, as that does not begin to describe his role in my journey. He is sharp yet humble. He will guide you to answers without you even realizing you had a question. He literally knows the name of every person and every theorem. Perhaps most importantly, however, he is always there for his students, no matter how much trouble they get themselves into. I am grateful for the fleeting time I was able to spend with him in the Robotics, Aerospace, and Information Networks (RAIN) lab at UW, and hope for many opportunities to work with him in the future.

I would also like to extend my thanks to my colleagues and lab-mates at the University of Washington. Sharing an office was a job, but sharing conversations, jokes, food, and of course coffee was what made the job truly enjoyable. I would like to extend special thanks to a few individuals; Dr. Saghar Hosseini for being willing to chat about coding problems and for always smiling; Dr. Armand Awad for helping me understand time scales; Dr. Max Spetzler for facilitating literally hundreds of gallons of coffee and his support developing the beacon sensor for the lab hardware testbed; and Dr. Airlie Chapman for her tireless encouragement. Without them, my research would not be what it is today.

Thanks to my professors at the UW. They were instrumental in helping maintain my momentum throughout my PhD. Specifically Profs. Howard Chizeck, Dieter Fox, Blake Hannaford, Kuen Lin, Eli Livne, Mehran Mesbahi, and Kristi Morgansen were exceptional. And I cannot say enough good things about the AA staff. Ed Connery and Wanda Frederick were always there to look after me with a smile, Jenny Park and Nancy-Lou Polk always made

sure I got paid, and Fiona Spencer always had my back when there was that one part/tool I was missing. And of course my graduate committee which, while changing from exam to exam, maintained the highest standards of integrity and guidance I could have hoped for, so I extend my deepest thanks to Profs. Behçet Açikmeşe, Howard Chizeck, Dieter Fox, Kuen Lin, Mehran Mesbahi, Marco Salviato, and Anshu Narang-Siddarth.

Finally, I am exceedingly fortunate to have not one, but two amazingly supportive families. My mother Pam and father Craig instilled in me curiosity and a burning desire to disassemble everything. Of course, I would *always* put said things back together. Never... I meant never. My two dear sisters helped shape everything I am. Stephanie can always make me laugh, and Kristen has never questioned me asking for support or just needing to vent at life. I can always count on David to consider any premise and talk endlessly about crazy solutions that are over-engineered just the right amount. My aunts, uncles, cousins, and grandmother exude endless warmth, caring, and generosity. Then there is my *other* family. Fiona and Geoff are always willing to help, whether it is reading papers from Australia, or flying half-way around the world to help with cooking while papers are inevitably being written too close to their submission deadline. Troy, Tahira, Jason, and Rico are very special to me, and I look forward to being a little bit closer to them soon.

And then there is my wife, Airlie. I would need another dissertation to describe what she has meant to me through all these years. Suffice it to say, she is my rock, my confidence, and my inspiration. I cannot wait to see what our next adventures have in store for us!

Dedication

For my family and my wife, Airlie.

All I am and all I do is because of you.

Introduction

Networked dynamic control is an important problem in networked systems such as multi-vehicle robotics. Significant of late is the problem's formulation from a distributed point of view, where an individual robotic agent only uses local information defined over a network communication graph for its operation [**1, 2**]. By restricting the scope of an individual agent, the system as a whole becomes both more robust to agent failure and scalable to larger numbers of agents. A common strategy employed in the literature is to generate an agent control law that only relies on information obtained about other nearby agents [**3, 4, 5, 6, 7, 8**]. These strategies are termed *distributed protocols*.

Aligned with the problem of designing distributed protocols is the intuitive manipulation or control of these protocols using coarse inputs. A driving application is the seamless integration of human signals into the networked system, or swarm, referred to as *human-swarm interaction*. Coarse human inputs can be generated by simple body gestures such as pointing and waving or various touchscreen gestures; see Figures 0.1.1 and 0.1.2. Manipulating a dynamics typically relies on adapting the protocol or augmenting it with external signals. The focus of this dissertation is on developing theory and algorithms for the effective manipulation of distributed protocols with coarse inputs, drawing on the fields of control theory, graph theory, and convex and submodular optimization.

A less typical form of control is the topological design or adaption of the underlying communication network to manipulate the dynamics. Topological design is unique to networked dynamics and often presents a coarse form of control. As such, it is an attractive avenue for manipulation. Designing topologies to optimize for a given performance metric has been addressed in the literature. These methods typically fit into two broad classes; continuous and combinatorial design.

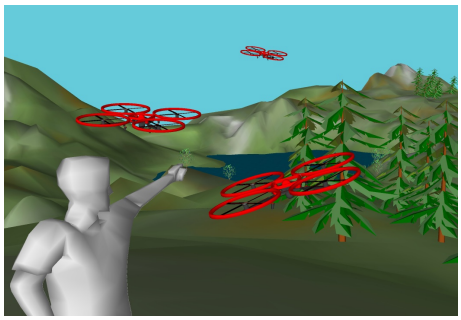

FIGURE 0.1.1. Simple body gesture example of human-swarm interaction.

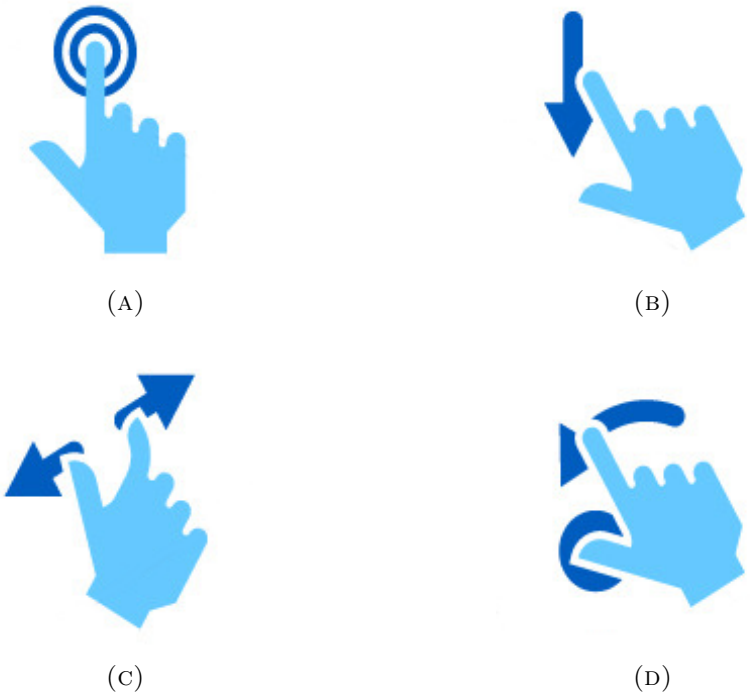

(A) (B)

(C) (D)

FIGURE 0.1.2. Various touchscreen gestures that enable coarse input from a human. A) tap, B) swipe, C) pinch-to-zoom, and D) rotate.

The first class examines the continuous design of variables on the graph topology, e.g., through edge weights and input control weights. For example, Wan *et al.* maximized the largest eigenvalue of the graph Laplacian through the selection of edge weights [**9**]. Chapman *et al.* designed edge weights distributively and online to reject network-level disturbances [**10**]. Zelazo and Mesbahi leveraged convex optimization techniques to design edge weights for performance improvements under the $\mathcal{H}_2$ and $\mathcal{H}_\infty$ norms [**11**]. With the objective of

maximizing the algebraic connectivity of the graph Laplacian, Ghosh and Boyd examined techniques to grow graphs with improved connectivity [**12**].

The second class is a combinatorial approach that examines node or edge selection problems. Techniques from convex optimization and submodularity theory have been used to select influential access points to a network, also referred to as the leader selection problem [**13, 14, 15**]. The leader selection problem for robotic swarms fits in a larger class of robot task assignment problems [**16**]. These problems are often posed as optimization problems with a set of leaders having an associated selection cost, such as swarm manipulability [**17**], network coherence [**13**] and $\mathcal{H}_2$ norm input amplification [**18, 15**]. The problems, due to their combinatorial nature, are often NP-hard and so require a relaxed or approximate solution. Submodular optimization has emerged as a popular technique to solve the discrete topology design problem [**19, 20, 21, 22, 23**]. An attraction of this theory is that greedy selection heuristics may be employed to achieve provably near-optimal solutions.

Coarse input control of three distributed protocols are examined in this work. In Part 1, two existing protocols are explored, namely the linear *advection protocol* and the nonlinear dynamics of networks of *coupled oscillators*. In Parts 2 and 3, an in depth study of a novel *formation control protocol*, derived by the authors and based on bearing-compass measurements, is explored. This bearing-compass protocol is shown to be particularly well suited to coarse control.

The *advection protocol* is the discretization of the fluid-based advection PDE over a network. The linear dynamics induce a conserved flow through the directed edges of the network dynamics. Due to this feature, the advection protocol has been used to model the spread of diseases [**2**], population migrations [**24**], supply and demand in economic systems [**25**], and recently applied to formation control as a sensor coverage problem by the authors in [**26**]. Examining a load-balancing application using advection, coarse control of the invariance subspace of advection is explored.

Phase synchronization in *coupled oscillators* is an extensive area of research [**27, 28, 29, 30**]. Less studied but still prominent in the literature is the examination of other types of

patterns in networks of oscillators [**31**]. A pattern occurs when the frequency of all oscillators synchronize, or equivalently their phases lock, with the phase separation between oscillators describing the type of pattern. These equilibria are referred to as phase locked, incoherent states or, if the set of oscillator phases are evenly distributed on the unit circle, balanced states [**27**]. In biological systems these different patterns give rise to different temporal and spatial collective behavior, for example in the flashing of fireflies, heart's pacemaker cells, brain neurons, and fish schooling [**32**]. Addressed in this dissertation is a network topology-based method to control the pattern exhibited by networks of oscillators.

Previous work in the area of pattern control or equilibrium switching in oscillators fall under the classes of non-feedback control strategies and feedback control strategies. The former control strategy acts via an external perturbation such as a short pulse, a pseudo-periodic or harmonic forcing signal [**33, 34**]. These methods are in general easy to apply, since they do not require intimate knowledge of system dynamics. The control is usually not efficient in the sense that the amplitude of the external signal is relatively large. The other successful method is to use feedback techniques where the internal state of the system is fed back into the dynamics either instantaneously or with a time delay [**32**]. Feedback schemes typically boast smaller external signals but can be more challenging to implement experimentally as continuous signal perturbations are required. The attraction of topological rewiring is that it represents a marriage of these two classes of control. Rewiring is a discrete event but induces a new set of feedback mechanisms in the network due to the new couplings produced or removed between edges.

Formation control protocols fit under a broader class of distributed protocols. Distributed formation control protocols are popular in the area of robotic formation control due to the fact that an individual agent needs only local information about its neighbors for operation. One of the most popular local information types is relative distance-based measurements [**35, 2**]. This information can be obtained for example by the strength of the received wireless communication signals. The examination of relative bearing-based measurements has become of interest in the last decade, with this current work fitting into this subclass [**36, 37, 38, 39**].

The protocols require knowledge of the relative bearing of neighboring agents for example from a monocular camera [**40**]. Both distance-based and bearing-based protocols rely on graph rigidity theory to guarantee that the protocols will converge to a unique formation shape based on the location of the relative measurements within the communication graph. The ability to reason about and design the placement of relative measurements within a network based on rigidity theory measures is one of the topics addressed in this dissertation. More broadly, relative measurements over a network can be framed as a *state-dependent network* problem, with edge weights in the graph dependent on the states of the nodes incident with the edge.

The dissertation is composed on three parts addressing the coarse control of existing protocols; the formulation of a formation control that is particularly suited to intuitive control; and a rigidity based framework for coarse topological control. The work is concluded with some final remarks and some direction for future work.

Part I. Analysis of Existing Protocols

The first portion of this part, Chapter 1, examines the properties of the linear advection dynamics. The dynamics are shown to serve as an attractive dynamics for coarse inputs. Its suitability for coarse control stems from the structure of invariance features within the dynamics. Invariance features are encoded in the role of the underlying graph structure and can be varied through simple edge reweighting.

The second portion of this part, Chapter 2, proposes a coarse control methodology for pattern control in a network of identical coupled oscillators. Patterns correspond to stable equilibriums in an oscillator network over different coupling coefficients and available network topologies. We show that the discrete graph based version of the Ginzburg-Landau equation, referred to as the graph Ginzburg-Landau dynamics, exhibits n pattern equilibrium for an n-node cycle graph with the sign of the oscillator coupling coefficient dictating the stability of the pattern. The pattern control problem is cast as a discrete Markov Decision Process (MDP) whose state space is the set of patterns realizable on subgraphs of the network.

Actions in the MDP correspond to the coarse control selection of coupling coefficients and edge switches in the network. Transition sampling is applied to generate the transition probabilities. The sampling approach is also applied to a nanoelectromechanical (NEM) coupled oscillator dynamics [**41**] to perform pattern control without the knowledge of an underlying Lyapunov function.

Part II. Bearing Measurements and Intuitive Manipulation

This part develops a novel bearing-based dynamics in Chapter 3, building on the literature that use a bearing-only approach to formation control [**37, 38, 36**]. We complemented these works by designing a control law that also relies on a single additional sensor, a compass, to localize the rotation in the global reference frame [**42**], which was also recently studied by Zhao and Zelazo [**43**]. The proposed bearing-compass control law has the attraction that the centroid location and scale remain invariant under the dynamics. A feature of interest to a human operator is the coarse manipulation of the formation's translation and scale. In Chapter 4 we examine how external control added to a subset of agents, referred to as leader agents, allows the centroid and scale to be arbitrarily shifted. A focus of this part is the efficient selection of leader agents for achieving these tasks, and is discussed in Chapter 5.

We formulate the leader selection problem, with a range of translation and scaling cost functions, as a combinatorial optimization problem. For translation and scale maximization the problem is associated with the maximization of a monotone increasing submodular function [**20**]. Mirroring similar approaches to solving leader selection problems over submodular functions [**14, 44**], a greedy leader selection algorithm is applied which provides guaranteed sub-optimal performance [**19**]. Further we formulate the leader selection problem over a *pure* translation cost function, meaning maximizing translation without formation scaling, as a mixed-integer quadratic program. An integer relaxation of the problem yields a sub-optimal solution in polynomial time. The *pure* scaling leader selection problem is similarly examined. To demonstrate the algorithms feasibility, the control law and leader selection process is implemented on a unicycle swarm.

Part III. Designing for Bearing Rigidity

This part extends the bearing-compass dynamics [**42, 39**] to allow selecting the weights on the agent interaction topology in Chapter 6 and includes the addition of fixed anchors in Chapter 7. Further, the field of submodular optimization is applied to build and manipulate formations by making provably near-optimal decisions that would be computationally infeasible to perform optimally. We show how several rigidity-based submodular metrics perform under edge and node selection. We also use convex optimization to select edge weights that improve the convergence of formation acquisition and manipulation protocols without increasing the required control authority for any individual agent in the formation. The current work relies heavily on this framework to design well-performing graphs under rigidity performance measures and provides insights into methods of examining state-dependent networks.

Dynamics applicable to a mix of range and bearing information is also considered, for example, when a subset of agents has the full relative position of a subset of neighbors [**45**], or when the distance between agents can be estimated using bearing measurements [**46**]. To this end, the approach adopted in Chapter 8 is a generalization of the bearing-compass dynamics via a generalized rigidity theory. This generalization produces a family of state-dependent network dynamics with edge weights in the network changing with the states of the edge nodes, due to the nonlinearity of the underlying measurement dynamics. We provide a systematic way to prove asymptotic convergence these state-dependent dynamics using the proposed generalized rigidity theory.

Preliminaries

In this introductory chapter, we will look at some common notation, as well as present common characterizations of swarms of autonomous agents. This section will also contain an overview of some of the hardware platforms developed to exercise the theory developed in this research.

We begin in §0.1 by discussing general notation and mathematical constructs used throughout this research. In §0.2, we look specifically at some definitions and properties relating to graph theory. The notion of a graph is used extensively to encode communication and sensor networks. We present a brief overview of modular and submodular functions in §0.3. Submodularity will be leveraged in Parts 2 and 3 to develop near-optimal solutions to typically intractable combinatorial problems. In §0.4, we describe a method by which a human can coarsely define a distribution of robots, which will be used as a target for many of the algorithms presented in this research. Finally, in §0.5, we introduce the hardware testbed developed to exercise the theory presented herein.

0.1. General Notation

For a vector $\mathbf{v} \in \mathbb{R}^n$, $[\mathbf{v}]_i$ denotes the ith element and $|\mathbf{v}|$ denotes the number of elements, or cardinality, of $\mathbf{v}$. We define the vectors $\mathbf{0}_n$ and $\mathbf{1}_n$, or if clear from context $\mathbf{0}$ and $\mathbf{1}$, to be the vectors of length n containing all zeros and ones, respectively. The notation $\|\mathbf{v}\|_p$ represents the p-norm of vector $\mathbf{v} \in \mathbb{R}^n$ as

$$\|\mathbf{v}\|_p \triangleq \left(\sum_{i=1}^{n} |[\mathbf{v}]_i|^p \right)^{1/p}.$$

When p is omitted, it is assumed that $p = 2$, and $\|\mathbf{v}\|$ is commonly called the magnitude of $\mathbf{v}$. The vector with the ith element 1 and all other elements 0 is denoted $\mathbf{e}_i$. We define

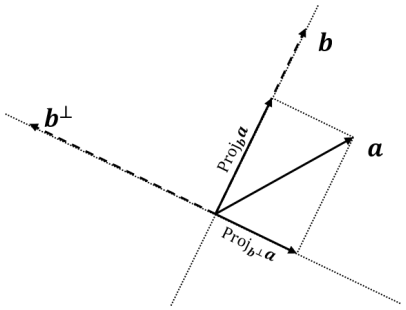

FIGURE 0.1.1. Projection example.

$\mathbf{v}_{ij} \triangleq \mathbf{v}_j - \mathbf{v}_i$. The normalized vector of $\mathbf{v}$ is denoted $\hat{\mathbf{v}} \triangleq \mathbf{v}/\left\|\mathbf{v}\right\|$. Given a vector $\mathbf{w} \in \mathbb{R}^2$, we define the vector perpendicular to $\mathbf{w}$ as $\mathbf{w}^{\perp} \triangleq \begin{bmatrix} -[\mathbf{w}]_2 & [\mathbf{w}]_1 \end{bmatrix}^T$.

Given vectors $\mathbf{a}, \mathbf{b} \in \mathbb{R}^n$, the projection of $\mathbf{a}$ onto $\mathbf{b}$ is defined as $\text{Proj}_{\mathbf{b}}\mathbf{a} \triangleq \left({}^{\mathbf{a}^T\mathbf{b}}/_{\|\mathbf{a}\|\|\mathbf{b}\|}\right)\mathbf{b}$, which for $n = 2$ implies that $\mathbf{a} - \text{Proj}_{\mathbf{b}}\mathbf{a} = \text{Proj}_{\mathbf{b}^{\perp}}\mathbf{a}$. These terms are visualized in Fig. 0.1.1. The operator $\mathbf{sgn}(c)$ for $c \in \mathbb{R}$ is defined as $\mathbf{sgn}(c) \triangleq {}^{c}/_{|c|}$ for $c \neq 0$ and 0 otherwise.

The matrix I_n, or I, denotes the $n \times n$ *identity matrix*. For a matrix $M \in \mathbb{R}^{p \times q}$, $[M]_{ij}$ denotes the *element* in the ith row and jth column of M. The *Kronecker product* of matrices A and B is denoted $A \otimes B$. The notation $A \succ 0$ and $A \succeq 0$ designate a matrix A as being *positive definite* and *positive semi-definite*, respectively. The matrix $\mathcal{D}_i[M(i)]$ is the *block diagonal matrix* consisting of blocks $M(i)$. The block diagonal matrix

$$\mathcal{D}_i\left[[\mathbf{v}]_i\right] = \begin{bmatrix} [\mathbf{v}]_1 & 0 & \cdots & 0 \\ 0 & [\mathbf{v}]_2 & \cdots & 0 \\ \vdots & \vdots & \ddots & 0 \\ 0 & 0 & 0 & [\mathbf{v}]_n \end{bmatrix}$$

for $\mathbf{v} \in \mathbb{R}^n$ is said to *diagonalize* vector $\mathbf{v}$, and is denoted $\text{diag}(\mathbf{v})$. Similarly, given a diagonal matrix

$$D = \begin{bmatrix} d_1 & 0 & \cdots & 0 \\ 0 & d_2 & \cdots & 0 \\ \vdots & \vdots & \ddots & 0 \\ 0 & 0 & 0 & d_n \end{bmatrix},$$

we *vectorize* D by letting $\text{vec}\,(D) = \begin{bmatrix} d_1 & d_2 & \dots & d_n \end{bmatrix}^T$.

The cardinality of a set S is denoted $|S|$. The union of sets S and T is denoted $S \cup T$ and is defined $S \cup T \triangleq \{a : a \in S \,\text{or}\, a \in T\}$. The intersection of sets S and T is denoted $S \cap T$ and is defined $S \cap T \triangleq \{a : a \in S \,\text{and}\, a \in T\}$.

We introduce the notation $\mathbf{b}_{(ij)}$ to abstractly represent the component of $\mathbf{b}_i$ due to j. This notation will typically appear in sums over agents, and will always imply that $\mathbf{b}_{(ij)} = -\mathbf{b}_{(ji)}$. We note that it is not necessary for $\mathbf{b}_{(ij)} = \mathbf{b}_{ij} = \mathbf{b}_j - \mathbf{b}_i$, but it will often be the case in this research.

0.2. Network Topology

0.2.1. Undirected Graphs. Given a set of nodes V with cardinality n, a set of undirected edges $\{i, j\} \in E : i, j \in V$ with cardinality m, and a weight vector $\mathbf{w} \in \mathbb{R}^m$ which corresponds to the edges in E, we denote an *undirected weighted graph* $\mathcal{G} = (V, E, \mathbf{w})$. If $\mathbf{w}$ is omitted, we call $\mathcal{G}$ an *undirected graph*, or simply a *graph*, and we assume $\mathbf{w} = \mathbf{1}$. We arbitrarily label the edges $\bar{k} = 1, \dots, m$, then we use the notation $\bar{k}$ and $\{i, j\} \in E$ interchangeably with associated edge weights denoted by $w_{\bar{k}}$ and w_{ij}, respectively. The *neighborhood set* $\mathcal{N}(v_i)$ is composed of the set of nodes adjacent to v_i.

Graphs can be encoded in many forms. The ones that we will use take the form of matrices, and each has certain properties we will exploit. Figure 0.2.1a contains an example graph we use for reference. The graph in Figure 0.2.1a has node set

$$V = \{1, 2, 3, 4\},$$

edge set

$$E = \{\{1, 2\}, \{1, 3\}, \{1, 4\}, \{2, 3\}, \{3, 4\}\},$$

unitary weights $\mathbf{w} = \mathbf{1}$, and has the following edge labeling.

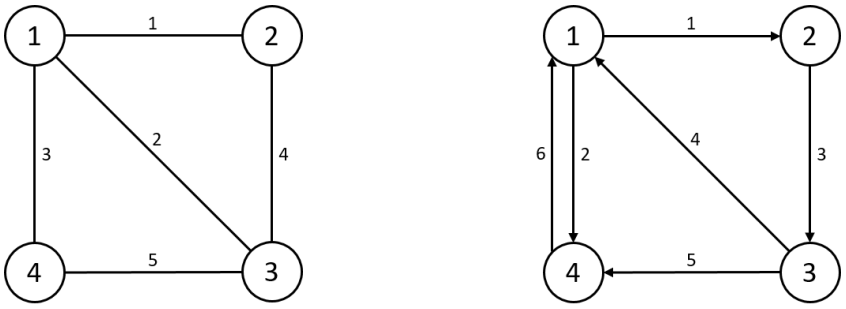

(A) (B)

FIGURE 0.2.1. Examples of (A) an unweighted undirected graph and (B) an unweighted directed graph. Numbers in the circles are the node numbers, and numbers on the lines are the edge numbers.

$\bar{k}$	$\{i,j\} \in E$
1	$\{1,2\}$
2	$\{1,3\}$
3	$\{1,4\}$
4	$\{2,3\}$
5	$\{3,4\}$

DEFINITION 1. The *degree* $\delta(i)$ of a node $i \in V$ in graph $\mathcal{G}$ is the sum of weights incident to node i. It can be calculated from $A(\mathcal{G})$ as the row-sum

$$\delta(i) = \sum_{j=1}^{n} [A(\mathcal{G})]_{ij}.$$

The degree of nodes 1 and 2 of the graph $\mathcal{G}$ in Figure 0.2.1a is $\delta(1) = 3$ and $\delta(2) = 2$, respectively.

DEFINITION 2. The degree matrix $\Delta(\mathcal{G}) \in \mathbb{R}^{n \times n}$ is

$$[\Delta(\mathcal{G})]_{ij} = \begin{cases} \delta(i) & i = j \\ 0 & \text{otherwise.} \end{cases}$$

The degree matrix for the graph $\mathcal{G}$ in Fig. 0.2.1a is

$$\Delta(\mathcal{G}) = \begin{bmatrix} 3 & 0 & 0 & 0 \\ 0 & 2 & 0 & 0 \\ 0 & 0 & 3 & 0 \\ 0 & 0 & 0 & 2 \end{bmatrix}.$$

DEFINITION 3. The *adjacency matrix* $A(\mathcal{G})$ of an undirected, weighted graph as is a matrix of dimension $n \times n$. For each edge $\{i, j\} \in E$ with corresponding weight w_{ij}, we have that $[A(\mathcal{G})]_{ij} = w_{ij}$ and $[A(\mathcal{G})]_{ji} = w_{ij}$. All other elements are zero.

An example adjacency matrix for the graph $\mathcal{G}$ in Figure 0.2.1a is

$$A(\mathcal{G}) = \begin{bmatrix} 0 & 1 & 1 & 1 \\ 1 & 0 & 1 & 0 \\ 1 & 1 & 0 & 1 \\ 1 & 0 & 1 & 0 \end{bmatrix}.$$

DEFINITION 4. The *incidence matrix* $H(\mathcal{G}) \in \mathbb{R}^{m \times n}$ of a graph $\mathcal{G}$ is defined over each edge $\bar{k} \in E$ as

$$[H(\mathcal{G})]_{\bar{k}\ell} = \begin{cases} -1 & \{\ell, j\} \in E \\ 1 & \{i, \ell\} \in E \\ 0 & \text{otherwise.} \end{cases}$$

The incidence matrix for the graph $\mathcal{G}$ in Fig. 0.2.1a is

$$H(\mathcal{G}) = \begin{bmatrix} -1 & 1 & 0 & 0 \\ -1 & 0 & 1 & 0 \\ -1 & 0 & 0 & 1 \\ 0 & -1 & 1 & 0 \\ 0 & 0 & -1 & 1 \end{bmatrix}.$$

DEFINITION 5. The *Laplacian matrix* $\mathcal{L}(\mathcal{G})$ of a graph $\mathcal{G}$ is defined as

$$\mathcal{L}(\mathcal{G}) = \Delta(\mathcal{G}) - A(\mathcal{G}) \tag{0.2.1}$$

or, equivalently,

$$\mathcal{L}(\mathcal{G}) = H(\mathcal{G})^T W H(\mathcal{G}), \tag{0.2.2}$$

where $W = \operatorname{diag}(\mathbf{w})$.

For the Laplacian matrix, one has $\mathbf{1}^T\mathcal{L}(\mathcal{G}) = \mathbf{0}^T$, $\mathcal{L}(\mathcal{G})\mathbf{1} = \mathbf{0}$, and eigenvalues $0 = \lambda_1(\mathcal{G}) \leq \lambda_2(\mathcal{G}) \leq \cdots \leq \lambda_n(\mathcal{G})$. The ith row of the Laplacian matrix is denoted as $\mathcal{L}_i(\mathcal{G})$.

The Laplacian matrix for the graph $\mathcal{G}$ in Fig. 0.2.1a is

$$\mathcal{L}(\mathcal{G}) = \begin{bmatrix} 3 & -1 & -1 & -1 \\ -1 & 2 & -1 & 0 \\ -1 & -1 & 3 & -1 \\ -1 & 0 & -1 & 2 \end{bmatrix}.$$

One of the matrices that is used frequently in this research is the incidence matrix H, so we present some examples here to make clear the notation and purpose of this matrix.

If each agent associated with a node i in a graph $\mathcal{G}$ has a state $x_i \in \mathbb{R}$, the states can be stacked as

$$\mathbf{x} = \begin{bmatrix} x_1 & x_2 & \dots & x_n \end{bmatrix}^T,$$

then the relative states between neighboring agents in the graph can be calculated as

$$\overline{\mathbf{x}} = H\mathbf{x}. \tag{0.2.3}$$

For example, if we look at the graph $\mathcal{G}$ in Fig. 0.2.1a, then Eq. (0.2.3) becomes

$$\begin{bmatrix} -1 & 1 & 0 & 0 \\ -1 & 0 & 1 & 0 \\ -1 & 0 & 0 & 1 \\ 0 & -1 & 1 & 0 \\ 0 & 0 & -1 & 1 \end{bmatrix} \begin{bmatrix} x_1 \\ x_2 \\ x_3 \\ x_4 \end{bmatrix} = \begin{bmatrix} x_2 - x_1 \\ x_3 - x_1 \\ x_4 - x_1 \\ x_3 - x_2 \\ x_4 - x_3 \end{bmatrix} = \begin{bmatrix} x_{21} \\ x_{31} \\ x_{41} \\ x_{32} \\ x_{43} \end{bmatrix} = \begin{bmatrix} x_{\bar{1}} \\ x_{\bar{2}} \\ x_{\bar{3}} \\ x_{\bar{4}} \\ x_{\bar{5}} \end{bmatrix}.$$

We observe that because $x_{ij} = -x_{ji}$ for all $\{i, j\} \in E$, we can also write

$$\begin{bmatrix} x_{(21)} \\ x_{(31)} \\ x_{(41)} \\ x_{(32)} \\ x_{(43)} \end{bmatrix} = \begin{bmatrix} x_{21} \\ x_{31} \\ x_{41} \\ x_{32} \\ x_{43} \end{bmatrix} = \begin{bmatrix} x_{\bar{1}} \\ x_{\bar{2}} \\ x_{\bar{3}} \\ x_{\bar{4}} \\ x_{\bar{5}} \end{bmatrix} = \begin{bmatrix} x_{(\bar{1})} \\ x_{(\bar{2})} \\ x_{(\bar{3})} \\ x_{(\bar{4})} \\ x_{(\bar{5})} \end{bmatrix}$$

to highlight this property.

If each agent i instead has a higher-dimensional state $\mathbf{x}_i \in \mathbb{R}^d$, with $\mathbf{x} = \begin{bmatrix} \mathbf{x}_1^T & \mathbf{x}_2^T & \dots & \mathbf{x}_n^T \end{bmatrix}^T$, then the relative state vectors between neighboring agents can be calculated as

$$\begin{aligned} \overline{\mathbf{x}} &= (H \otimes I_d)\,\mathbf{x} \\ &\triangleq \widetilde{H}\mathbf{x}. \end{aligned} \tag{0.2.4}$$

Following the previous example, if we assume each agent i has state $\mathbf{x}_i \in \mathbb{R}^2$, then

$$\widetilde{H}\mathbf{x} = \begin{bmatrix} -1 & 0 & 1 & 0 & 0 & 0 & 0 & 0 \\ 0 & -1 & 0 & 1 & 0 & 0 & 0 & 0 \\ -1 & 0 & 0 & 0 & 1 & 0 & 0 & 0 \\ 0 & -1 & 0 & 0 & 0 & 1 & 0 & 0 \\ -1 & 0 & 0 & 0 & 0 & 0 & 1 & 0 \\ 0 & -1 & 0 & 0 & 0 & 0 & 0 & 1 \\ 0 & 0 & -1 & 0 & 1 & 0 & 0 & 0 \\ 0 & 0 & 0 & -1 & 0 & 1 & 0 & 0 \\ 0 & 0 & 0 & 0 & -1 & 0 & 1 & 0 \\ 0 & 0 & 0 & 0 & 0 & -1 & 0 & 1 \end{bmatrix} \begin{bmatrix} [\mathbf{x}_1]_1 \\ [\mathbf{x}_1]_2 \\ [\mathbf{x}_2]_1 \\ [\mathbf{x}_2]_2 \\ [\mathbf{x}_3]_1 \\ [\mathbf{x}_3]_2 \\ [\mathbf{x}_4]_1 \\ [\mathbf{x}_4]_2 \end{bmatrix}$$

$$= \begin{bmatrix} [\mathbf{x}_2]_1 - [\mathbf{x}_1]_1 \\ [\mathbf{x}_2]_2 - [\mathbf{x}_1]_2 \\ [\mathbf{x}_3]_1 - [\mathbf{x}_1]_1 \\ [\mathbf{x}_3]_2 - [\mathbf{x}_1]_2 \\ [\mathbf{x}_4]_1 - [\mathbf{x}_1]_1 \\ [\mathbf{x}_4]_2 - [\mathbf{x}_1]_2 \\ [\mathbf{x}_3]_1 - [\mathbf{x}_2]_1 \\ [\mathbf{x}_3]_2 - [\mathbf{x}_2]_2 \\ [\mathbf{x}_4]_1 - [\mathbf{x}_3]_1 \\ [\mathbf{x}_4]_2 - [\mathbf{x}_3]_2 \end{bmatrix} = \begin{bmatrix} \mathbf{x}_2 - \mathbf{x}_1 \\ \mathbf{x}_3 - \mathbf{x}_1 \\ \mathbf{x}_4 - \mathbf{x}_1 \\ \mathbf{x}_3 - \mathbf{x}_2 \\ \mathbf{x}_4 - \mathbf{x}_3 \end{bmatrix} = \begin{bmatrix} \mathbf{x}_{21} \\ \mathbf{x}_{31} \\ \mathbf{x}_{41} \\ \mathbf{x}_{32} \\ \mathbf{x}_{43} \end{bmatrix} = \begin{bmatrix} \mathbf{x}_{(21)} \\ \mathbf{x}_{(31)} \\ \mathbf{x}_{(41)} \\ \mathbf{x}_{(32)} \\ \mathbf{x}_{(43)} \end{bmatrix} = \begin{bmatrix} \mathbf{x}_{(\bar{1})} \\ \mathbf{x}_{(\bar{2})} \\ \mathbf{x}_{(\bar{3})} \\ \mathbf{x}_{(\bar{4})} \\ \mathbf{x}_{(\bar{5})} \end{bmatrix}.$$

DEFINITION 6. A *path* from node i to node j in graph $\mathcal{G}$ is an ordered list of nodes in V which starts with node i, continues along edges in E, and ends with node j, such that no node in the list appears more than once.

If we examine Figure 0.2.1a, we see that there are four paths from node 2 to node 4, which are $P_1 = (2, 1, 4)$, $P_2 = (2, 3, 4)$, $P_3 = (2, 1, 3, 4)$, and $P_4 = (1, 3, 2, 4)$.

DEFINITION 7. The *shortest path(s)* between nodes i and j in graph $\mathcal{G}$ is given by the path(s) between nodes i and j with the smallest magnitude $d(v_i, v_j)$.

The shortest paths from Figure 0.2.1a from node 2 to node 4 are $P_1 = (2, 1, 4)$ and $P_2 = (2, 3, 4)$.

DEFINITION 8. A graph $\mathcal{G}$ is called *connected* if there exists at least one path between all pairs of vertices in V. Otherwise, it is called *disconnected*.

DEFINITION 9. The *diameter* of a graph $\mathcal{G}$, denoted $\text{diam}(\mathcal{G})$, is the length of the longest shortest path over all pairs of vertices in $\mathcal{G}$.

For example, the diameter of the graph $\mathcal{G}$ in Figure 0.2.1a is 2.

0.2.2. Directed Graphs. A generalization of a graph is a weighted *directed graph*, or *digraph*. A weighted digraph $\mathcal{D} = (V, E, W)$ is characterized by a node set V with cardinality n, an edge set E comprised of ordered pairs of nodes with cardinality m, and a weight set W with cardinality m. Here, $(i, j) \in E$ indicates a directed edge from i to j. The adjacency matrix is an $n \times n$ matrix with $[A(\mathcal{D})]_{ij} = w_{ij} \in W$ when $(j, i) \in E$ and $[A(\mathcal{D})]_{ij} = 0$ otherwise. The in-degree matrix $\Delta_{\text{in}}(\mathcal{D}) \in \mathbb{R}^{n \times n}$ is a diagonal matrix with the number of edges incident to node i, its in-degree $\delta_{\text{in}}(i) \stackrel{\triangle}{=} \sum_{(j,i) \in E} w_{ij}$, at position (i, i). The out-degree matrix $\Delta_{\text{out}}(\mathcal{D})$ is similarly defined, using the out-degree $\delta_{\text{out}}(i) = \sum_{(i,k) \in E} w_{ki}$. The in-degree graph Laplacian (or Laplacian) matrix $\mathcal{L}_{in}(\mathcal{D})$ (or $\mathcal{L}(\mathcal{D})$) is defined as $[\mathcal{L}(\mathcal{D})]_{ij} = -[A(\mathcal{D})]_{ij}$ for $i \neq j$ and $[\mathcal{L}(\mathcal{D})]_{ii} = [\Delta_{\text{in}}(\mathcal{D})]_{ii}$. The out-degree graph Laplacian $\mathcal{L}_{\text{out}}(\mathcal{D})$ is similarly defined. The in-degree neighborhood set $\mathcal{N}_{\text{in}}(i)$ is composed of the set of nodes attached to in-degree edges of v_i. Similarly, $\mathcal{N}_{\text{out}}(i)$ is defined in terms of the out-degree edges of v_i. A special family of digraphs is the strongly connected graphs, where a digraph is strongly connected if between every pair of distinct nodes there exists a directed path of edges. For convenience, we can treat an undirected graph $\mathcal{G}$ as a directed graph $\mathcal{D}$ using the same node set V if, for every edge $\{i, j\} \in E$ in $\mathcal{G}$, we assume that both $(i, j) \in E$ and $(j, i) \in E$ with weights $w_{ij} = w_{ji} \in W$ in $\mathcal{D}$.

The adjacency matrix for the unweighted digraph $\mathcal{D}$ in Fig. 0.2.1b is

$$A(\mathcal{D}) = \begin{bmatrix} 0 & 1 & 0 & 1 \\ 0 & 0 & 1 & 0 \\ 1 & 0 & 0 & 1 \\ 1 & 0 & 0 & 0 \end{bmatrix}.$$

0.3. Introduction to Submodularity

Submodularity is a topic area that we will leverage extensively in this research, starting with Chapter 4. At a basic level, it will provide a mechanism for solving certain otherwise intractable problems in a fast, and provably near-optimal way.

We denote functions of the form $f(S) : 2^n \to \mathbb{R}$, where $S \subseteq \mathcal{S}$ and $|\mathcal{S}| = n$, as *set functions*. The *empty set* is denoted $\emptyset$. These functions can have many properties that we can exploit, some of which are reviewed next.

DEFINITION 10. A set function $f(S) : 2^n \to \mathbb{R}$ is *modular* if for all subsets $S \subseteq \mathcal{S}$ it can be expressed as

$$f(S) = w(\emptyset) + \sum_{s \in S} w(s),$$

for some weight function $w : s \in \mathcal{S} \to \mathbb{R}$.

DEFINITION 11. A set function $f(S) : 2^n \to \mathbb{R}$ is *monotone increasing* if, for all subsets $A \subseteq B \subseteq \mathcal{S}$ it holds that $f(A) \leq f(B)$.

DEFINITION 12. [**19**, Def. 2.1] A set function $f(S) : 2^n \to \mathbb{R}$ is *submodular* if, for all subsets $A \subseteq B \subseteq \mathcal{S}$ and $s \notin B$, then

$$f(A \cup \{s\}) - f(A) \geq f(B \cup \{s\}) - f(B). \tag{0.3.1}$$

The intuition behind Def. 12 is that adding an element to a smaller set gives a greater gain than adding the same element to a larger set, sometimes called "diminishing returns." Submodular functions bear similarities to convex functions [**20**]. This connection can be used to provide guarantees on greedy algorithms optimizing over submodular functions which is explored in Theorem 14 below.

PROPOSITION 13. [**19**, Prop. 2.7] *A positive linear combination of submodular functions is submodular.*

THEOREM 14. [**19**, Thm. 4.3] *Consider the problem of selecting K elements from a set $\mathcal{S}$ which optimizes the value of a monotonically increasing submodular cost function $f(S)$ for $S \in \mathcal{S}$ and $|S| = K$. If we make a greedy selection of R elements at each iteration, then the value of our greedy selection $f(S)$ will satisfy*

$$\frac{f(S) - f(\emptyset)}{f(S^*) - f(\emptyset)} \geq 1 - \left(\frac{q - \lambda}{q}\right)\left(\frac{q-1}{q}\right)^{q-1}, \tag{0.3.2}$$

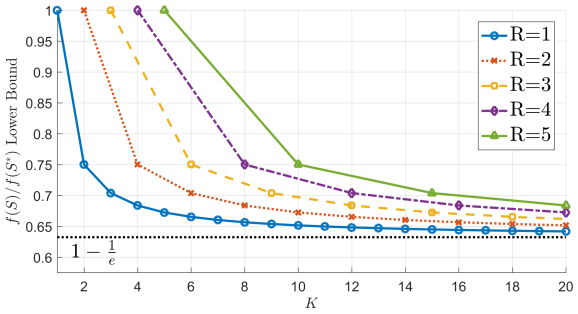

FIGURE 0.3.1. Optimality bound when performing a greedy selection of K elements over a submodular cost function, for different batch sizes R, assuming $f(\emptyset) = 0$.

where S^* is the globally optimal selection, $K = qR - p$ for some $q \in \mathbb{Z}^+$, p an integer in the range $0 \leq p \leq R-1$, and $\lambda = \frac{R-p}{R}$. When K is an integer multiple of R, the bound in Eq. (0.3.2) becomes tight. For the case when $R = 1$, Eq. (0.3.2) becomes

$$\frac{f(S) - f(\emptyset)}{f(S^*) - f(\emptyset)} \geq 1 - \left(\frac{K-1}{K}\right)^K \geq 1 - \frac{1}{e} \approx 63\%. \tag{0.3.3}$$

The last approximation is obtained in the limit as $K \to \infty$.

A consequence of Theorem 14 is that picking K items from a set one at a time using a greedy submodular heuristic, i.e., adding an element to a set which maximizes the heuristic at each step, will return a solution whose value is within approximately 37% of the optimal solution. Different bounds can be obtained by varying K and R, as demonstrated in Figure 0.3.1.

0.4. Voronoi Partitioning

In this section, we present a coarse interaction technique for the robotic testbed introduced in §0.5. This technique allows for an untrained operator to 'draw' a picture, and for a distributed set of agents to acquire a formation that coarsely represents that image, illustrated in Fig. 0.4.1.

The process we use is broken down into distinct phases, which are outlined below.

0.4.1. Initial Image Processing. When presented with a high-resolution image, e.g. from a tablet computer, we usually quantize the image resulting in 'bins' of pixel data. This

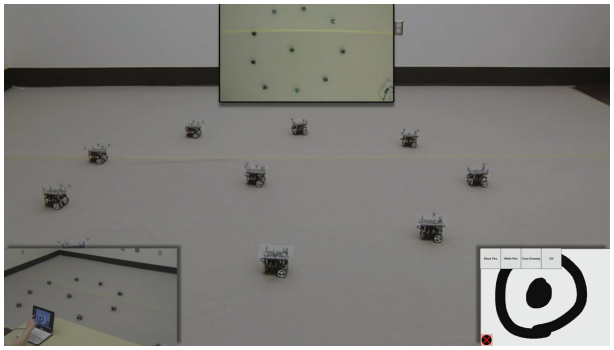

FIGURE 0.4.1. Human operator commanding a swarm using coarse inputs.

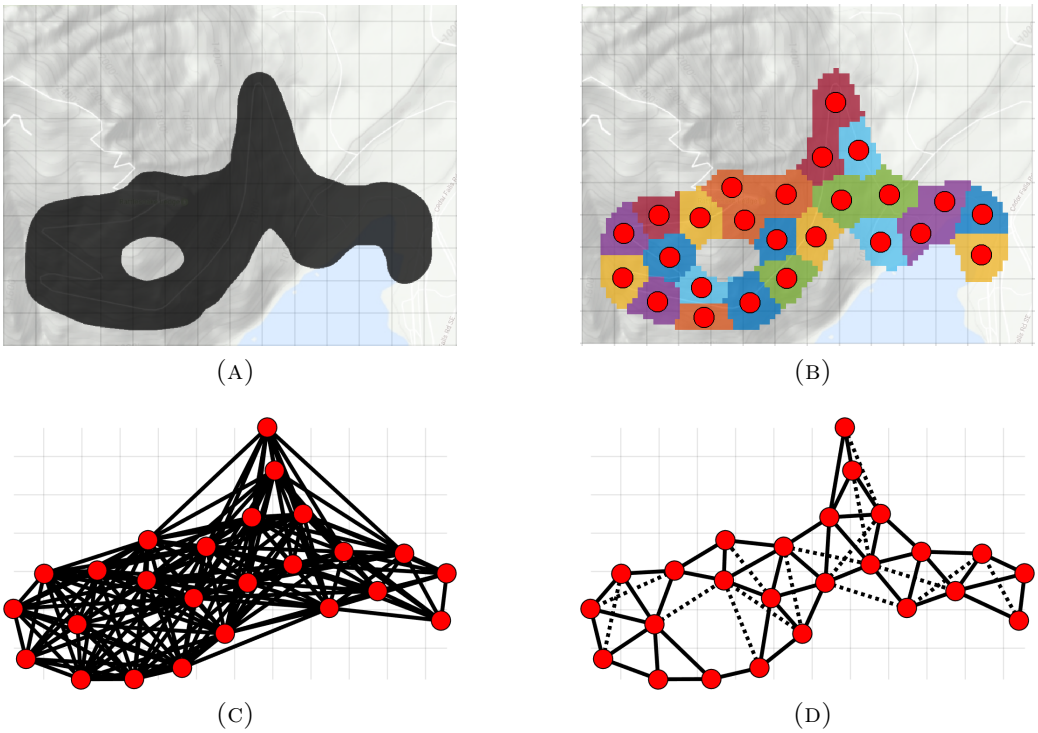

(A) (B) (C) (D)

FIGURE 0.4.2. (A) A human operator draws the formation shape on a map, and (B) a Voronoi partitioning of the agents is automatically computed. (C) A distance graph is constructed which provides the edges we will select from. (D) Edges are selected to ensure the formation has enough information to perform adequately. This selection will be explored in detail in Part 3.

step forms a coarse-grain clustering of pixels. It has the effect of accelerating many later steps since the full resolution is not needed to obtain a reasonable formation when using 10's or even 100's of agents. An example of such quantizing can seen in Figure 0.4.3.

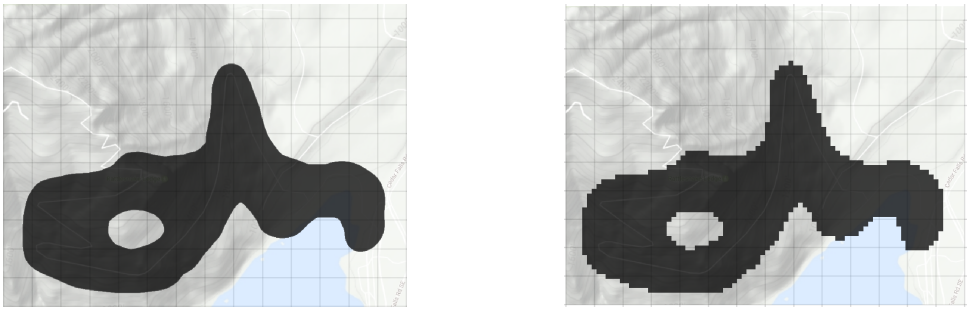

(A) (B)

FIGURE 0.4.3. (A) Original image as drawn by a human operator, and (B) quantized image with a lower resolution.

0.4.2. Distribution of Agents. To distribute agents evenly over a given formation shape, we perform the following steps:

Algorithm 1 Spread agents over an image of a formation using Voronoi partitioning.

Input: Points which define formation image: $P = \{p_1, p_2, \ldots, p_N\}$ where $p_i \in \mathbb{R}^2$

$f_1, f_2, \ldots, f_n \leftarrow n$ random elements of P
while Not converged **do**
  for $i = 1$ **to** n **do**
    $\widetilde{P}_i \leftarrow \{p_k \in P : \|f_i - p_k\| < \|f_j - p_k\| \, \forall j \neq i\}$
  end for
  for $i = 1$ **to** n **do**
    $f_i \leftarrow \frac{1}{|\widetilde{P}_i|} \sum_{p_k \in \widetilde{P}_i} p_k$
  end for
end while
return Positions of distributed agents $f \leftarrow [f_1^T f_2^T \cdots f_n^T]^T$

The process outlined in Algorithm 1 can be visualized in Figure 0.4.4.

0.4.3. Distance Graph. Once agents are distributed, we can use known communication limits to construct a distance graph. This is simply creating a graph with the node set being the agents, and the edge set being composed of all pairs of agents that are less than a certain distance apart. This process can be visualized in Figure 0.4.5.

0.5. Hardware Testbed

To support our theoretical endeavors of this research [**42, 7, 47, 48**] and of the RAIN lab as a whole [**49, 50, 51**], we validate our results with experiment. One strategy is to develop

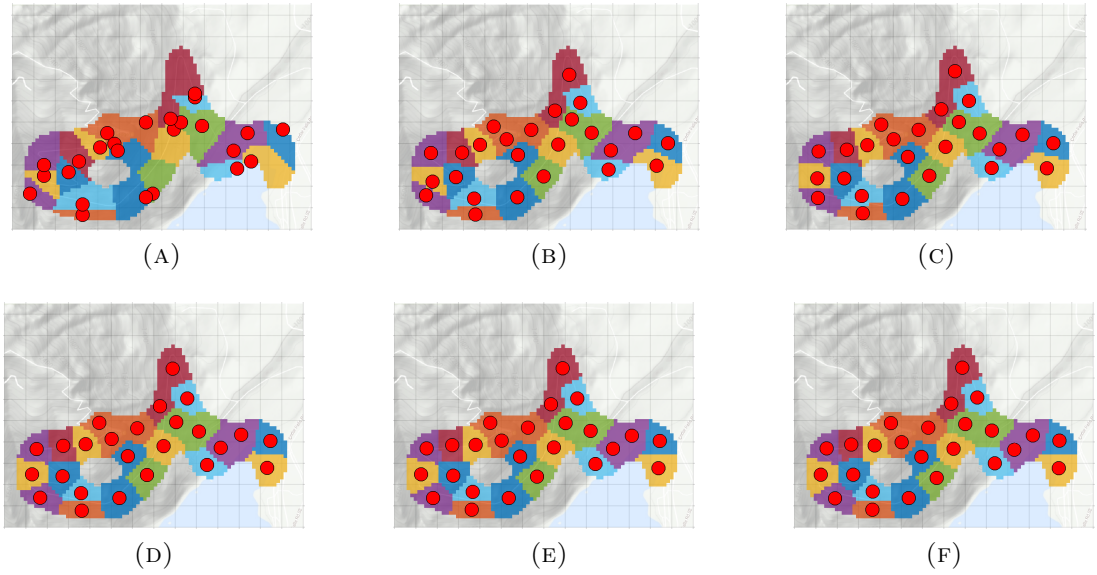

(A) (B) (C)

(D) (E) (F)

FIGURE 0.4.4. Initial iterations of the Voronoi partitioning algorithm to distribute agents on an image.

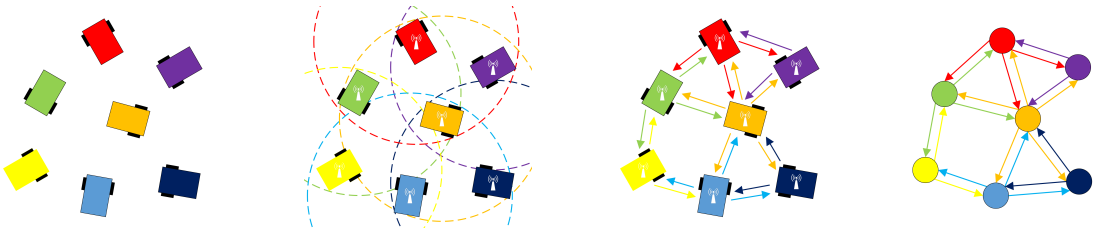

(A) (B) (C) (D)

FIGURE 0.4.5. Creating a distance graph.

high-fidelity simulations, but there is always a question of whether the simulation is accurate. If we instead can physically demonstrate algorithms, much of this doubt can be removed. There has been much work towards the development of hardware to support the broad field of networked robotics [**52, 53, 54, 55**]. In this section, we will present the robots that we have developed and used to validate our theoretical results.

Of particular interest to aerospace engineers is the canonical fixed-wing aircraft. Airplane trajectories can be challenging to develop because errors tend to result in damage or destruction of the vehicle, so we opted to design an airplane-like vehicle that has 2D dynamics that are very similar to a car, known as *unicycle dynamics*, and is detailed in §0.5.1. Control of such unicycles has been of interest to the community for some time [**56**]. Our particular

incarnation of the unicycle is addressed below. This vehicle, dubbed *Johnny*, was designed to be low-cost, easy to construct, and easy to program. Additionally it needed to have the capability to communicate with other robots nearby, and be able to easily extend its abilities, possibly with an easily applied hardware module. Different incarnations of our vehicles can be seen in Figure 0.5.1.

After building several Johnny robots which had no on-board relative sensing, one major challenge we found in demonstrating our robotic swarm algorithms was the issue of scalability. When we increase the number of robots, communication links can become saturated. This is only exacerbated by simulating sensors on a central computer, since those measurements must also be sent to the vehicles. To address this issue, we have developed a local sensor platform which can sense and communicate with the other robots in its vicinity. This sensor is called a *beacon*, and is discussed in §0.5.2. This beacon can not only detect other beacons in its vicinity, it can transmit small packets of data to aid inter-vehicle identification and other user-defined tasks.

Work on these two projects is ongoing, and relevant development milestones and current open issues will be discussed in Chapter 9.

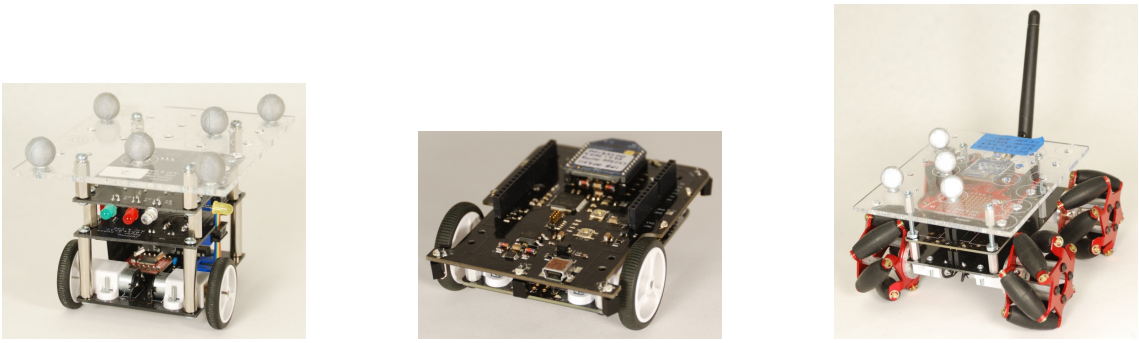

(A) (B) (C)

FIGURE 0.5.1. Variants of the "Johnny" robots: A) version 1, B) version 2, and C) omni-directional variant of version 2. Specifications can be found in Table 1.

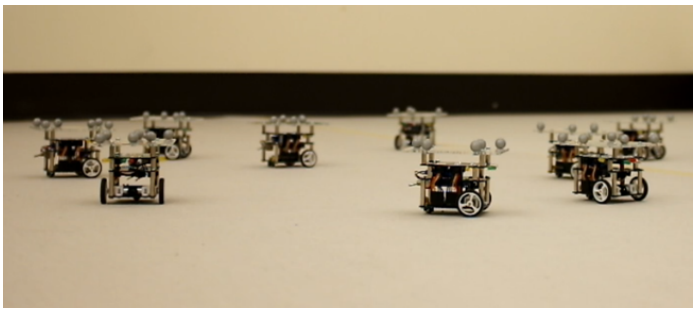

FIGURE 0.5.2. Ground vehicles used in the RAIN lab distributed hardware testbed.

0.5.1. Johnny. The robots in Figure 0.5.1A-B conform to a model called *unicycle dynamics*. A unicycle is described by the state variable

$$\mathbf{x} \triangleq \begin{bmatrix} \mathbf{r} \\ \psi \end{bmatrix} = \begin{bmatrix} r_x \\ r_y \\ \psi \end{bmatrix}, \tag{0.5.1}$$

where $\mathbf{r}$ is the position and ψ is the heading angle, and control variables

$$\mathbf{u} \triangleq \begin{bmatrix} v \\ \omega \end{bmatrix}, \tag{0.5.2}$$

where v is the magnitude of the forward velocity, and ω is the turning rate. In real-world scenarios, we will often restrict the control variables as

$$v_{\min} \leq v \leq v_{\max}$$

and

$$|\omega| \leq \omega_{\max}.$$

Our Johnny robots have limiting values of

$$\begin{aligned} v_{\min} &\approx -30^{\mathrm{cm}}/_{\mathrm{s}} \\ v_{\max} &\approx 30^{\mathrm{cm}}/_{\mathrm{s}} \\ \omega_{\max} &\approx 4\pi^{\mathrm{rads}}/_{\mathrm{s}}. \end{aligned}$$

We note that when modeling aircraft, we restrict $v_{\min} > 0$, as planes cannot reduce their forward velocity to zero in normal operation.

The unicycle dynamics are then given as

$$\dot{\mathbf{x}} = \begin{bmatrix} v\cos(\psi) \\ v\sin(\psi) \\ \omega \end{bmatrix}. \tag{0.5.3}$$

	Johnny v1	Johnny v2	Omni
$v_{\min}$	$-30^{\text{cm}}/_{\text{s}}$	$-30^{\text{cm}}/_{\text{s}}$	$-50^{\text{cm}}/_{\text{s}}$
$v_{\max}$	$30^{\text{cm}}/_{\text{s}}$	$30^{\text{cm}}/_{\text{s}}$	$50^{\text{cm}}/_{\text{s}}$
$\omega_{\max}$	$4\pi^{\text{rads}}/_{\text{s}}$	$4\pi^{\text{rads}}/_{\text{s}}$	$3\pi^{\text{rads}}/_{\text{s}}$
CPU	ATMega 328p @ 16MHz	ATMega 2560 @ 16MHz	ATMega 2560 @ 16MHz
SRAM	2kB	8kB	8kB
Analog I/O	6	6	6
Digital I/O	4	13	13
Wireless	XBee @ 115200bps	XBee @ 115200bps	XBee @ 115200bps
Battery	2S 180mAh LiPo (1 hour)	1S 1000mAh LiPo (4 hour)	9V (2 hour)
Charging	χ	✓	χ
JTAG Debugging	χ	✓	✓
PCB Count	3	1	2
Cost Each	$60	$80	$175

TABLE 1. Specifications for the different variants of robots which comprise our robotic testbed.

Often, we would like a vehicle conforming to the unicycle dynamics to move to a prescribed point $\tilde{\mathbf{r}}$. To do this, we modify a controller originally proposed by Aciardi *et al.* [**57**] as

$$\begin{aligned} v &= k_d d \cos(\beta) \\ \omega &= k_\psi \beta \left(1 + d^2\right) - \frac{1}{2} k_d \sin(2\beta), \end{aligned}$$

where

$$d \triangleq \|\tilde{\mathbf{r}} - \mathbf{r}\|,$$

$$\beta \triangleq \text{atan2}(\tilde{\mathbf{r}} - \mathbf{r}) - \psi,$$

and k_d and k_ψ are positive gains.

The specifications for the robots themselves are listed in Table 1.

0.5.2. Beacon. As mentioned in the previous section, when robotic formations scale past a certain size, communicating becomes a challenge due to wireless bandwidth constraints. To help alleviate these constraints, we developed a sensor for our ground vehicles that could sense other neighboring vehicles directly, leaving the wireless channels open for

more important tasks. The physical beacon can be seen in Figure 0.5.3. The hardware itself consists of infra-red LED 'emitters', infra-red photodiode 'detectors', filter and amplifier circuitry, as well as an independent processor.

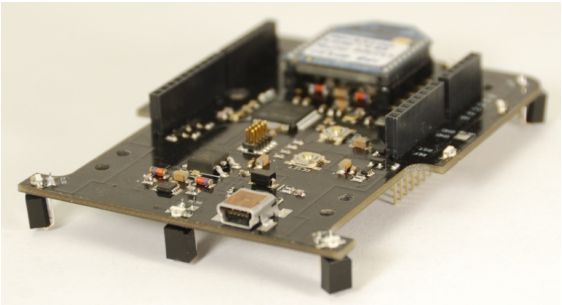

FIGURE 0.5.3. Beacon shield for the Johnny v2 robots.

In order to calibrate the sensor model, we took two vehicles with beacons equipped, and drove them around each other in different patterns and simply recorded the incoming signals at each detector.

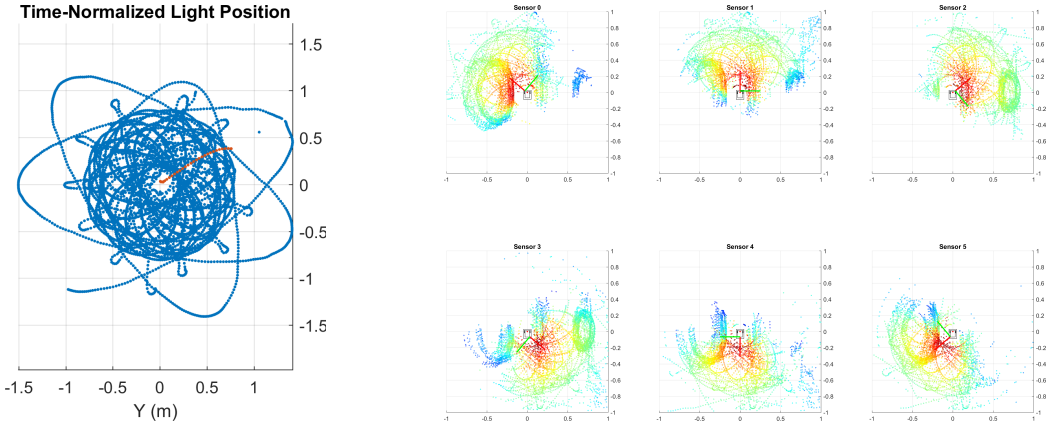

(A) (B)

FIGURE 0.5.4. (A) Path of vehicles during data gathering, and (B) strength of all observations gathered at each sensor.

We assume that all detectors have an approximately equal response. Thus, we can translate all observations from Figure 0.5.4b into a common frame, as seen in Figure 0.5.5a. Further, we assume that the sensors exhibit symmetry in the radial direction, so we mirror all observations, as seen in Figure 0.5.5b. This is the data to which we fit our model.

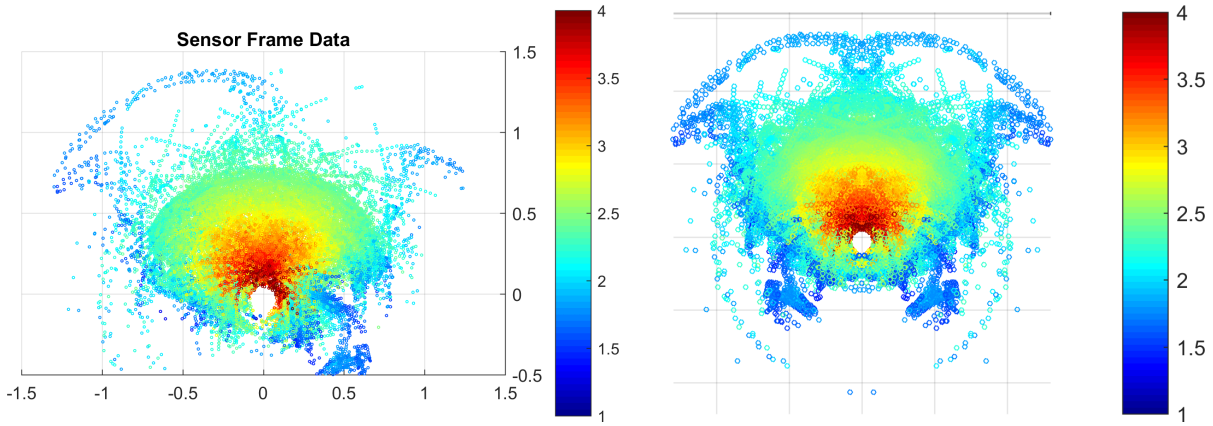

(A) (B)

FIGURE 0.5.5. Beacon detector observation data.

The model we are choosing to fit incorporates both angular and distance terms, and has the form of

$$\begin{aligned} h(r,\theta) &\triangleq h_r(r,\theta)\, h_\theta(r,\theta) \\ h_r(r,\theta) &\triangleq \alpha_1 r e^{\alpha_2 r^{\alpha_3}+\alpha_4} \\ h_\theta(r,\theta) &\triangleq \alpha_5 \cos\left(\frac{1}{2}\theta\right) + \alpha_6 \cos(4\theta) + \left(\frac{1-\cos(\theta)}{2}\right)^{\alpha_7} + 1. \end{aligned}$$

When we perform the nonlinear fit, we arrive at parameters

$$\begin{aligned} \alpha_1 &= 3.63 \\ \alpha_2 &= -9.84 \\ \alpha_3 &= 0.15 \\ \alpha_4 &= 7.95 \\ \alpha_5 &= 2.91 \\ \alpha_6 &= -0.11 \\ \alpha_7 &= 7.88. \end{aligned}$$

The resulting sensor model can be seen in Figure 0.5.6a, and the residual errors from this fit can be seen in Figure 0.5.6b.

This sensor model, coupled with the dynamic model of the vehicle presented above, can be used to construct a Kalman filter to track neighboring agents and is one of the subjects of future work.

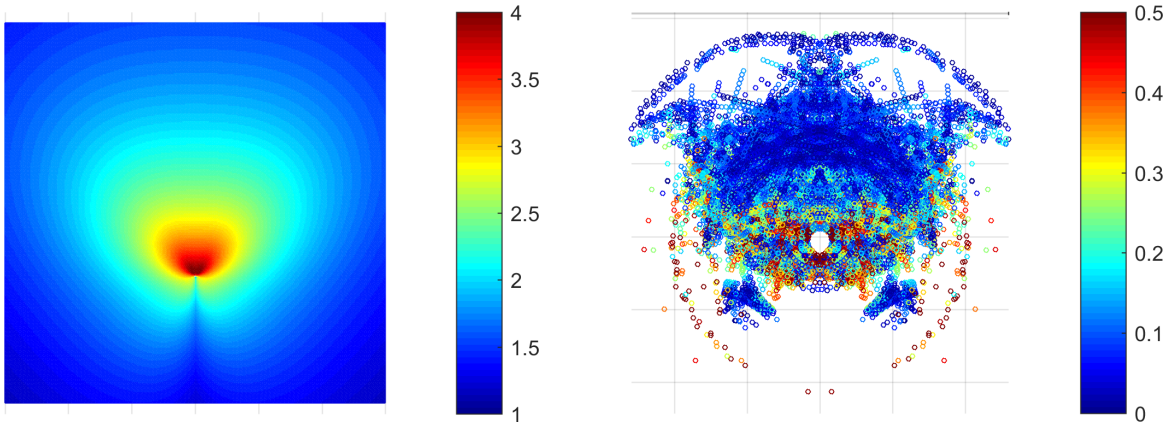

(A) (B)

FIGURE 0.5.6. Beacon (A) sensor model with (B) residual error.

Part 1

From Dynamics to Coarse Control

This part explores notion of 'coarse control' for distributed protocols. Commonly for control, a continuous signal $\mathbf{u}(t)$ is designed, for example through feedback $\mathbf{u}(\mathbf{x}(t))$, that will affect a state $\mathbf{x}(t)$ through the dynamics

$$\dot{\mathbf{x}}(t) = f(\mathbf{x}(t)) + \mathbf{u}(\mathbf{x}(t)).$$

We examine a more 'coarse grained' approach whereby only discrete control decisions can be made that have the effect of shifting the dynamics from the current mode of operation to a more desirable ith mode of operation with passive dynamics

$$\dot{\mathbf{x}}(t) = f_i(\mathbf{x}(t)).$$

Over relative few control decisions, and corresponding modes, this notion of coarse control must navigate through the landscape of passive dynamics to attain some desired behavior.

In Chapter 1, we will examine a load-balancing application that is relevant to managing robotic workers in a factory. In this case, a human operator may want to change the distribution of robots without having to explicitly assign robots to tasks or even know what the distribution of agents in the full system is. The proposed coarse control involves changing the weights on an internal graph topology, and allowing the passive dynamics to attain the desired agent distribution.

In Chapter 2, we investigate a more abstract example, with a control objective to acquire desired phase alignment, referred to as pattern control, of a set of coupled electrical oscillators using coarse intermittent control of the dynamics. In this case, the system dynamics are on a much shorter time-scale than the control, and so a switching controller relies heavily on the stability of the dynamics to shift between patterns. The specific coarse control involves adapting the graph topology, as well as the relative degree of coupling between agents adjacent in the graph. A novel Markov decision process (MDP) formulation is used to generate a high-level switching controller for this problem.

CHAPTER 1

Advection

The motivation and formulation of distributed multi-vehicle dynamics can come from many sources. One such inspiration is fluid flow dynamics which, when discretized on a particle-scale form a distributed dynamics. Consensus, a popular distributed multi-agent dynamics, can be formulated as the discretization of the diffusion dynamics PDE. Consensus provides an effective model for distributed information-sharing and coordination with application in formation control, swarming phenomenon and distributed estimation; see for example [**1, 58**]. Fluid-flow advection dynamics shares many similarities to diffusion and may be interpreted as diffusion in a flow field. An appeal of the advection framework is that it leads to locally-based interaction dynamics that can produce global network characteristics. Further, the performance characteristics are coupled to the underlying network structure.

As the discretization of the advection dynamics has the effect of inducing a conserved flow through the directed edges in the graph, the state sum across agents is conserved for all time. It is this property, as well as the ability to tune the equilibrium subspace, that makes advection dynamics attractive for coarse manipulation. Advection has been used to model the spread of diseases [**2**], population migration [**24**], and supply and demand in economic systems [**25**], and recently applied to formation control and a sensor coverage problem by the authors in [**26**].

The advection dynamics were independently studied by Berman *et al.* [**59**] and stochastically simulated for task allocation. In this section, we highlight some of the features that complement this work and implement a load balancing application on a robotics testbed. We begin by defining advection dynamics and characterize its state matrix, dynamics and equilibrium, with a particular focus on the underlying graph structure. We highlight some of the

features of advection that make it appropriate for decentralized load balancing application and coarse control. We support this analysis with examples.

1.1. Background and Model

The advection equation, also known as the transport equation, involves a scalar concentration u of a material affected by a flow field $\mathbf{v}$. The flux of the advection process is $F = \mathbf{v}u$.

In a discrete calculus analogue of the advection equation, we first define an interaction graph (directed and weighted) over nodes based on the flow $\mathbf{v}$. The flow vector $\mathbf{v}$ dictates the interactions between nodes by defining directed edges and edge weights. We then adopt a discretized view of the flux $\mathbf{v}u$ through an edge $i \to j$ as consisting of the flow w_{ji} prescribed by $\mathbf{v}$ at the edge modified by the concentration x_i prescribed by u at node i. The flow along edge $i \to j$ is consequently $w_{ij}x_i(t)$. The concentration at node i at time t is denoted $x_i(t)$. The flux of node i is then the flow into the node minus the flow out of the node, i.e.,

$$\dot{x}_i(t) = -\sum_{(i,j)\in E} w_{ij}x_i(t) + \sum_{(j,i)\in E} w_{ji}x_j(t). \tag{1.1.1}$$

These dynamics are well suited to a graph theoretic analysis. As such, we proceed by presenting some graph theory background and rewrite the dynamics (1.1.1).

We can now rewrite our dynamics (1.1.1) using these graph concepts with the flow $\mathbf{v}$ generating the digraph $\mathcal{D}(\mathbf{v}) = (V, E(\mathbf{v}), W(\mathbf{v}))$, where a flow from node i to j is encoded as $(i,j) \in E$ with edge weight $w_{ji} \in W$. For brevity, we will denote the digraph as $\mathcal{D} = (V, E, W)$. The advection dynamics can therefore be written with respect to the out-degree Laplacian as

$$\dot{\mathbf{x}}(t) = -\mathcal{L}_{\text{out}}(\mathcal{D})\mathbf{x}(t). \tag{1.1.2}$$

We proceed to examine system characteristics of the advection dynamics relevant to load balancing.

1.2. Load Balancing and Advection Properties

Load balancing is a rich area of research with varied applications from mobility-on-demand systems to the reallocation of resources in a business [**59, 60, 61, 62**]. The advection protocol is well-suited for application to decentralized load balancing, which is illustrated with r ground vehicles corresponding to the load and n ground markers corresponding to the nodes. The global objective is to attain a pre-selected distribution of vehicles at each node.

For load balancing applications, the advection dynamics must be quantized and so generally the exact equilibrium can not be reached. Instead, a close integer solution is guaranteed. We refer to the paper by Kashyap *et al.* [**63**] for the larger set of equilibrium generated by quantization consensus dynamics; a similar results can be attained for the advection dynamics. Typically, load balancing for centralized approaches scales poorly with the number of nodes, and decentralized approaches often require performance validation through simulation [**61, 62**]. For our application, each iteration of the protocol requires $|E|$ operations and r communications. The algorithm has a computational complexity of $\mathcal{O}\left(\text{diam}(\mathcal{G})\,|E|\right)$ and communication complexity of $\mathcal{O}\left(\text{diam}(\mathcal{G})r\right)$, distributed across the n nodes of the graph.

The following are properties that support a load balancing application with omitted proofs included in [**26, 48**]. Invariant features of advection are positive invariance and state sum conservation summarized in the following propositions. These properties ensure that while the protocol is running every portion of the total load will be assigned to some node.

PROPOSITION 15. [**26**, Prop. 8] *The advection dynamics are positively invariant over $x_i \geq 0$ for all $i \in V$, i.e., if $x_i(0) \geq 0$ for all $i \in V$ then $x_i(t) \geq 0$ for all $i \in N$ for all $t > 0$.*

PROPOSITION 16. [**26**, Prop. 1] *The advection dynamics (1.1.2) are (state) sum conservative, i.e., $\sum_{i=1}^{n} x_i(t) = \sum_{i=1}^{n} x_i(0)$ for all time t.*

The following proposition characterizes the equilibrium for the advection dynamics where $\mathcal{D}$ is strongly connected. The proposition states that if there is a path from each node to every other node, the dynamics will converge to an equilibrium. Further, if load is removed from

the system, the dynamics will adapt and re-distribute the remaining load, making it robust to load variability.

PROPOSITION 17. [**26**, Prop. 9]*For a strongly connected digraph $\mathcal{D}$, the advection dynamics (1.1.2), initialized from $\mathbf{x}(0) = \mathbf{x}_0$, satisfies*

$$\lim_{t\to\infty} \mathbf{x}(t) = \frac{1}{\sqrt{n}} \left(\mathbf{1}^T \mathbf{x}_0\right) \mathbf{z} := \mathbf{z}_{nom}(\mathbf{x}_0),$$

where $\mathbf{z} = \mathbf{sgn}(\bar{z}_1)\, \bar{\mathbf{z}} / \|\bar{z}\|_2$ and $\mathcal{L}_{\text{out}}(\mathcal{D})\bar{\mathbf{z}} = \mathbf{0}$. Further, $z_i > 0$ for all $i \in V$ and graphically $\bar{\mathbf{z}}_i = \sum_{T\in\mathcal{T}_i} \prod_{(i,j)\in T} w_{ij}$, where $\mathcal{T}_i$ is the set of spanning trees of $\mathcal{D}$ rooted at node i.

Proposition 15 and 17 result from a zero eigenvalue of the advection dynamics. The eigenvector corresponding to this mode presents a direction of perturbation that the advection dynamics will not correct namely $\sum_{i=1}^n x_i(t)$. This invariance can be exploited to control the position on the invariant subspace defined by $\mathcal{Z} = \{\alpha\mathbf{z} : \alpha \in \mathbb{R}\}$. Perturbing any subset of nodes in the network by the additive signal $\tilde{u}(t)$ applied over the time from $[0, T]$, the convergence point in $\mathcal{Z}$ can be directly controlled by the accumulative control signal $\gamma := \mathbf{1}^T \int_0^T \tilde{\mathbf{u}}(t)dt$ as

$$\begin{aligned}\lim_{t\to\infty} \mathbf{x}(t) &= \frac{1}{\sqrt{n}} \left(\mathbf{1}^T\mathbf{x}_0 + \mathbf{1}^T \int_0^T \tilde{\mathbf{u}}(t)dt\right) \mathbf{z} \\ &= (1+\gamma)\, \mathbf{z}_{\text{nom}}(\mathbf{x}_0).\end{aligned}$$

This represents a coarse method of control with only access to a single node required. Further, local feedback can be applied to acquire a desired $\mathbf{z}^* \in \mathcal{Z}$ through an additive feedback term $\tilde{u}_i = -k_i(x_i(t) - z_i^*)$ with $k_i > 0$ for each node i which is directly controlled with the signal $\tilde{u}_i$ and $k_i = 0$ otherwise. This follows from the property $L_{\text{out}}(\mathcal{D})\mathbf{z}^* = \mathbf{0}$, and reformulating the dynamics in matrix form as

$$\begin{aligned}\dot{\mathbf{x}}(t) &= -\mathcal{L}_{\text{out}}(\mathcal{D})\mathbf{x}(t) + \tilde{\mathbf{u}} \\ &= -\mathcal{L}_{\text{out}}(\mathcal{D})\mathbf{x}(t) - \mathcal{D}_i\,[k_i](\mathbf{x}(t) - \mathbf{z}^*)\end{aligned}$$

$$\frac{d}{dt}(\mathbf{x}(t) - \mathbf{z}^*) = -\left(\mathcal{L}_{\text{out}}(\mathcal{D}) + \mathcal{D}_i\left[k_i\right]\right)(\mathbf{x}(t) - \mathbf{z}^*)$$

and the positive definiteness of $\mathcal{L}_{\text{out}}(\mathcal{D}) + \mathcal{D}_i\left[k_i\right]$ indicates the dynamics converge exponentially to $\lim_{t\to\infty} \mathbf{x}(t) - \mathbf{z}^* = \mathbf{0}$.

An alternative coarse control mechanism is one that uses the graph's edge weights as a controller to change the invariant subspace $\mathcal{Z}$. The result follows from the Proposition 17, summarized in the following corollary, states that if $\mathcal{D}$ is strongly connected then the edges of $\mathcal{D}$ can be re-weighted so that the advection dynamics converges to an arbitrary positive set of equilibrium.

COROLLARY 18. *For a strongly connected $\mathcal{D} = (V, E, [w_{ij}])$, the equilibrium set is $\frac{1}{z_1}x_1 = \frac{1}{z_2}x_2 \cdots = \frac{1}{z_n}x_n$, where z_i is defined in Proposition 17. A new equilibrium set $\alpha_1 x_1 = \alpha_2 x_2 = \cdots = \alpha_n x_n$ where $\alpha_i > 0$, for all $i \in V$, can be achieved by re-weighting the edges of $\mathcal{D}$ forming a new graph $\widetilde{\mathcal{D}} = (V, E, [\widetilde{w}_{ij}])$, with the weights $\widetilde{w}_{ji} = \frac{\alpha_i}{z_i} w_{ji}$ for all $(i, j) \in E$.*

Hence, for strongly connected $\mathcal{D}$, the set $\mathcal{Z}(w)$ can be dynamically reweighted if higher loads are required at a particular node i, by decreasing the weights w_{ji} for all $(i, j) \in E$. This is a local redesign technique that only requires the adjust the outgoing edges of node i. A coarse input indicating an increase in desired load can be simply translated to decrease in α_i in Corollary 18.

1.3. Concluding Remarks

Properties of the linear advection dynamics were explored with a specific focus on its suitability for coarse input control. Of particular interest was the invariant features of the dynamics and how it related to the underlying network topology structure. A simple edge reweighting mechanism was proposed as an effective method to coarsely control the desired load balancing performance of the dynamics.

This approach of adapting the network as a coarse method for control is further explored in the following chapter with the objective of acquiring desired patterns in nonlinear coupled oscillators dynamics.

CHAPTER 2

MDP Switching Control

Phase synchronization in coupled oscillators is an extensive area of research [**27, 30, 28, 64**]. Less studied but still prominent in the literature is the examination of other types of patterns in networks of oscillators [**31**]. A pattern occurs when the frequency of all oscillators synchronize, or equivalently their phases lock, with the phase separation between oscillators describing the type of pattern. These equilibriums are referred to as incoherent states or, if the oscillators' phases are evenly distributed on the unit circle, balanced states [**27**]. In biological systems these different patterns give rise to different temporal and spatial collective behavior, for example in the flashing of fireflies, heart's pacemaker cells, brain neurons, and fish schooling [**32**]. Addressed in this work is a network topology-based method to control the pattern exhibited by networks of oscillators.

Multiple balanced states have been characterized for cycles of oscillators, or more generally for circulant networks running the Kuramoto dynamics [**65, 2**]. Zhihao *et al.* relaxed the Kuramoto sine-coupling dynamics to a cosine-coupling focusing on balanced configured equilibrium so that a convoy of robots could be equally distributed about a moving target [**66**]. Motivated by the variations of Kuramoto dynamics for oscillator power networks, Dörfler and Bullo [**28**] analyzed an extended version of the Kuramoto dynamics with non-uniform coupling, phase shifts and frequencies. We consider a variation of the Kuramoto form to include amplitude and phase dynamics, specifically the discrete form of the real Ginzburg-Landau equation.

With origins in the theory of superconductivity, the Ginzburg-Landau equation describes universal features of systems near a Hopf bifurcation [**31, 67**]. These dynamics have appeared in a myriad of naturally occurring phenomenon including binary fluid convection [**68**], laser physics [**69**], bluff body wakes [**70**], mechanical systems and chemical turbulence [**71**]. The

prototypical real Ginzburg-Landau equation takes the form

$$\dot{A} = A - |A|^2 A + \nabla^2 A \tag{2.0.1}$$

where $A(x,t)$ is a complex function, defined over a spatially infinite x in one dimension. We will examine the discretized form of these dynamics, dubbed the *graph Ginzburg-Landau* dynamics, over a finite number of oscillators coupled through a network graph. This approach is similar to the creation of consensus dynamics and graph advection dynamics from discretized diffusion and advection dynamics [**26**]. This PDE to graph-based conversion of the Ginzburg-Landau dynamics has been successfully adapted for classification and image processing in the PDE-based image community for high dimensional datasets [**72**]. We focus on examining this discrete dynamics over a cycle graph which exhibit multiple balanced state equilibria. Each of these equilibrium states has varying sized basins of attraction, making some states more challenging than others to acquire from a random initial condition. The objective of this work is to use topology rewiring as a pattern control mechanism to drive the discrete Ginzburg-Landau dynamics to a desired balanced state equilibrium.

Previous work in the area of pattern control or equilibrium switching in oscillators fall under the classes of non-feedback control strategies and feedback control strategies. The former control strategy acts via an external perturbation such as a short pulse, a pseudo-periodic or harmonic forcing signal [**33, 34**]. These methods are in general easy to apply, since they do not require intimate knowledge of system dynamics. The control is usually not efficient in the sense that the amplitude of the external signal is relatively large. The other successful method is to use feedback techniques where the internal state of the system is fed back into the dynamics either instantaneously or with a time delay [**32**]. Feedback schemes typically boast smaller external signals but can be more challenging to implement experimentally as continuous signal perturbations are required. The attraction of topological rewiring is that it represents a marriage of these two classes of control. Rewiring is a discrete event but induces a new set of feedback mechanisms in the network due to the new couplings produced or removed between edges.

Our pattern control method consists of rewiring the graph into different disconnected cycle subgraph configurations. Each of these configurations exhibit their own distinct balanced states, which individually are easier or harder to achieve based on their differently sized regions of attraction. Hence, from a random initial condition, acquiring a selected final balanced state can be more likely via an intermediate disconnected cycle topology balanced state. As equilibria in disconnected oscillator networks can randomly drift relative to one another, transitions to a final state under topological rewiring is non-deterministic. Hence, the topology rewiring problem can be modeled as a discrete time stochastic control process, or more specifically, a Markov decision process (MDP) [**73, 74**]. An optimal MDP policy would then outline the selection of topologies, *MDP actions*, that would more likely achieve a desired final balanced state, with a corresponding *MDP reward*.

2.0.1. Background. We introduce some brief notation that is unique to this chapter. The n node cycle graph, denoted as $\mathcal{C}_n$, is defined using the edges $\{1, n\}$ and $\{i, i+1\}$ for $i = 1, \ldots, , n-1$. The kth eigenvector of $\mathcal{L}(\mathcal{C}_n)$ is $\mathbf{v}_k = \frac{1}{\sqrt{n}} \begin{bmatrix} 1 & \omega_k & \omega_k^2 & \cdots & \omega_k^{n-1} \end{bmatrix}^T$ where $\omega_k = \exp(2\pi kj/n)$, the associated eigenvalue $\lambda_k(\mathcal{C}) = 2 - 2\cos(2\pi kj/n)$, and j is the imaginary number.

2.0.2. Dynamics. The Ginzburg-Landau equation (2.0.1) can be generalized by sampling the vector space $A(x,t)$ discretely at complex states $x_1, \ldots, x_n \in \mathbb{C}$. The spatial gradient operator ∇^2 is subsequently replaced with a more general gradient operator on graph $\mathcal{G}$. The state of oscillator i can be represented by the complex number $x_i = a_i e^{j\theta_i}$ with amplitude a_i and phase θ_i. Applying the diffusive gradient operator with coupling strength of $\beta \in \mathbb{R}$, the dynamics for oscillator $i \in [n]$ becomes

$$\begin{aligned} \dot{x}_i &= x_i - |x_i|^2 x_i - \beta \sum_{k \in \mathcal{N}(i)} (x_k - x_i) \\ &= x_i - |x_i|^2 x_i + \beta \mathcal{L}_i(\mathcal{G}) x. \end{aligned} \tag{2.0.2}$$

We refer to dynamics (2.0.2) as the graph Ginzburg-Landau dynamics to distinguish it from its continuous form. For this paper we will consider so-called *weak coupling* between oscillators, letting $|\beta| \leq 1/2$.

The dynamics (2.0.2) can also be written in an amplitude and phase form by differentiating the relationship $x_i = a_i e^{j\theta}$. For $x_i \neq 0$ then,

$$\begin{aligned} \dot{x}_i &= \dot{a}_i e^{j\theta_i} + \dot{\theta}_i j a_i e^{j\theta_i} = \dot{a}_i \frac{x_i}{|x_i|} + j\dot{\theta}_i x_i \\ \frac{\dot{x}_i}{x_i} &= \dot{a}_i \frac{1}{a_i} + j\dot{\theta}_i. \end{aligned} \tag{2.0.3}$$

From dynamics (2.0.2),

$$\begin{aligned} \frac{\dot{x}_i}{x_i} &= 1 - a_i^2 - \beta \sum_{k \in \mathcal{N}(i)} \left(\frac{a_k e^{j\theta_k}}{a_i e^{j\theta_i}} - 1 \right) \\ &= 1 - a_i^2 - \beta \sum_{k \in \mathcal{N}(i)} \left(\frac{a_k}{a_i} e^{j(\theta_k - \theta_i)} - 1 \right) \\ &= 1 - a_i^2 - \beta \sum_{k \in \mathcal{N}(i)} \left(\frac{a_k}{a_i} \cos(\theta_k - \theta_i) - 1 \right) \\ &\quad -j\beta \sum_{k \in \mathcal{N}(i)} \frac{a_k}{a_i} \sin(\theta_k - \theta_i). \end{aligned} \tag{2.0.4}$$

Equating the real and imaginary parts in (2.0.3) and (2.0.4) then the graph Ginzburg-Landau equation is equivalent to

$$\begin{aligned} \dot{a}_i &= \left(1 - a_i^2\right) a_i - \beta \sum_{k \in \mathcal{N}(i)} \left(a_k \cos(\theta_k - \theta_i) - a_i \right) \\ \dot{\theta}_i &= \beta \sum_{k \in \mathcal{N}(i)} \frac{a_k}{a_i} \sin(\theta_i - \theta_k). \end{aligned} \tag{2.0.5}$$

There are notable similarities between the phase dynamics and the Kuramoto dynamics [**27**], with equivalence when the amplitudes are restricted to be synchronized. We observe that under the transformation $\theta_i \to \theta_i + \omega t + \gamma$ for $\omega \in \mathbb{R}$ the amplitude dynamics are invariant

and

$$\dot{\theta}_i \to \omega + \beta \sum_{k \in \mathcal{N}(i)} \frac{a_k}{a_i} \sin\left(\theta_i - \theta_k\right). \tag{2.0.6}$$

The transformed dynamics correspond to a limit cycle version of the dynamics, rotating at a rate of ω. Further, the dynamics exhibit global phase symmetry and so equilibria of the dynamics are semi-stable with respect to rotations.

2.0.3. Markov Decision Processes (MDPs). Markov decision processes provide a framework for discrete time stochastic control [**74**]. They present an efficient method for modeling decision making in problems where outcomes are only known stochastically. An MDP is encoded in the 4-tuple $(\mathcal{S}, \mathcal{A}, \mathcal{T}, \mathcal{R})$, representing the system states, actions, transition probabilities and rewards, respectively. More precisely, at discrete time steps, a decision maker is given a finite state $s \in \mathcal{S}$, after which the decision maker must select a finite, and available action $a \in \mathcal{A}$. Given the state and action pair, there is a known probability that the action will transition to state $s' \in \mathcal{S}$ at the following time step which is encoded in $\mathcal{T}(s, s', a)$. Here, $\mathcal{T}$ is assumed to be Markovian, namely

$$\mathcal{T}(s, s', a) = \Pr\left(s_{t+1} = s' \,:\, s_t = s, a_t = a\right). \tag{2.0.7}$$

Following the transition to state $s' \in \mathcal{S}$ under the action $a \in \mathcal{A}$ the decision maker is then rewarded with $\mathcal{R}(s', a)$. The objective of MDPs is to find an optimal policy $\pi(s)$ for the decision maker, where $\pi(s) : \mathcal{S} \to \mathcal{A}$ specifies an action given the current state. A common function to measure the optimality the policy π is the expected discounted sum cost

$$J = \sum_{t=0}^{\infty} \gamma^t \mathcal{R}(s_{t+1}, \pi(s_t)), \tag{2.0.8}$$

where $\gamma \in [0, 1)$ is the discount factor. The appeal of this formulation is that it can be solved efficiently by linear programming or dynamic programming [**73**].

2.1. Pattern Characterization

This section characterizes the balanced equilibrium of the graph Ginzburg-Landau dynamics (2.0.2). The equilibrium states for a given graph topology will form the states of the MDP which are examined in §2.2, with the objective of acquiring a particular equilibrium pattern. Similar to the Kuramoto dynamics, the graph Ginzburg-Landau dynamics over cycle graphs can exhibit multiple balanced equilibria, where neighboring oscillators are equally distributed about the unit circle. For compact representation, we introduce the cycle balanced equilibrium notation $\mathcal{C}_V^k$, or $\mathcal{C}_{v_1,\ldots,v_n}^k$, which denotes the kth balanced equilibrium of the cycle graph on the nodes in the ordered set $V = (v_1, \ldots, v_n)$ with edges $\{v_i, v_{i+1}\}$ (mod n). The kth balanced equilibrium corresponds to a phase separation of

$$\theta_{i+1} - \theta_i = 2\pi k/n$$

between nodes v_{i+1} and v_i for all $i \in [n]$.[1] A sample of this notation is displayed in Figure 2.1.1.

To establish the stability of balanced states in the graph Ginzburg-Landau equation we examine the continuous Ginzburg-Landau free energy

$$F = \int \left(-|A|^2 + \frac{1}{2}|A|^4 + |\nabla A|^2 \right) dx,$$

which can be adapted to form a global Lyapunov potential for (2.0.2).

THEOREM 19. *The graph form of the Ginzburg-Landau free energy*

$$\begin{aligned} V &= \sum_{i=1}^{n} \left(-(x_i x_i^*) + \frac{1}{2}(x_i x_i^*)^2 \right) - \beta x^* \mathcal{L} x \\ &= \sum_{i=1}^{n} \left[-a_i^2 + \frac{1}{2} a_i^4 \right] - \beta \sum_{k \in \mathcal{N}(i)} \left(a_i^2 + a_k^2 - 2 a_k a_i \cos(\theta_i - \theta_k) \right) \end{aligned} \tag{2.1.1}$$

is a global Lyapunov potential for the graph Ginzburg-Landau dynamics (2.0.2).

[1] It should be noted that $\mathcal{C}_V^k$ is equivalent to $\mathcal{C}_V^{k+\bar{k}n}$ for $\bar{k} \in \mathbb{Z}$, due to the periodicity of cosine.

PROOF. Noting that $\beta x^* \mathcal{L} x \geq 0$ for $\beta \geq 0$ or for $\beta < 0$ then $\beta x^* \mathcal{L} x \geq \beta \lambda_{\max} \sum_{i=1}^{n} (x_i x_i^*)$. As

$$V \geq \sum_{i=1}^{n} -(x_i x_i^*) + \frac{1}{2}(x_i x_i^*)^2 - |\beta| \lambda_{\max}(x_i x_i^*);$$

hence V is bounded from below and is a valid Lyapunov function candidate. Differentiating V with respect to x^* and x, then

$$\frac{\partial V}{\partial x^*} = -x + \operatorname{diag}\left[(x_1 x_1^*) x_1, \ldots, (x_n x_n^*) x_n\right] - \beta \mathcal{L} x = -\dot{x},$$

and similarly $\frac{\partial V}{\partial x} = -\dot{x}^{T*}$. Hence,

$$\dot{V} = \frac{\partial V}{\partial x^*}\dot{x}^{T*} + \frac{\partial V}{\partial x}\dot{x} = -\dot{x}^T \dot{x}^{T*} - \dot{x}^* \dot{x} = -2\sum_{i=1}^{n} |\dot{x}_i|^2,$$

which is strictly negative except for $\dot{A} = 0$ and so is a valid Lyapunov function for dynamics (2.0.2). Formulating V in amplitude and phase form with $V_a = \sum_{i=1}^{n} \left[-a_i^2 + \frac{1}{2}a_i^4\right]$,

$$\begin{aligned} V &= \sum_{i=1}^{n} \left[-(x_i x_i^*) + \frac{1}{2}(x_i x_i^*)^2\right] - \beta x^* \mathcal{L} x \\ &= V_a - \beta \sum_{k \sim i} \left(a_i e^{j\theta_i} - a_k e^{j\theta_k}\right)^* \left(a_i e^{j\theta_i} - a_k e^{j\theta_k}\right) \\ &= V_a - \beta \sum_{k \sim i} \left(a_i^2 + a_k^2 - a_k a_i \left[e^{j(\theta_i - \theta_k)} + e^{j(\theta_k - \theta_i)}\right]\right) \\ &= V_a - \beta \sum_{k \sim i} \left(a_i^2 + a_k^2 - 2a_k a_i \cos(\theta_i - \theta_k)\right). \end{aligned}$$

□

Examining the potential (2.1.1), for $\beta < 0$, V admits a global minimum when $x^* \mathcal{L} x = 0$. For a connected $\mathcal{G}$, as the right null space of $\mathcal{G}$ is spanned by $\mathbf{1}$, this condition is satisfied when $x = \mathbf{1} e^{i\theta_0}$ for some $\theta_0 \in \mathbb{R}$. This equilibrium represents the fully synchronized state with all oscillators phase locked $\theta_i = \theta_{i+1} \pmod{n}$ for all $i \in [n]$ and the amplitudes are on the unit circle. The equilibrium is present irrespective of the underlying graph topology. The occurrence of other balanced equilibria for our specific graph of interest, the cycle graph, is examined in the following theorem. The stability property addressed is set stability with

respect to the set represented by the balanced state; as discussed in §2.0.2, the dynamics are invariant to rotation.

THEOREM 20. *For the cycle graph, the balanced state* $\mathcal{C}^k_{[n]}$ *with a common oscillator amplitude of* $\bar{a} = \sqrt{1 + 2\beta\left(1 - \cos 2\pi k/n\right)}$ *is an equilibrium of dynamics (2.0.2) for* $|\beta| \leq \frac{1}{2}$. *Further,* $\mathcal{C}^k_{[n]}$ *is stable for* $\cos(2\pi k/n)\beta < 0$.

PROOF. Reformulating the potential in Theorem 19 with $x = \sqrt{\eta}w$ where $\eta \geq 0$ and $\|w\|_2 = 1$ then

$$V = -\eta + \frac{1}{2}\sum_{i=1}^{n}\left(w_i w_i^*\right)^2\eta^2 - \beta w^*\mathcal{L}w\eta, \tag{2.1.2}$$

and at equilibrium

$$\frac{\partial V}{\partial \eta} = -1 + \sum_{i=1}^{n}\left(w_i w_i^*\right)^2\eta - \beta w^*\mathcal{L}w = 0,$$

and so $\sum_{i=1}^{n}\left(w_i w_i^*\right)^2\eta = 1 + \beta w^*\mathcal{L}w$. Substituting back into the potential then $V = -\frac{1}{2}\eta\left(1 + \beta w^* Lw\right)$. Consider $w_i = |w_i|\, e^{j\theta_i}$ for all $i \in [n]$, at equilibrium

$$\frac{\partial V}{\partial \theta_i} = -\frac{1}{2}\eta\beta\left(jw_i\right)^*\mathcal{L}_i w = 0,$$

and for $\eta \neq 0$, $\mathcal{L}_i w = \alpha_i w_i$ for some $\alpha_i \in \mathbb{R}$.[2] This condition is identical to the Kuramoto dynamics critical condition, and for circulant matrices it is satisfied when w is a unit eigenvector of the graph Laplacian [**75**]. This corresponds to the $\mathcal{C}^k_{[n]}$ balanced states with $\theta_{i+1} - \theta_i = 2\pi k/n$ for all and $k \in [n]$. For the case where $\sin(2\pi k/n) = 0$, the phase dynamics are invariant under different amplitudes, with the only common amplitude value satisfying amplitude dynamics (2.0.5) when the oscillators are on the unit circle. Examining the phase dynamics (2.0.5) for $\sin(2\pi k/n) \neq 0$ with $a_i = a_{i+1} \pmod n$ and applying this condition to the amplitude dynamics (2.0.5) we have that $a_i^2 = 1 + \beta\lambda_k = 1 + 2\beta\left(1 - \cos 2\pi k/n\right)$ for all $i \in [n]$ and $k \in [n]$ for $|\beta| \leq \frac{1}{2}$. Examining the potential in Eq. (2.1.2), the balanced

[2]There exists an annulus, which contains the unit circle but not the origin, that represents an invariant set of the dynamics. Consequently, for dynamics starting close to the unit circle the amplitudes will not go to zero.

states represent either local minima or maxima corresponding to stable or unstable equilibria depending on the sign of β. A simple check for the appropriate sign of β can be found by examining the phase acceleration dynamics about the equilibrium $\theta_{i+1} - \theta_i = 2\pi k/n$, $a_i = a_{i+1}$, $\dot{\theta}_{i+1} = \dot{\theta}_{i-1} = 0$ and $\dot{a}_i = 0$ for $i \in [n]$, giving

$$\begin{aligned}
\ddot{\theta}_i &= \frac{\partial \dot{\theta}_i}{\partial \theta_i} \dot{\theta}_i \\
&= \beta \left(\frac{a_{i+1}}{a_i} \cos(\theta_i - \theta_{i+1}) + \frac{a_{i-1}}{a_i} \cos(\theta_i - \theta_{i-1}) \right) \dot{\theta}_i \\
&= 2\beta \left(\cos 2\pi k/n \right) \dot{\theta}_i + \text{h.o.t.},
\end{aligned}$$

and so $\beta \cos 2\pi k/n < 0$ for stable $\mathcal{C}^k_{[n]}$.

□

The equilibria patterns corresponding to Theorem 20 are displayed in Figure 2.1.1 for the 6-node cycle graph. The first and second row corresponds to those balanced states that are stable for $\beta < 0$ and $\beta > 0$, respectively. A unique feature of the graph Ginzburg-Landau dynamics, opposed to the Kuramoto dynamics, is the variation of amplitude at different $\mathcal{C}^k_{[n]}$. For balanced states with $\beta < 0$ the balanced states are on or within the unit circle, while for $\beta > 0$ the balanced states are outside the unit circle.

2.2. MDP Formulation for Pattern Control

The control of patterns in nonlinear systems is a challenging task, often requiring highly accurate modeling, monitoring and actuation. Feedback is the natural control candidate but can be infeasible in cases where minimal external inputs are required and uncertainty dominates [**32**]. Brief time perturbation approaches rely on the underlying dynamics to carry the system trajectories between equilibria. The difficulty here lies in capturing the basin structure of the dynamics, frequently demanding sampling or local linearization of the dynamics [**34**].

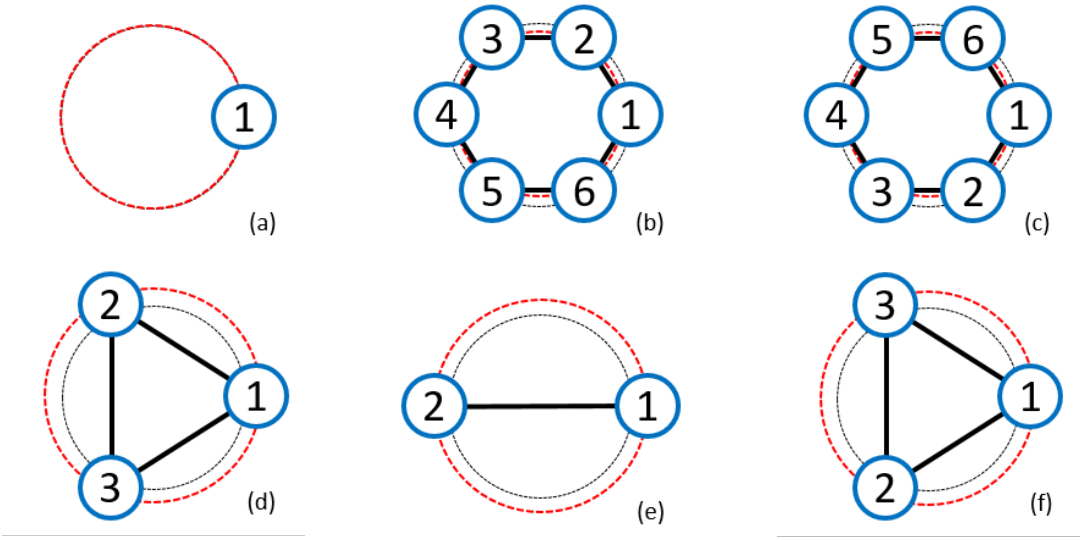

FIGURE 2.1.1. The $\mathcal{C}^k_{[6]}$ balanced states and pair $\{\mathbf{sgn}(\beta), \bar{a}\}$ for $k = 0, \ldots, n-1$ and $|\beta| = 0.1$, namely are A) $\mathcal{C}^0_{[6]}, \{-1, 1.00\}$, B) $\mathcal{C}^1_{[6]}, \{-1, 0.95\}$, C) $\mathcal{C}^5_{[6]}, \{-1, 0.95\}$, D) $\mathcal{C}^2_{[6]}, \{1, 1.14\}$, E) $\mathcal{C}^3_{[6]}, \{1, 1.18\}$, and F) $\mathcal{C}^4_{[6]}, \{1, 1.14\}$. The black and dashed circles indicate circles of radius one and $\bar{a}$, respectively. Solid lines between nodes indicate graph edges.

We approach the problem of pattern selection in the graph Ginzburg-Landau dynamics from a topological control direction. We consider rewiring the edges in the oscillator network using the patterns associated with the new graph to move the trajectory closer to the desired pattern. In this way, the dynamics are controlled by internal feedback dynamics induced by the addition of edges rather than the application of external signals. Further, the pattern selection task is transformed from a continuous time signal control problem to a discrete decision making problem. For noise-free systems, transitions between patterns on connected graphs, induced by edge rewiring, are completely deterministic. We consider a noisy version of the Ginzburg-Landau dynamics without the assumption that connectivity must be maintained through edge rewiring. The problem subsequently becomes a stochastic decision process making is particularly suited to an MDP formulation.

To leverage the analysis of patterns over cycle graphs, we consider only edge rewiring over disconnected subgraph cycles of the form $\mathcal{G} = \mathcal{C}_1(V_1, E_1) \cup \mathcal{C}_2(V_2, E_2) \cup \cdots \cup \mathcal{C}_m(V_m, E_m)$. The full set of vertices is the disjoint union of vertices $V_1, \ldots, V_m$ with size $|V_i| \geq 1$, as

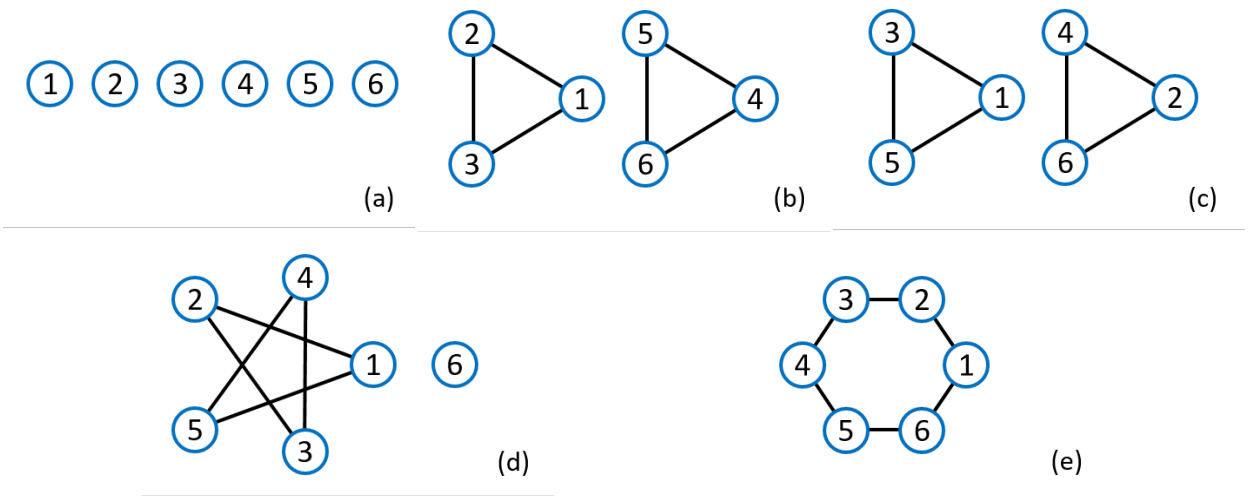

FIGURE 2.2.1. A) State 1 ($\prod_{i=1}^{6} \mathcal{C}_i^0$), B) state 3 ($\mathcal{C}_{1,2,3}^1 \mathcal{C}_{4,5,6}^1$), C) state 8 ($\mathcal{C}_{1,3,5}^1 \mathcal{C}_{2,4,6}^1$), D) state 14 ($\mathcal{C}_{[5]}^2, \mathcal{C}_6^0$), and E) state 18 ($\mathcal{C}_{[6]}^1$).

we consider the singleton graph as a cycle. We extend the balanced equilibrium notation of §2.1 to describe patterns over disconnected cycle subgraphs, denoting $\mathcal{C}_{V_1}^{k_1} \mathcal{C}_{V_2}^{k_2} \dots \mathcal{C}_{V_m}^{k_m}$ as the pattern state whereby each cycle $\mathcal{C}_i$ is in pattern state k_i. For compactness we also define $\prod_{i=1}^{m} \mathcal{C}_{V_i}^{k_i} = \mathcal{C}_{V_1}^{k_1} \dots \mathcal{C}_{V_m}^{k_m}$. A sample of patterned cycle subgraph on 6-nodes with the corresponding notation is depicted in Figure 2.2.1. Each of the patterned cycles will form the states $\mathcal{S}$ of the MDP. In addition to selecting the cycle subgraphs, we assume that we can also assign the sign of β globally to the graph. This generates an action space $\mathcal{A}$ for the MDP composed of graph-beta sign pairs $(\mathcal{G}_i, \mathbf{sgn}(\beta))$. These actions will transition the dynamics between states $\mathcal{S}$.

Noise in the system is induced by small biases in the rotation rate ω in Eq. (2.0.6) across oscillators. These biases are typical in oscillator systems and have been extensively explored for the Kuramoto dynamics [**28**]. For small biases over connected graphs the coupling between oscillators dominates the dynamics leaving the pattern largely unvaried. On the other hand, the relative phase offset between disconnected subgraphs is dominated by this bias, inducing relative phase mixing between graph clusters. This induces sufficient mixing necessary for the system to be Markovian with respect to phase offsets. The probability of actions then takes the memoryless form $\mathcal{T}(s, s', a)$ from Eq. (2.0.7). To calculate $\mathcal{T}(s, s', a)$,

we run Monte-Carlo simulations, sampling the transition probabilities over random initial phase biases between subsets. Unlike traditional basin of attraction sampling, this is considerably cheaper computationally as the dimension of the simulation grows with the number of subgraph patterns and the number of edge rewiring actions, rather than with the dimension of the system.

Finally, the reward states $\mathcal{R}(s', a)$ encode the desired final pattern. Alternative reward structures can also be implemented for example adding rewards for transitioning to other favorable states or penalties for adding many edges at once or switching the sign of β. Using the typical expected discounted sum reward over an infinite horizon from Eq. (2.0.8), an optimal policy $\pi(s)$ for action $s \in \mathcal{S}$ can be formulated used linear or dynamic programming [**74**].

2.3. Results for Ginzburg-Landau Dynamics

The topological rewiring approach for pattern control described in §2.2 was applied to five different cycle subgraphs on 6 nodes running the graph Ginzburg-Landau dynamics. These subgraphs, including 1, 3, 5 and 6 subgraph cycle with sample balanced patterns, are displayed in Figures 2.2.1A-E with topology labeled as $\mathcal{G}_1, \ldots, \mathcal{G}_5$, respectively. We note that Figures 2.2.1B and 2.2.1C are distinct pairs of three node subgraphs as the cycles are over different vertex sets. Enumerating over all patterns in the five graphs, with $n_{\beta+}^{\mathcal{G}_i}$ and $n_{\beta-}^{\mathcal{G}_i}$ the number of available pattern states for each subgraph $\mathcal{G}_i$, the total number of graphs for $\beta > 0$ and $\beta < 0$, respectively, is $n_{\beta+} = \sum_{i=1}^{5} n_{\beta+}^{\mathcal{G}_i} = 1 + 1 + 1 + 3 + 3 = 9$ and $n_{\beta-} = \sum_{i=1}^{5} n_{\beta-}^{\mathcal{G}_i} = 0 + 4 + 4 + 2 + 3 = 13$.

We assume that the pattern $\prod_{i=1}^{6} \mathcal{C}_i^0$ in Figure 2.2.1A is acquired under the action of $\beta > 0$ only. We add an additional state 23 which corresponds to an unknown state which is a product of unclassified states during the transition sampling. The only action available from this state is to transition to the 6 node singleton graph $\prod_{i=1}^{6} \mathcal{C}_i^0$. Hence there are $|\mathcal{S}| = n_{\beta+} + n_{\beta-} + 1 = 23$ states and $|\mathcal{A}| = 9$ actions in the MDP.

A sample transition probability matrix $\mathcal{T}(s, s', a)$ for fixed action 7, corresponding to the action pair $(\mathcal{G}_4, \mathbf{sgn}(\beta) = -1)$ is displayed in Figure 2.3.1a. The two final states s' available are $\mathcal{C}^2_{[5]}\mathcal{C}^0_6$ and $\mathcal{C}^3_{[5]}\mathcal{C}^0_6$, respectively. Figure 2.3.1b gives an indication of the reachability of certain states encoding the transition probabilities of final states from a given initial state and a random action. State 13, corresponding to $\mathcal{C}^1_{[5]}\mathcal{C}^0_6$, is particularly hard to obtain.

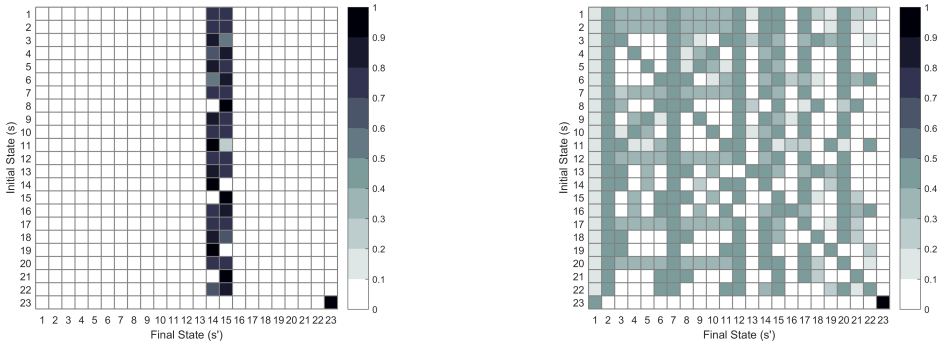

(A) (B)

FIGURE 2.3.1. MDP transition probabilities obtained from Monte-Carlo simulations of the dynamics. A) Transition probabilities for action 7 and B) average transition probability across all actions, assuming actions are chosen at random.

A desired state 21, representing $\mathcal{C}^4_{[6]}$, was selected corresponding to a reward set $\mathcal{R}(s' = 21, a) = 1$ for all $a \in \mathcal{A}$. For the cost function in Eq. (2.0.8) with $\gamma = 0.95$, using dynamic programming, the optimal policy π^* was formulated, with a corresponding optimal transition probability $\mathcal{T}_{\pi^*}(s, s')$. This transition probability is graphically depicted in Figure 2.3.2a with selected optimal actions displayed on the graph edges and edge thickness corresponding to the probability of transition under the action. One of the implicit strengths of this approach is that it exploits smaller subgraphs with larger basins to achieve larger graph patterns. This is particularly pertinent when examining the optimal routing of patterns through state 8, corresponding to $\mathcal{C}^1_{1,3,5}\mathcal{C}^2_{2,4,6}$, in preference to directly transitioning to state 21. This is supported by examining columns 8 and 21 of Figure 2.3.1b, indicating the relative challenge to directly acquiring state 21 over state 8 and then 21. The topological rewiring realization of policy π^* over a sample trajectory, initialized from the unknown random state, is displayed in Figure 2.3.2b. We observe that after 6 topological rewirings we attained the desired pattern.

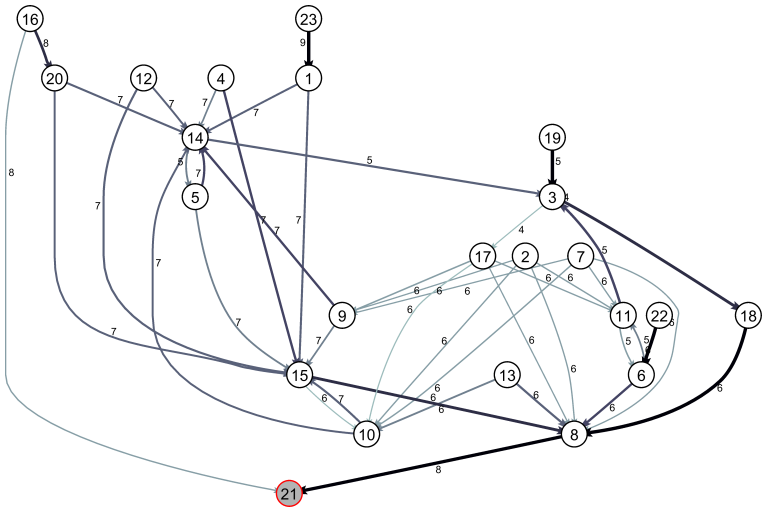

(A)

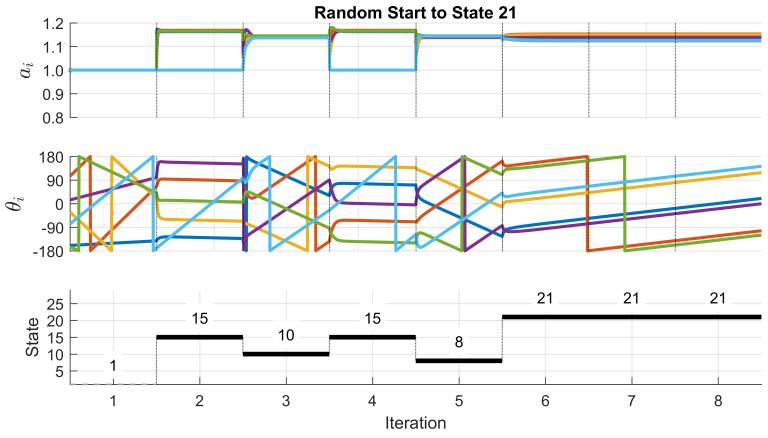

(B)

FIGURE 2.3.2. Given the Ginzburg-Landau dynamics, optimal policy for reaching state 21 from any initial state. A) Transition graph (low probability edges are omitted for clarity) and B) topological switching controller implemented using the optimal policy.

2.4. Concluding Remarks

This chapter proposed a design methodology for pattern control in a network of identical oscillators. Patterns correspond to a stable equilibrium in an oscillator network over different coupling coefficients and available network topologies. We showed that the discrete graph based version of the Ginzburg-Landau equation exhibits n pattern equilibrium for an n-node cycle graph with the sign of the oscillator coupling coefficient dictating the stability of the pattern. The pattern control problem was cast as an MDP whose state space is the set of

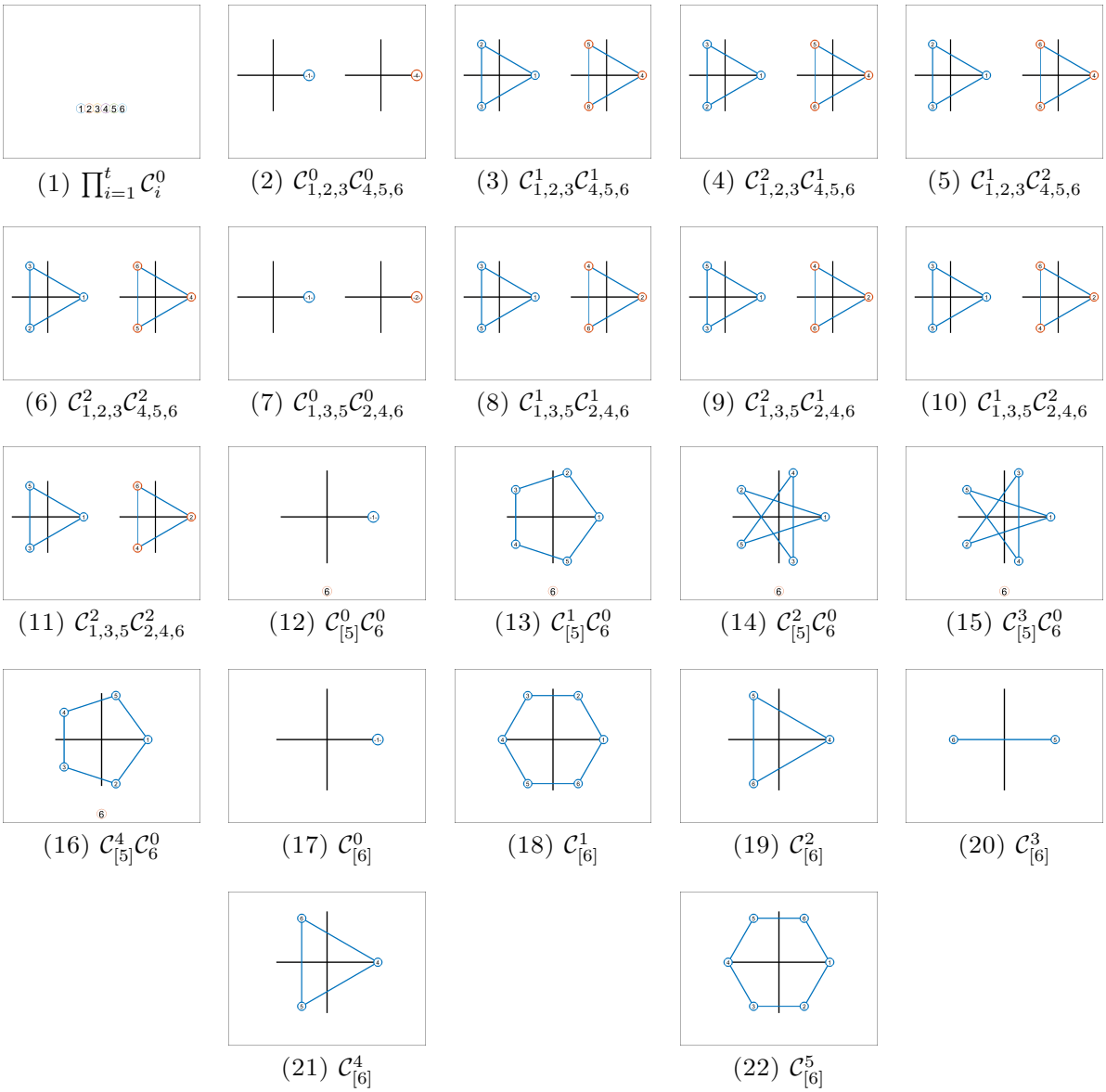

(1) $\prod_{i=1}^{t} \mathcal{C}_i^0$ (2) $\mathcal{C}_{1,2,3}^0 \mathcal{C}_{4,5,6}^0$ (3) $\mathcal{C}_{1,2,3}^1 \mathcal{C}_{4,5,6}^1$ (4) $\mathcal{C}_{1,2,3}^2 \mathcal{C}_{4,5,6}^1$ (5) $\mathcal{C}_{1,2,3}^1 \mathcal{C}_{4,5,6}^2$

(6) $\mathcal{C}_{1,2,3}^2 \mathcal{C}_{4,5,6}^2$ (7) $\mathcal{C}_{1,3,5}^0 \mathcal{C}_{2,4,6}^0$ (8) $\mathcal{C}_{1,3,5}^1 \mathcal{C}_{2,4,6}^1$ (9) $\mathcal{C}_{1,3,5}^2 \mathcal{C}_{2,4,6}^1$ (10) $\mathcal{C}_{1,3,5}^1 \mathcal{C}_{2,4,6}^2$

(11) $\mathcal{C}_{1,3,5}^2 \mathcal{C}_{2,4,6}^2$ (12) $\mathcal{C}_{[5]}^0 \mathcal{C}_6^0$ (13) $\mathcal{C}_{[5]}^1 \mathcal{C}_6^0$ (14) $\mathcal{C}_{[5]}^2 \mathcal{C}_6^0$ (15) $\mathcal{C}_{[5]}^3 \mathcal{C}_6^0$

(16) $\mathcal{C}_{[5]}^4 \mathcal{C}_6^0$ (17) $\mathcal{C}_{[6]}^0$ (18) $\mathcal{C}_{[6]}^1$ (19) $\mathcal{C}_{[6]}^2$ (20) $\mathcal{C}_{[6]}^3$

(21) $\mathcal{C}_{[6]}^4$ (22) $\mathcal{C}_{[6]}^5$

FIGURE 2.3.3

patterns realizable on subgraphs of the network. Actions in the MDP corresponded to the selection of coupling coefficients and edge connections in the network. A novel transition sampling was applied to generate the necessary MDP transition probabilities. Dynamic programming was then used to calculate a 'coarse pattern control' stochastic policy that maximized the expected total reward over an infinite horizon.

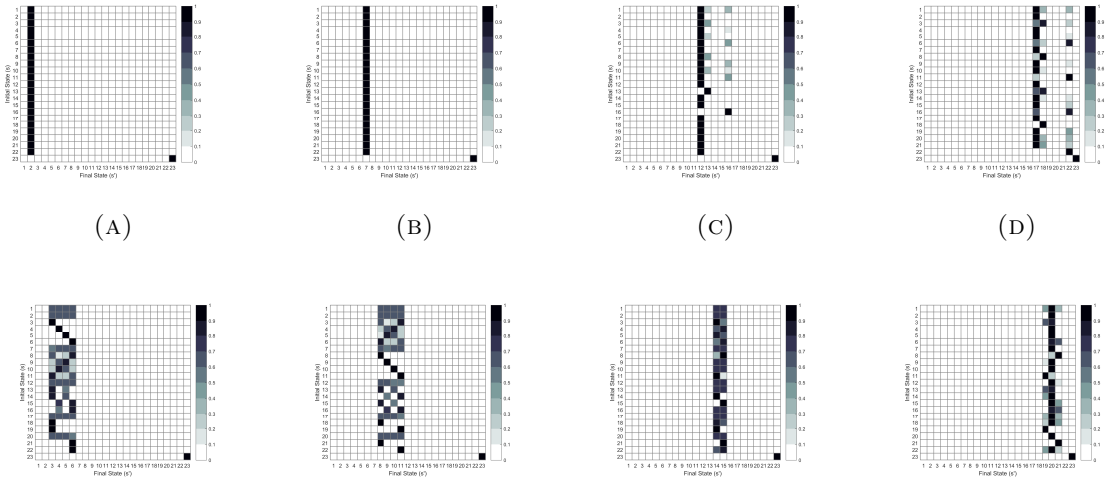

(A) (B) (C) (D)

(E) (F) (G) (H)

FIGURE 2.3.4. Transition probabilities for the Ginzburg-Landau dynamics.

Part 2

Bearing Measurements and Intuitive Manipulation

In this part, we present and examine a distributed formation control dynamics that uses relative bearing measurements and a compass to localize these measurements. The dynamics, referred to as bearing-compass dynamics, is introduced in Chapter 3 as well an exploration of the properties of the passive dynamics. In Chapter 4, we examine the effect on the formation when a subset of the agents is actively manipulated. We extend these manipulation concepts further in Chapter 5 by investigating methods to select a favorable set of leader agents to allow manipulating the formation in some desired ways, such as scaling, translation, and maximizing information propagation.

CHAPTER 3

Analysis of the Bearing-Compass Dynamics

In this chapter, we will present a dynamics, called Bearing-Compass dynamics, capable of being implemented with inexpensive hardware on a distributed robotic platform. Specifically, all that an agent needs is a sensor to measure the bearing to other agents, such as a monocular camera, and a compass with which to orient these measurements in a global frame. We begin by formally introducing some constructs that will be used throughout this part.

3.1. Bearing Measurements on a Graph

We use the term *node* to describe a particular element of V. There is also a more loosely termed *agent* which refers to something, usually a vehicle, that can communicate or act through the edges of E, and can have its own state. We define the agent positions in 2-D space at time t by the vector $\mathbf{r}(t) = [\ \mathbf{r}_1^T(t) \quad \mathbf{r}_2^T(t) \quad \dots \quad \mathbf{r}_n^T(t)\ ]^T$, where $\mathbf{r}_i(t) = [\ r_{ix}(t) \quad r_{iy}(t)\ ]^T$. Core to this research, is understanding agents formation shape when a family of bearing constraints are placed on pairs of agents. To this end, we use the term *formation*, denoted with $\mathbf{f} \in \mathbb{R}^{2n}$, to represent a desired state for a collection of agents. Franchi and Giordano [**38**] explored the notion of coupling of a formation with a graph, using the pairwise bearing measurement set

$$\Theta(\mathcal{G}, \mathbf{f}) \triangleq \left\{ \hat{\mathbf{f}}_{ij} \ : \ \{i,j\} \in E \right\}. \tag{3.1.1}$$

We will take an excursion from Franchi and Giordano terminology and refer to this as a *framework*. The collection of agent formations $\mathbf{r}$ which are *bearing equivalent*, or just

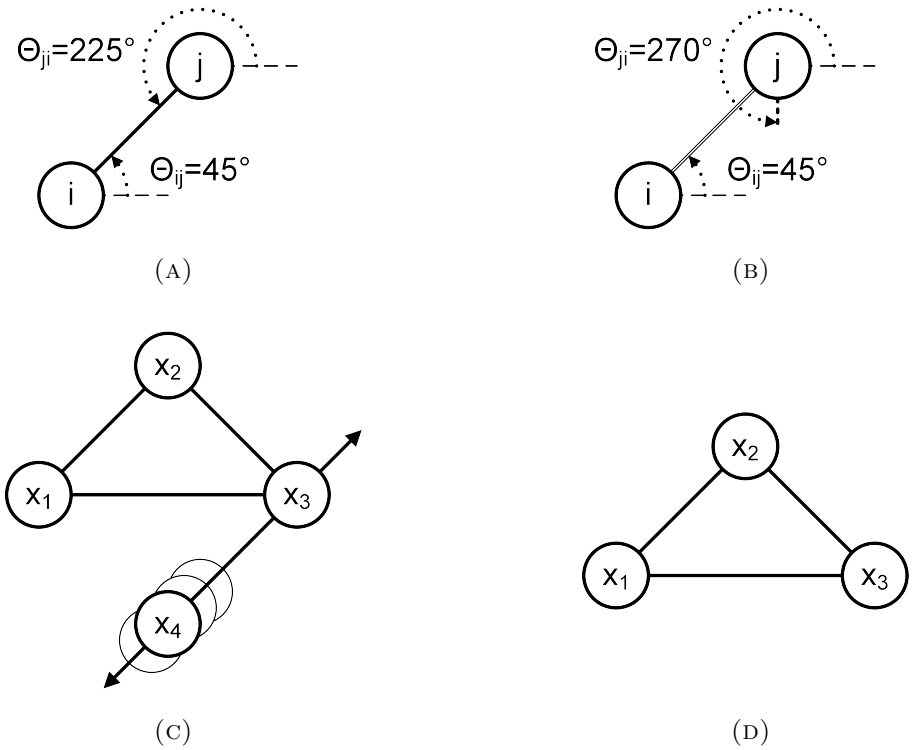

FIGURE 3.1.1. Bearing constraints which are A) desired (and realizable) and B) non-realizable. Formations which correspond to C) a realizable bearing, but not a parallel rigid, set and D) a parallel rigid set.

equivalent, to a given framework Θ is denoted by

$$\chi(\Theta) = \left\{ \mathbf{r} \,:\, \hat{\mathbf{r}}_{ij}^T \hat{\mathbf{f}}_{ij}^{\perp} = 0,\, \forall \hat{\mathbf{f}}_{ij} \in \Theta \right\}. \tag{3.1.2}$$

If $\chi(\Theta)$ is non-empty then Θ is referred to as a *realizable bearing* set [**37**]. Examples of a realizable and non-realizable bearing set can be seen in Figures 3.1.1a and 3.1.1b. Further, if every pair of position vectors in a realizable bearing set $\chi(\Theta)$ is equivalent to every other up to 2-D scaling and translation then Θ is called a *parallel rigid* set [**37**]. Figures 3.1.1c and 3.1.1d provide examples of non-parallel-rigid and parallel-rigid sets. A linear algebra test for parallel rigidity using the rank of the bearing-constrained rigidity matrix, as well as a graph theoretic test, has been formulated by Bishop *et al.* [**37**]. Additional algebraic conditions that guarantee bearing rigidity based on the notion of infinitesimal bearing rigidity will be explored in Chapter 8. Henceforth, we shall consider only parallel rigid sets Θ.

In order to more easily classify similar formations, we introduce the notion of centroid and scale of a formation [**42, 39**]. Given a set of agents at positions $\mathbf{r} \in \mathbb{R}^{2n}$, the *centroid* of the agent formation is defined as

$$C(\mathbf{r}) \triangleq \frac{1}{n} \sum_{i \in V} \mathbf{r}_i. \tag{3.1.3}$$

The scale of the agent formation is defined as

$$S(\mathbf{r}) \triangleq \sqrt{\frac{1}{n} \sum_{i \in V} \|\mathbf{q}_i\|^2}, \tag{3.1.4}$$

where

$$\mathbf{q}_i \triangleq \mathbf{r}_i - C(\mathbf{r}) \tag{3.1.5}$$

represents the relative offset from an agent from the formation centroid.

Given a formation $\mathbf{f} \in \mathbb{R}^{2n}$, the *unitless formation* $\tilde{\mathbf{f}}$ is defined as

$$\tilde{\mathbf{f}} = [\mathbf{f} - (I_n \otimes C(\mathbf{f}))\, \mathbf{1}_n]\, S(\mathbf{f})^{-1}, \tag{3.1.6}$$

with properties $C(\tilde{\mathbf{f}}) = \mathbf{0}$, $S(\tilde{\mathbf{f}}) = 1$, and $\left\|\tilde{\mathbf{f}}\right\| = \sqrt{n}$.

Given a set of agent positions $\mathbf{r} \in \mathbb{R}^{2n}$ and a desired formation $\mathbf{f} \in \mathbb{R}^{2n}$, we define the two *most similar* formations $\xi_\pm(\mathbf{f}, \mathbf{r}) = \{\xi_+(\mathbf{f}, \mathbf{r}), \xi_-(\mathbf{f}, \mathbf{r})\}$ to the given formation $\mathbf{f}$. Broadly speaking, ξ represents the formations that have the same "shape" as $\mathbf{f}$, but the same centroid and scale as $\mathbf{r}$. In this way, the definitions are prescriptive as

$$\begin{aligned} \xi_\pm(\mathbf{f}, \mathbf{r}) &= \{\mathbf{f} \in \chi(\Theta) : C(\mathbf{f}) = C(\mathbf{r}) \cap S(\mathbf{f}) = S(\mathbf{r})\} \\ &= \pm \tilde{\mathbf{f}} S(\mathbf{r}) + (I_n \otimes C(\mathbf{r}))\, \mathbf{1}. \end{aligned}$$

It is not immediately obvious that the set $\xi_\pm(\mathbf{f}, \mathbf{r})$ should contain exactly two elements. The reasons for this property will be explored in Theorem 27.

In order to examine the dynamics (3.2.1) it is helpful to have machinery to encode the bearing information embedded within the dynamics. The bearing rigidity matrix serves this function and can be constructed from the framework Θ composed of the formation $\mathbf{f}$ and the underlying graph $\mathcal{G}$.

DEFINITION 21. The *bearing rigidity matrix* is denoted $\mathcal{R}(\Theta)$, where $\Theta(\mathcal{G}, \mathbf{f})$ is a framework, is defined as

$$\mathcal{R}(\Theta) \triangleq \frac{\partial \hat{\bar{\mathbf{f}}}}{\partial \mathbf{f}}, \tag{3.1.7}$$

where $\bar{\mathbf{f}} = \widetilde{H}\mathbf{f}$ is the vector of relative node states from §0.2, and $\hat{\bar{\mathbf{f}}} \triangleq \begin{bmatrix} \hat{\mathbf{f}}_{(\bar{1})}^T & \hat{\mathbf{f}}_{(\bar{2})}^T & \dots & \hat{\mathbf{f}}_{(\bar{m})}^T \end{bmatrix}^T$. An alternative expression for Eq. (3.1.7) is[1]

$$\begin{aligned} \mathcal{R}(\Theta) &= \mathcal{D}_{\bar{k}} \left[\frac{1}{\|\mathbf{f}_{\bar{k}}\|} I_2 \right] \mathcal{D}_{\bar{k}} \left[P_{\bar{k}} \right] \widetilde{H} \\ &= \mathcal{D}_{\bar{k}} \left[\frac{1}{\|\mathbf{f}_{\bar{k}}\|} I_2 \right] \widetilde{\mathcal{R}}(\Theta), \end{aligned}$$

where $P_{\bar{k}} = I_2 - \hat{\mathbf{f}}_{\bar{k}} \hat{\mathbf{f}}_{\bar{k}}^T$ is a projection onto the orthogonal compliment of $\mathbf{f}_{\bar{k}}$, and $\widetilde{\mathcal{R}}(\Theta)$ is called the *unit rigidity matrix*. The derivation of this formulation can be found in A.

The rigidity matrix exhibits the property that $\mathbf{r} \in \chi(\Theta)$ if and only if $\mathcal{R}(\Theta)\mathbf{r} = \mathbf{0}$, or equivalently $\widetilde{\mathcal{R}}(\Theta)\mathbf{r} == \mathbf{0}$.

We can interpret the bearing rigidity matrix as the derivative of the relative edge directions with respect to node positions. In other words, we are measuring how the relative directions between nodes changes with node positions.

3.2. Statement of Dynamics

The dynamics discussed in this research can be stated succinctly as

$$\dot{\mathbf{r}}_i = \mathbf{u}_i(\Theta) + \tilde{\mathbf{u}}_i \tag{3.2.1a}$$

[1]It is assumed throughout that no two agents are coincident within a formation, and so $\|\mathbf{f}_{\bar{k}}\| \neq 0$.

$$\mathbf{u}_i(\Theta) = \sum_{j\in\mathcal{N}(i)} w_{ij}\left(\hat{\mathbf{r}}_{ij}^T\hat{\mathbf{f}}_{ij}^{\perp}\right)\hat{\mathbf{r}}_{ij}^{\perp}, \tag{3.2.1b}$$

where $\Theta = (\mathcal{G}, \mathbf{f})$, and $\mathcal{G} = (V, E, \mathbf{w})$. If $\tilde{\mathbf{u}}_i = 0$ for all $i \in V$, then we say the dynamics is *unforced*. Otherwise, we say the dynamics is *forced*. Similarly, if $\mathbf{w} = \mathbf{1}$, then we say the dynamics is *weighted*. Otherwise, we say the dynamics is *unweighted*, or omit the modifier entirely. Agents i corresponding to $\tilde{\mathbf{u}}_i \neq 0$ are referred to as *leaders*, as through the networked dynamics, the non-leader agents follow the leaders.

We note that the unforced control required by each agent is bounded, summarized in the following proposition.

PROPOSITION 22. *The unforced control $\|\mathbf{u}_i\|$ required by each agent $i \in V$ is bounded as*

$$\|\mathbf{u}_i\| \leq \sum_{j\in\mathcal{N}(i)} w_{ij},$$

which, for $\mathbf{w} = \mathbf{1}$, degenerates to

$$\|\mathbf{u}_i\| \leq |\mathcal{N}(i)|.$$

PROOF. The proof follows directly by observing the $\hat{\mathbf{r}}_{ij}^T\hat{\mathbf{f}}_{ij}^{\perp}$ term from Eq. (3.2.1b) is bounded in magnitude by 1. □

The preceding proposition is useful because it means our individual agent control is always bounded, and so we can bound the maximum control effort needed by a single agent by limiting the number of other agents it can observe, or by reducing the weights of the adjacent edges.

The dynamics 3.2.1 is referred to as a *particle model*, as the dynamics assume that the state $\mathbf{r}$ can move in an arbitrary direction, and its velocity can change instantaneously. Typically, a particle model does not accurately describe the motion of most physical vehicles. For example, cars and airplanes cannot move sideways, and more complicated trajectories are needed to change their state in this way. However, it is still often useful to study these particle models, as a tracking controller can be designed to follow this so-called *virtual particle* [**76**].

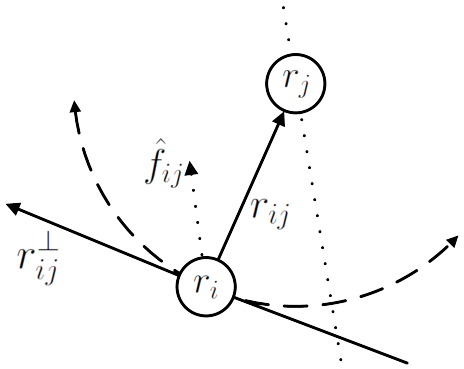

FIGURE 3.2.1. Vector definitions for dynamics (3.2.1).

As we proceed through this section, we will examine various features of the bearing-compass dynamics.To this end, the following proposition is a useful tool which will be used throughout this paper to simplify our proofs.

PROPOSITION 23. *Enumeration over nodes and neighborhoods is equivalent to enumeration over edges as*

$$\sum_{i\in V}\mathbf{a}_i^T\sum_{j\in\mathcal{N}(i)}\mathbf{b}_{(ij)}=-\sum_{\bar{k}\in E}\mathbf{a}_{\bar{k}}^T\mathbf{b}_{(\bar{k})}. \tag{3.2.2}$$

Equivalently, we can state the proposition as

$$\sum_{i\in V}\sum_{j\in\mathcal{N}(i)}\mathbf{b}_{(ij)}=\sum_{\{i,j\}\in E}\mathbf{b}_{(ij)}+\mathbf{b}_{(ji)}=\mathbf{0}.$$

PROOF. Note that the left hand side of Eq. (3.2.2) represents an enumeration of every edge twice, once representing $\mathbf{a}_i^T\mathbf{b}_{(ij)}$ and once representing $\mathbf{a}_j^T\mathbf{b}_{(ji)}$. Using the fact that $\mathbf{b}_{(ij)}=-\mathbf{b}_{(ji)}$, the result follows. □

The unforced weighted bearing-compass dynamics exhibits properties such as invariance of the formation centroid and scale, which make it attractive for maintaining stable formations. The forced dynamics is then able to directly manipulate the centroid and scale. The following propositions formerly explore this idea.

PROPOSITION 24. *Under the weighted dynamics (3.2.1), the formation centroid evolves as*

$$\frac{\partial C(\mathbf{r})}{\partial t} = \frac{1}{n}\sum_{i\in V}\tilde{\mathbf{u}}_i. \tag{3.2.3}$$

Additionally, if $\tilde{\mathbf{u}}_i = \mathbf{0}$ *for all* $i \in V$*, then* $\partial C(\mathbf{r})/\partial t = \mathbf{0}$ *and the centroid is said to be invariant under the unforced dynamics.*

PROOF. Differentiating Eq. (3.1.3) and substituting in Eq. (3.2.1a), we have

$$\begin{aligned}
\frac{\partial C(\mathbf{r})}{\partial t} &= \frac{1}{n}\sum_{i\in V}\dot{\mathbf{r}} \\
&= \frac{1}{n}\sum_{i\in V}(\mathbf{u}_i + \tilde{\mathbf{u}}_i) \\
&= \frac{1}{n}\sum_{i\in V}\sum_{j\in\mathcal{N}(i)}\mathbf{u}_{(ij)} + \frac{1}{n}\sum_{i\in V}\tilde{\mathbf{u}}_i \\
&= \frac{1}{n}\sum_{\{i,j\}\in E}\left(\mathbf{u}_{(ij)} + \mathbf{u}_{(ji)}\right) + \frac{1}{n}\sum_{i\in V}\tilde{\mathbf{u}}_i \\
&= \frac{1}{n}\sum_{i\in V}\tilde{\mathbf{u}}_i,
\end{aligned}$$

completing the proof. □

PROPOSITION 25. *Under the weighted dynamics (3.2.1), the formation scale evolves as*

$$\frac{\partial S(\mathbf{r})}{\partial t} = \frac{2}{nS(\mathbf{r})}\sum_{i\in V}\mathbf{q}_i^T\left(\tilde{\mathbf{u}}_i - \frac{1}{n}\sum_{j\in V}\tilde{\mathbf{u}}_j\right). \tag{3.2.4}$$

Additionally, if $\tilde{\mathbf{u}}_i = \mathbf{0}$ *for all* $i \in V$*, then*

$$\frac{\partial C(\mathbf{r})}{\partial t} = \mathbf{0},$$

and the scale is said to be invariant under the unforced dynamics.

PROOF. Differentiating Eq. (3.1.4), we have

$$\frac{\partial S(\mathbf{r})}{\partial t} = \frac{\partial}{\partial t}\sqrt{\frac{1}{n}\sum_{i\in V}\mathbf{q}_i^T\mathbf{q}_i}$$

$$
\begin{aligned}
&= \frac{1}{\sqrt{n\sum_{i\in V}\mathbf{q}_i^T\mathbf{q}_i}}\frac{\partial}{\partial t}\sum_{i\in V}\mathbf{q}_i^T\mathbf{q}_i \\
&= \frac{2}{nS\left(\mathbf{r}\right)}\sum_{i\in V}\mathbf{q}_i^T\dot{\mathbf{q}}_i \\
&= \frac{2}{nS\left(\mathbf{r}\right)}\sum_{i\in V}\mathbf{q}_i^T\left(\dot{\mathbf{r}}_i - \frac{\partial C\left(\mathbf{r}\right)}{\partial t}\right) \\
&= \frac{2}{nS\left(\mathbf{r}\right)}\sum_{i\in V}\mathbf{q}_i^T\left(\tilde{\mathbf{u}}_i - \frac{1}{n}\sum_{j\in V}\tilde{\mathbf{u}}_j\right),
\end{aligned}
$$

completing the proof. □

A consequence of these results is that if a single agent, say agent i, applies a non-zero external control input, then the centroid will always shift in the direction of the applied control, namely

$$\frac{\partial C(\mathbf{r})}{\partial t} = \frac{1}{n}\tilde{\mathbf{u}}_i,$$

and so

$$C(\mathbf{r}) = \frac{1}{n}\int_0^t \tilde{\mathbf{u}}_i + C(\mathbf{r}\left(0\right)).$$

Further, as

$$\frac{\partial S\left(\mathbf{r}\right)}{\partial t} = 2\left(\mathbf{r}_i - C(\mathbf{r})\right)^T\tilde{\mathbf{u}}_i,$$

changes in the centroid are coupled to changes in scale. In fact, movement away from the centroid will expand the formation, while movement towards will contract it. Figure 3.2.2a provides an example of a constant control applied to a single agent demonstrating the translation and scale of the formation.

COROLLARY 26. *Under the unforced weighted dynamics (3.2.1a), the centroid and scale of the formation are both constant, i.e.* $\dot{C}\left(\mathbf{r}\right) = \mathbf{0}$ *and* $\dot{S}\left(\mathbf{r}\right) = 0$.

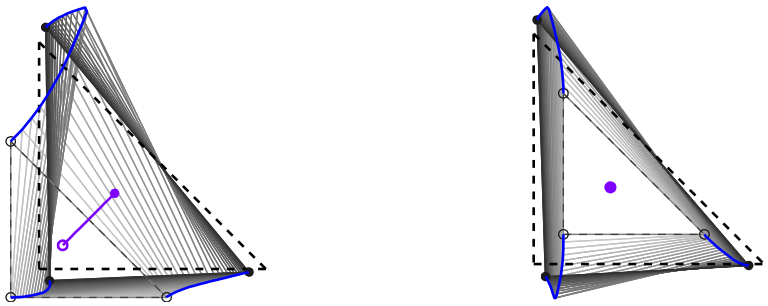

(A) (B)

FIGURE 3.2.2. A) Control applied to top agent, resulting in a scale and a translation. B) Top and bottom-left agents apply a control to move away from one another, resulting in a pure scale amplification while maintaining the centroid.

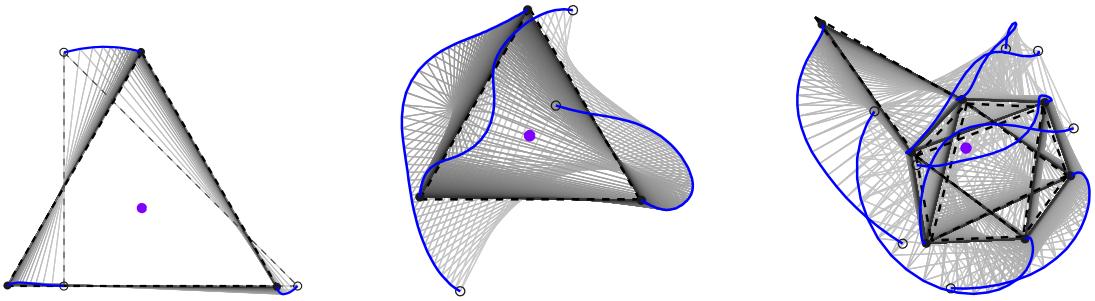

(A) (B) (C)

FIGURE 3.2.3. Convergence to an equilateral triangle from A) a right triangle and B) random initial conditions. Fig. C) shows random initial positions for 7 agents converging to an asymmetric formation. Initial and final positions are marked with open and closed circles, respectively, and the centroid by a larger solid circle. The most similar formation $\xi(\mathbf{f}, \mathbf{r}_0)$ to the desired final formation $\mathbf{f}$ given initial conditions $\mathbf{r}_0$ is marked with dashed lines.

PROOF. Both results follows directly from Propositions 24 and 25 when $\tilde{\mathbf{u}}_i = 0$ for all $i \in V$. □

The examples in Figure 3.2.3 show the conservation of $C(r)$ and $S(r)$ for varying bearing constraint sets Θ and initial conditions.

THEOREM 27. *Under the unforced weighted dynamics (3.2.1),* $\mathbf{r}(t)$ *will asymptotically converge to* $\chi(\Theta)$.

PROOF. Without loss of generality, assume that the centroid $C(\mathbf{r})$ is at the origin, meaning $\mathbf{q}_i = \mathbf{r}_i$. Let $\mathbf{f} = \xi_+(\mathbf{r}(0), \Theta)$. Consequently, $\|\mathbf{r}(0)\| = \|\mathbf{f}\|$ and $C(\mathbf{f}) = \mathbf{0}$. Applying the change of variables $\mathbf{z} = \mathbf{r} - \mathbf{f}$, where $\mathbf{r}_{ij} = \mathbf{z}_{ij} + \mathbf{f}_{ij}$, then for each $i \in V$ we have

$$\begin{aligned}
\dot{\mathbf{z}}_i &= \sum_{j \in \mathcal{N}(i)} w_{ij} \hat{\mathbf{r}}_{ij}^T \hat{\mathbf{f}}_{ij}^{\perp} \hat{\mathbf{r}}_{ij} \\
&= \sum_{j \in \mathcal{N}(i)} \frac{w_{ij}}{\|\mathbf{z}_{ij} + \mathbf{f}_{ij}\|^2} (\mathbf{z}_{ij} + \mathbf{f}_{ij})^T \hat{\mathbf{f}}_{ij}^{\perp} (\mathbf{z}_{ij} + \mathbf{f}_{ij})^{\perp} \\
&= \sum_{j \in \mathcal{N}(i)} \frac{w_{ij}}{\|\mathbf{z}_{ij} + \mathbf{f}_{ij}\|^2} \left(\mathbf{z}_{ij}^T \hat{\mathbf{f}}_{ij}^{\perp} + \cancelto{0}{\mathbf{f}_{ij}^T \hat{\mathbf{f}}_{ij}^{\perp}} \right) (\mathbf{z}_{ij} + \mathbf{f}_{ij})^{\perp} \\
&= \sum_{j \in \mathcal{N}(i)} \frac{w_{ij} \mathbf{z}_{ij}^T \hat{\mathbf{f}}_{ij}^{\perp}}{\|\mathbf{z}_{ij} + \mathbf{f}_{ij}\|^2} (\mathbf{z}_{ij} + \mathbf{f}_{ij})^{\perp} \\
&\triangleq \sum_{j \in \mathcal{N}(i)} \mathbf{g}_{(ij)}(\mathbf{z}, \mathbf{f}). \qquad (3.2.5)
\end{aligned}$$

Consider the Lyapunov function $V(\mathbf{z}) = \frac{1}{2}\mathbf{z}^T\mathbf{z}$. We can expand its time derivative using Eq. (3.2.5) and apply Proposition (3.2.2) as

$$\begin{aligned}
\dot{V}(\mathbf{z}) &= \sum_{i \in V} \mathbf{z}_i^T \dot{\mathbf{z}}_i \\
&= -\sum_{i \in V} \mathbf{z}_i^T \sum_{j \in \mathcal{N}(i)} \mathbf{g}_{(ij)}(\mathbf{z}, \mathbf{f}) \\
&= -\sum_{\bar{k} \in E} \frac{w_{\bar{k}} \mathbf{z}_{\bar{k}}^T \left(\mathbf{z}_{\bar{k}}^T \hat{\mathbf{f}}_{\bar{k}}^{\perp} \right)}{\|\mathbf{z}_{\bar{k}} + \mathbf{f}_{\bar{k}}\|^2} (\mathbf{z}_{\bar{k}} + \mathbf{f}_{\bar{k}})^{\perp} \\
&= -\sum_{\bar{k} \in E} \frac{w_{\bar{k}} \mathbf{z}_{\bar{k}}^T \hat{\mathbf{f}}_{\bar{k}}^{\perp}}{\|\mathbf{z}_{\bar{k}} + \mathbf{f}_{\bar{k}}\|^2} \left(\cancelto{0}{\mathbf{z}_{\bar{k}}^T \mathbf{z}_{\bar{k}}^{\perp}} + \mathbf{z}_{\bar{k}}^T \mathbf{f}_{\bar{k}}^{\perp} \right) \\
&= -\sum_{\bar{k} \in E} \frac{w_{\bar{k}} \left(\mathbf{z}_{\bar{k}}^T \mathbf{f}_{\bar{k}}^{\perp} \right)^2}{\|\mathbf{f}_{\bar{k}}\| \|\mathbf{z}_{\bar{k}} + \mathbf{f}_{\bar{k}}\|^2}. \qquad (3.2.6)
\end{aligned}$$

As $\dot{V}(\mathbf{z}) \leq 0$ and $\dot{V}(\mathbf{z}) = 0$ if and only if $\mathbf{z} \in \chi(\Theta)$, implying that $\mathbf{z}^T \hat{\mathbf{f}}^{\perp} = 0$, then it follows that $\mathbf{r} \in \chi(\Theta)$ and thus $\mathbf{r}(t)$ converges to $\chi(\Theta)$, establishing asymptotic stability by La Salle's theorem [**77**]. □

Asymptotic convergence to $\chi(\Theta)$ can be further strengthened to exponential stability. This is explored in the following theorem.

THEOREM 28. *Under the unforced weighted dynamics (3.2.1), the Lyapunov function* $V = \frac{1}{2}\mathbf{z}^T\mathbf{z}$ *where* $\mathbf{z} \triangleq \mathbf{r} - \mathbf{f}$ *satisfies*

$$\begin{aligned} \dot{V} &\leq S(\mathbf{f})^{-1}\mathbf{z}^T\widetilde{\mathcal{R}}^T\mathcal{D}_{\bar{k}}\left[m_{\bar{k}}^2 I_2\right]\widetilde{\mathcal{R}}\mathbf{z} \\ &\triangleq -S(\mathbf{f})^{-1}\mathbf{z}^T Q\mathbf{z}, \end{aligned}$$

where $\mathbf{f} = \xi(\mathbf{r}(0), \Theta)$, *and we define the term*

$$m_{\bar{k}}^2(r(0)) \triangleq \frac{w_{\bar{k}}\left\|\mathbf{f}_{\bar{k}}\right\|}{\left(S(\mathbf{f})^{-1}\left\|\mathbf{z}(0)\right\| + \left\|\tilde{\mathbf{f}}_{\bar{k}}\right\|\right)^2}.$$

Consequently, $\mathbf{r}(t)$ *will globally exponentially converge to* $\chi(\Theta)$.

PROOF. If we expand Eq. (3.2.6), we have

$$\begin{aligned} \dot{V}(\mathbf{z}) &= -\sum_{\bar{k}\in E}\frac{w_{\bar{k}}\left(\left(\mathbf{r}_{\bar{k}} - \mathbf{f}_{\bar{k}}\right)^T\mathbf{f}_{\bar{k}}^{\perp}\right)^2}{\left\|\mathbf{f}_{\bar{k}}\right\|\left\|\mathbf{r}_{\bar{k}} - \mathbf{f}_{\bar{k}} + \mathbf{f}_{\bar{k}}\right\|^2} \\ &= -\sum_{\bar{k}\in E}\frac{w_{\bar{k}}\left(\mathbf{r}_{\bar{k}}^T\mathbf{f}_{\bar{k}}^{\perp}\right)^2}{\left\|\mathbf{f}_{\bar{k}}\right\|\left\|\mathbf{r}_{\bar{k}}\right\|^2} \\ &= -\sum_{\bar{k}\in E}\frac{w_{\bar{k}}\left\|\mathbf{f}_{\bar{k}}\right\|}{\left\|\mathbf{r}_{\bar{k}}\right\|^2}\mathbf{r}_{\bar{k}}^T\left(\hat{\mathbf{f}}_{\bar{k}}^{\perp T}\mathbf{r}_{\bar{k}}\right)\hat{\mathbf{f}}_{\bar{k}}^{\perp}. \end{aligned}$$

We now apply the relationship that

$$\left(\hat{\mathbf{f}}_{\bar{k}}^{\perp T}\mathbf{r}_{\bar{k}}\right)\hat{\mathbf{f}}_{\bar{k}}^{\perp} = \mathrm{Proj}_{\hat{\mathbf{f}}_{\bar{k}}^{\perp}}\mathbf{r}_{\bar{k}} = \mathbf{r}_{\bar{k}} - \mathrm{Proj}_{\hat{\mathbf{f}}_{\bar{k}}}\mathbf{r}_{\bar{k}} = P_{\bar{k}}\mathbf{r}_{\bar{k}}$$

to see that

$$\begin{aligned} \dot{V}(\mathbf{z}) &= -\sum_{\bar{k}\in E}\mathbf{r}_{\bar{k}}^T w_{\bar{k}}\frac{\left\|\mathbf{f}_{\bar{k}}\right\|}{\left\|\mathbf{r}_{\bar{k}}\right\|^2}P_{\bar{k}}\mathbf{r}_{\bar{k}} \\ &= -\mathbf{r}^T\widetilde{H}^T\mathcal{D}_{\bar{k}}\left[w_{\bar{k}}\frac{\left\|\mathbf{f}_{\bar{k}}\right\|}{\left\|\mathbf{r}_{\bar{k}}\right\|^2}P_{\bar{k}}\right]\widetilde{H}\mathbf{r}. \end{aligned} \tag{3.2.7}$$

Now, we observe that

$$\mathcal{D}_{\bar{k}}\left[w_{\bar{k}}\frac{\|\mathbf{f}_{\bar{k}}\|}{\|\mathbf{r}_{\bar{k}}\|^2}P_{\bar{k}}\right]\widetilde{H}\mathbf{f}=\mathbf{0} \tag{3.2.8}$$

as $P_{\bar{k}}\mathbf{f}_{\bar{k}}=\mathbf{0}$ due to $P_{\bar{k}}$ being a projection onto the orthogonal compliment of $\mathbf{f}_{\bar{k}}$. Thus, we can add Eq. (3.2.8) into Eq. (3.2.7) as

$$\begin{aligned}\dot{V}(\mathbf{z}) &= -(\mathbf{r}-\mathbf{f})^T\widetilde{H}^T\mathcal{D}_{\bar{k}}\left[w_{\bar{k}}\frac{\|\mathbf{f}_{\bar{k}}\|}{\|\mathbf{r}_{\bar{k}}\|^2}P_{\bar{k}}\right]\widetilde{H}(\mathbf{r}-\mathbf{f})\\ &= -\mathbf{z}^T\widetilde{H}^T\mathcal{D}_{\bar{k}}\left[w_{\bar{k}}\frac{\|\mathbf{f}_{\bar{k}}\|}{\|\mathbf{r}_{\bar{k}}\|^2}P_{\bar{k}}\right]\widetilde{H}\mathbf{z}.\end{aligned}$$

Similarly, we can also introduce additional multiplicative $\mathcal{D}_{\bar{k}}[P_{\bar{k}}]$ terms, using the fact that $P_{\bar{k}}$ is a projection matrix, and so $P_{\bar{k}}^2=P_{\bar{k}}$. Thus,

$$\dot{V}(\mathbf{z})=-\mathbf{z}^T\widetilde{H}^T\mathcal{D}_{\bar{k}}[P_{\bar{k}}]^T\mathcal{D}_{\bar{k}}\left[w_{\bar{k}}\frac{\|\mathbf{f}_{\bar{k}}\|}{\|\mathbf{r}_{\bar{k}}\|^2}P_{\bar{k}}\right]\mathcal{D}_{\bar{k}}[P_{\bar{k}}]\widetilde{H}\mathbf{z}.$$

However, we notice that

$$\begin{aligned}\frac{\|\mathbf{f}_{\bar{k}}\|}{\|\mathbf{r}_{\bar{k}}\|^2} &= \frac{\|\mathbf{f}_{\bar{k}}\|}{\|\mathbf{z}_{\bar{k}}+\mathbf{f}_{\bar{k}}\|^2}\\ &\geq \frac{\|\mathbf{f}_{\bar{k}}\|}{[\|\mathbf{z}_{\bar{k}}\|+\|\mathbf{f}_{\bar{k}}\|]^2}.\end{aligned}$$

Applying Theorem 27, $\|\mathbf{z}_{\bar{k}}\|\leq\|\mathbf{z}\|\leq\|\mathbf{z}_0\|$. Thus, we can write

$$\begin{aligned}\frac{w_{\bar{k}}\|\mathbf{f}_{\bar{k}}\|}{\|\mathbf{r}_{\bar{k}}\|^2} &\geq \frac{w_{\bar{k}}S(\mathbf{f})\left\|\tilde{\mathbf{f}}_{\bar{k}}\right\|}{\left[\|\mathbf{z}_0\|+S(\mathbf{f})\left\|\tilde{\mathbf{f}}_{\bar{k}}\right\|\right]^2}\\ &= S(\mathbf{f})^{-1}\frac{w_{\bar{k}}\left\|\tilde{\mathbf{f}}_{\bar{k}}\right\|}{\left[S(\mathbf{f})^{-1}\|\mathbf{z}_0\|+\left\|\tilde{\mathbf{f}}_{\bar{k}}\right\|\right]^2}\\ &\triangleq S(\mathbf{f})^{-1}m_{\bar{k}}^2.\end{aligned}$$

From the definition of $m_{\bar{k}}^2$ and the unit bearing rigidity matrix $\widetilde{\mathcal{R}}$, we have

$$\dot{V}\leq -S(\mathbf{f})^{-1}\mathbf{z}^T\widetilde{\mathcal{R}}^T\mathcal{D}_{\bar{k}}\left[m_{\bar{k}}^2I_2\right]\widetilde{\mathcal{R}}\mathbf{z}.$$

The worst case initial error is $\|\mathbf{z}_0\| \leq \|-2\mathbf{f}\| = 2\sqrt{n}S(\mathbf{f})$, which follows from the fact that the trajectory of the error $\mathbf{z}$ under the dynamics 3.2.1 travels along a sphere of radius $\|\mathbf{f}\|$ [**42, 39**]. Noting that

$$m_{\bar{k}}^2 \geq \frac{w_{\bar{k}} \left\| \tilde{\mathbf{f}}_{\bar{k}} \right\|}{\left[2\sqrt{n} + \left\| \tilde{\mathbf{f}}_{\bar{k}} \right\| \right]^2}$$

and let

$$\beta = \min_{\bar{k}} m_{\bar{k}}^2 > 0,$$

then

$$\dot{V}(\mathbf{z}) \leq -\beta S(\mathbf{f})^{-1} \mathbf{z} \widetilde{\mathcal{R}}^T \widetilde{\mathcal{R}} \mathbf{z}.$$

Isolating the components of $\mathbf{z}$ that are orthogonal to the nullspace of $\widetilde{\mathcal{R}}$, denoted $\mathbf{z}_\perp$, then

$$\begin{aligned} \dot{V}(\mathbf{z}_\perp) &\leq -\beta S(\mathbf{f})^{-1} \lambda_q \left[\widetilde{\mathcal{R}}^T \widetilde{\mathcal{R}} \right] \mathbf{z}_\perp^T \mathbf{z}_\perp \\ &= -\beta S(\mathbf{f})^{-1} \lambda_q \left[\widetilde{\mathcal{R}}^T \widetilde{\mathcal{R}} \right] V(\mathbf{z}_\perp), \end{aligned} \tag{3.2.9}$$

where $\lambda_q \left(\widetilde{\mathcal{R}}^T \widetilde{\mathcal{R}} \right) > 0$ is the smallest non-zero eigenvalue of $\widetilde{\mathcal{R}}^T \widetilde{\mathcal{R}}$. Hence, the dynamics will converge exponentially to the nullspace of $\widetilde{\mathcal{R}}$, or equivalently to $\chi(\Theta)$, by La Salle's theorem [**77**]. □

Theorem 28 describes convergence to the set $\chi(\Theta)$. To guarantee that the steady state formation is parallel to $\mathbf{f}$, the framework must be bearing rigid. With this is mind, Zhao and Zelazo [**39**] examined the effect of a small change in agent positions $\triangle\mathbf{r} \in \mathbb{R}^{2n}$ with respect to the bearing measurements, where if $\mathcal{R}(\Theta) \triangle\mathbf{r} = \mathbf{0}$, then $\triangle\mathbf{r}$ is called an *infinitesimal bearing motion*. An infinitesimal bearing motion corresponding to a translation or a scaling of the whole framework is called *trivial*. The framework $\Theta(\mathcal{G}, \mathbf{f})$ is called *infinitesimally bearing rigid* if all infinitesimal bearing motions are trivial. Intuitively, this means that such frameworks will appear to maintain their shape, regardless of scaling or position, under the dynamics (3.2.1b). We now state a rank condition on the bearing rigidity matrix for checking if a given framework exhibits infinitesimal bearing rigidity.

THEOREM 29. [**78**] *A framework* $\Theta(\mathcal{G}, \mathbf{f})$ *is infinitesimally bearing rigid, if and only if*

$$\mathbf{rank}\left[\mathcal{R}(\Theta)\right] = 2n - 3,$$

with the nullspace of $\mathcal{R}(\Theta)$ *spanned by orthogonal vectors* $\mathbf{v}_1 = F^T \begin{bmatrix} \mathbf{1}^T & \mathbf{0}^T \end{bmatrix}^T$, $\mathbf{v}_2 = F^T \begin{bmatrix} \mathbf{0}^T & \mathbf{1}^T \end{bmatrix}^T$, *and* $\mathbf{v}_3 = \tilde{\mathbf{f}}$. *Here,* $F = \begin{bmatrix} I_n \otimes \begin{bmatrix} 1 & 0 \end{bmatrix} \\ I_n \otimes \begin{bmatrix} 0 & 1 \end{bmatrix} \end{bmatrix}$ *and* $\tilde{\mathbf{f}}$ *is the underlying unit formation.*

The vectors $\mathbf{v}_1$, $\mathbf{v}_2$ and $\mathbf{v}_3$ in Theorem 29 capture the modes representing the invariance of the bearing measurement to translation in x, translation in y, and scale, respectively.

A consequence of Theorem 29 is that the bearing-compass dynamics will converge to a formation parallel to $\mathbf{f}$ if the underlying framework is bearing rigid. Further, as the dynamics are invariant to scale and centroid by Proposition 26, then the dynamics will converge to one of the two points in $\xi_{\pm}(\mathbf{f}, \boldsymbol{r})$. Summarized in the following corollary of Theorem 28, this will almost always be the positively scaled most similar formation $\xi_{+}(\mathbf{f}, \mathbf{r})$, with $\xi_{-}(\mathbf{f}, \mathbf{r})$ corresponding to an unstable equilibrium point.

COROLLARY 30. *Let the framework* $\Theta(\mathcal{G}, \mathbf{f})$ *be infinitesimally bearing rigid. Under the unforced dynamics (3.2.1b),* $\mathbf{r}(t)$ *will almost globally exponentially converge to* $\xi_{+}(\mathbf{f}, \mathbf{r}_0)$*, with the worst-case convergence rate proportional to* $\lambda_4\left[\widetilde{\mathcal{R}}(\Theta)^T \widetilde{\mathcal{R}}(\Theta)\right]$.

Thus far, we have examined how the bearing-compass dynamics perform when unforced, i.e. when $\tilde{\mathbf{u}} = \mathbf{0}$. In the next chapter, we relax this assumption and explore the behavior of the dynamics when they are forced.

CHAPTER 4

Controlling a Bearing-Compass Dynamics

In Chapter 3, we studied the bearing-compass dynamics (3.2.1) and derived properties relating to how the dynamics will evolve over time. Further, we derived how these dynamics will evolve in the presence of an external forcing term $\tilde{\mathbf{u}}$. However, we did not explicitly choose a $\tilde{\mathbf{u}}$ to accomplish a given objective. In this chapter, we will identify several properties that will be useful when designing distributable controllers. We will extend these results further in Chapter 5.

4.1. Additive Control

Another result following from Propositions 24 and 25 is that control of two agents can achieve scaling without translation of the formation. This scaling, unlike for the single agent case, can be achieved without knowledge of the direction of the centroid. This observation is summarized in the following corollary.

COROLLARY 31. *If two agents, not necessarily adjacent in $\mathcal{G}$, apply equal magnitude control inputs along the vector between them, but in opposite directions, the centroid of the formation $C(\mathbf{r})$ remains stationary while the scale $S(\mathbf{r})$ decreases when the agents move towards one another, and increases otherwise. More specifically, the change in scale is proportional to the distance between these two agents and inversely proportional to the current formation scale as*

$$\frac{\partial S(\mathbf{r})}{\partial t} = -\frac{2}{nS(\mathbf{r})}\mathbf{r}_{ij}^T\mathbf{u}. \tag{4.1.1}$$

PROOF. Consider two agents i and j having a forced control $\tilde{\mathbf{u}}_i = -\tilde{\mathbf{u}}_j = \mathbf{u}$. Our first observation is that

$$\sum_{i \in V} \tilde{\mathbf{u}}_i = \tilde{\mathbf{u}}_i + \tilde{\mathbf{u}}_j = \mathbf{u} - \mathbf{u} = 0. \tag{4.1.2}$$

Substituting Eq. (4.1.2) into Proposition 24 it is clear that $\dot{C}(\mathbf{r}) = \mathbf{0}$. Without loss of generality, assume that the centroid $C(\mathbf{r})$ is at the origin, meaning $\mathbf{q}_i = \mathbf{r}_i$. Using Eq. (4.1.2), the formation scale dynamics from Proposition 25 evolve as

$$\begin{aligned}
\frac{\partial S(\mathbf{r})}{\partial t} &= \frac{2}{nS(\mathbf{r})} \sum_{i \in V} \mathbf{q}_i^T \left(\tilde{\mathbf{u}}_i - \frac{1}{n} \sum_{j \in V} \tilde{\mathbf{u}}_j \right) \\
&= \frac{2}{nS(\mathbf{r})} \sum_{i \in V} \mathbf{r}_i^T \tilde{\mathbf{u}}_i \\
&= \frac{2}{nS(\mathbf{r})} \left[\mathbf{r}_i^T \mathbf{u} - \mathbf{r}_j^T \mathbf{u} \right] \\
&= -\frac{2}{nS(\mathbf{r})} \mathbf{r}_{ij}^T \mathbf{u},
\end{aligned}$$

completing the proof. □

An example of Corollary 31 can be seen in Figure 3.2.2b, whereby the formation is scaled while the centroid remains stationary.

To complement Corollary 31 we examine a scenario whereby pure translation without scaling can occur. This can be achieved using a broadcast control approach where all agents apply the same control magnitude and direction, i.e., a common additive $\overline{\mathbf{u}}$. In practice, broadcast communication scales well with the size of the network since no agent-specific communication is required.

COROLLARY 32. *If all agents $i \in V$ have the same external control $\tilde{\mathbf{u}}_i = \overline{\mathbf{u}}$, then the centroid $C(\mathbf{r})$ evolves in time as*

$$\frac{\partial C(\mathbf{r})}{\partial t} = \overline{\mathbf{u}} \tag{4.1.3}$$

and the scale $S(\mathbf{r})$ evolves as

$$\frac{\partial S(\mathbf{r})}{\partial t} = 0. \tag{4.1.4}$$

PROOF. Equation (4.1.3) follows directly from Proposition 24.

If we expand Eq. (3.2.4), we have

$$\begin{aligned}
\frac{\partial S(\mathbf{r})}{\partial t} &= \frac{2}{nS(\mathbf{r})} \sum_{i \in V} \mathbf{q}_i^T \left(\tilde{\mathbf{u}}_i - \frac{1}{n} \sum_{j \in V} \tilde{\mathbf{u}}_j \right) \\
&= \frac{2}{nS(\mathbf{r})} \sum_{i \in V} \mathbf{q}_i^T \left(\overline{\mathbf{u}} - \frac{1}{n} \sum_{j \in V} \overline{\mathbf{u}} \right) \\
&= \frac{2}{nS(\mathbf{r})} \sum_{i \in V} \mathbf{q}_i^T (\overline{\mathbf{u}} - \overline{\mathbf{u}}) \\
&= 0,
\end{aligned}$$

completing the proof. □

4.2. Rotational Control

We now examine a non-additive type of broadcast control, one that dynamically rotates the unit vectors in Θ at a constant rate. We consider the time varying bearing set $\Theta(t) = \{\hat{\mathbf{f}}_{\bar{k}}(t)\}$, with $\hat{\mathbf{f}}_{\bar{k}}(t) = R(\theta(t))\mathbf{f}_{\bar{k}}$ for all $\hat{\mathbf{f}}_{\bar{k}} \in \Theta$,

$$R(\theta) = \begin{bmatrix} \cos\theta & -\sin\theta \\ \sin\theta & \cos\theta \end{bmatrix}$$

is the rotation matrix, and $\dot{\theta} = \omega \in \mathbb{R}$ is constant. This control law can be realized by broadcasting to all agents simultaneously the value $\dot{\theta}$. The dynamics (3.2.1b) becomes

$$\dot{\mathbf{r}} = \sum_{j \in \mathcal{N}(i)} w_{ij} \left(\hat{\mathbf{r}}_{ij}^T \hat{\mathbf{f}}_{ij}^{\perp} \right) \hat{\mathbf{r}}_{ij}^{\perp}. \tag{4.2.1}$$

The equilibrium trajectory $\mathbf{f}(t)$ is a rotation of the formation $\mathbf{f} = \xi(\mathbf{r}_0, \Theta)$ about its centroid, i.e., $\mathbf{f}(t) = (I_n \otimes R(\theta(t)))(\mathbf{f} - C(\mathbf{f}))$. It is straightforward to see that $C(\mathbf{r})$ and $S(\mathbf{r})$ will be constant under this type of control. The following theorem states that the trajectory $\mathbf{r}(t)$ will ultimately be achieved up to some bound b.

THEOREM 33. *Given the graph is bearing rigidity, the equilibrium trajectory of (4.2.1) is bounded for all $t \geq 0$ and ultimately bounded by*

$$b = \frac{4mS(\mathbf{r}_0)\dot{\theta}}{\alpha\left(\beta S(\mathbf{f})^{-1}\lambda_4\left[\widetilde{\mathcal{R}}^T\widetilde{\mathcal{R}}\right]\right)},$$

and where $\alpha \in (0,1)$ is an arbitrary constant.

PROOF. For the rotating case dynamics (4.2.1), for a *frozen* θ [**77**] the frozen equilibrium point is $\mathbf{r} = (I_n \otimes R(\theta))\mathbf{f} := \mathbf{f}_\theta$. This frozen θ, under the change of variable $\mathbf{z} = \mathbf{r} - \mathbf{f}_\theta$, has dynamics $\dot{\mathbf{z}}_i = g_i(\mathbf{z}, \mathbf{f}_\theta)$, where $g_i(\cdot)$ is defined in (3.2.5), and analyzed in Theorem 28. The non-frozen rotating system consequently has dynamics, for each $i \in V$,

$$\dot{\mathbf{z}}_i = g_i(\mathbf{z}, \mathbf{f}_\theta) - \frac{\partial \mathbf{f}_\theta}{\partial \theta}\dot{\theta}. \tag{4.2.2}$$

We proceed to analyze this system as a slow varying system drawing upon the comparison lemma [**77**] to show ultimate boundedness. Note that

$$\begin{aligned}\left\|\frac{\partial \mathbf{f}_\theta}{\partial \theta}\right\| &= \|(I_n \otimes R'(\theta))\mathbf{f}\| \\ &= \|\mathbf{f}\| \\ &\triangleq L.\end{aligned}$$

We have

$$c_1\|\mathbf{z}\|^2 \leq V(\mathbf{z}) \leq c_2\|\mathbf{z}\|^2,$$

$$\dot{V}(\mathbf{z}) \leq -c_3\|\mathbf{z}\|^2,$$

$$\left\| \frac{\partial V}{\partial \mathbf{z}} \right\| = \|\mathbf{z}\| \leq c_4 \|\mathbf{z}\|,$$

and

$$\left\| \frac{\partial V}{\partial \theta} \right\| = 0 \leq c_5 \|\mathbf{z}\|^2,$$

where $c_3 = \beta S(\mathbf{f})^{-1} \lambda_4 \left[\widetilde{\mathcal{R}}^T \widetilde{\mathcal{R}}\right]$ from (3.2.9), $c_1 = c_2 = \frac{1}{2}$, $c_4 = 1$, and $c_5 > 0$ (an arbitrary positive constant). Applying [**77**, Thm. 9.3], for $||\dot{\theta}|| \leq \varepsilon$ and $\mathbf{z} \in D(\delta)$ then the solutions of (4.2.2) are bounded for all $t \geq 0$ and ultimately bounded by

$$b = \frac{c_2 c_4 L \varepsilon}{\alpha (c_1 c_3 - \varepsilon c_2 c_5)} = \frac{4m \|\mathbf{f}\|^2 \dot{\theta}}{\alpha \left(\beta S(\mathbf{f})^{-1} \lambda_4 \left[\widetilde{\mathcal{R}}^T \widetilde{\mathcal{R}}\right]\right)}.$$

Since c_5 can be selected arbitrarily small, $\dot{\theta}$ is constant, and we can let $\varepsilon = \dot{\theta}$. □

Not surprisingly, the bound b in Theorem 33 exhibits similar features to the convergence rate in Theorem 28. Smaller bounds are achieved with improved network connectivity, less edges, smaller scale and closer initial conditions to the equilibrium trajectory. Further, better bounds are formed with a slower rotation rate $\dot{\theta}$. These features can be observed in Figure 4.2.1, comparing (a) with larger $\frac{\lambda_4[\widetilde{\mathcal{R}}^T \widetilde{\mathcal{R}}]}{m}$ than (b). When, the rotation rate is too high the overall formation shape can not be maintained as observed in Figure 4.2.1d.

The additive control approach explored earlier in the section can also be combined with a rotation control. An example of this is displayed in Figure 4.2.1c, with a rotation coupled with a pure scaling as per Corollary 31.

We have shown that we can manipulate the formation to cause rotations, changes in scale, and change in position using one, two, or all agents. The next chapter will presents methods to select particularly effect agents, known as leaders, to manipulate the formation.

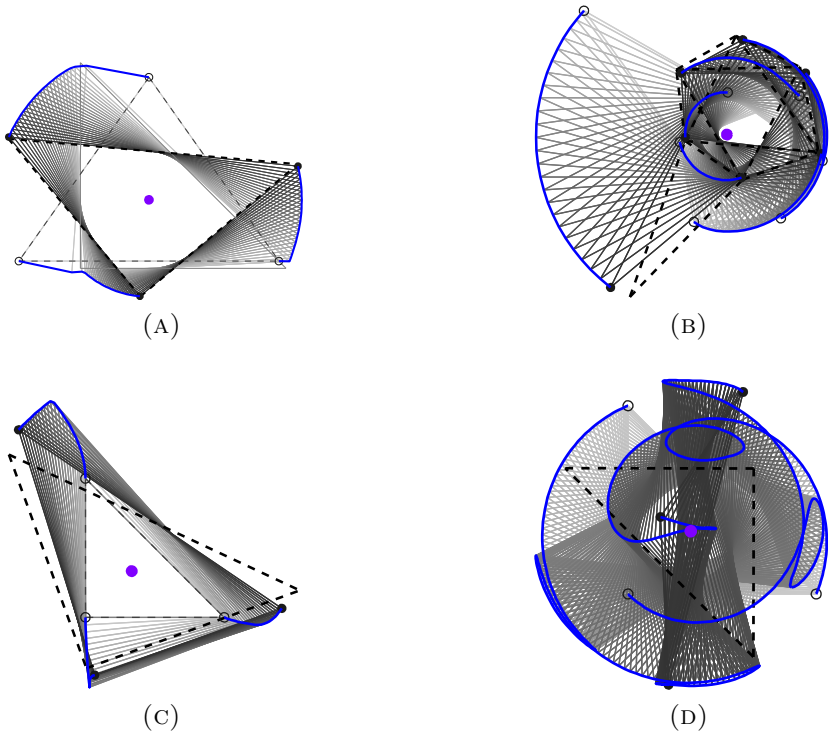

(A) (B) (C) (D)

FIGURE 4.2.1. Tracking a rotating formation. A) Right triangle formation. B) Asymmetric formation on 7 agents. C) Pure scale with the same additive control in Figure 3.2.2b and constant-rate rotation. D) Equilateral formation with large $\dot{\theta}$.

CHAPTER 5

Leader Selection for Internal Manipulation

One of the attributes previously explored for dynamics (3.2.1) is the application of external control on all or a subset of the agents referred to as *leader* agents to manipulate the formation. Motivated by *intuitive* human-swarm formation interactions, we focused on control strategies that can translate and scale the formation. As specific controls are required to be communicated to each agent to perform these strategies, communication costs can restrict the number of agents able to participate in a maneuver. When constrained to a finite control, some agents can more effectively instigate these maneuvers. Further, translation without scaling, referred to as *pure* translation, can be achieved by applying carefully selected external leader control. Similarly, translation can be maintained while varying scale when the external leader control values are restricted. These observations indicate that an intelligent selection of control agents and control signals is required when interacting with the swarm.

5.1. Translation and Scale

This section discusses solutions and approximate solutions for the problem of selecting a leader set S for effective formation translation and scaling.

As mentioned in Proposition 24, the dynamics of the formation centroid is

$$\frac{\partial C}{\partial t} = \frac{1}{n}\sum_{i\in S}\tilde{u}_i,$$

which provides a direct method for leader agents to translate the formation. Consider a translation of the formation in the direction of the unit vector $\mathbf{h} \in \mathbb{R}^2$. If each agent can apply a cumulative unforced and forced control of magnitude at most $u_{\max}$ then, as the unforced dynamics of agent i is at most $\mathcal{N}(i)$ from Proposition 22, it follows that $\|\tilde{\mathbf{u}}_i\| \leq u_{\max} - |\mathcal{N}(i)|$.

Here, we assume there is sufficient control to apply the unforced dynamics, i.e., $u_{\max} \geq \mathcal{N}(i)$. The set function describing the most suitable translation leader set S is

$$\begin{aligned} f_t(S) &= \max_{\|\tilde{\mathbf{u}}_i\| \leq u_{\max} - |\mathcal{N}(i)|} \mathbf{h}^T \left(\frac{1}{n} \sum_{i \in S} \tilde{\mathbf{u}}_i \right) \\ &= \frac{1}{n} \sum_{i \in S} (u_{\max} - |\mathcal{N}(i)|), \end{aligned} \tag{5.1.1}$$

corresponding to $\tilde{\mathbf{u}}_i = (u_{\max} - \mathcal{N}(i))\,\mathbf{h}$ for each agent i. For this case, every agent applies their maximum control in the direction of $\mathbf{h}$. We note that a similar formulation can be obtained if $\mathbf{w} \neq \mathbf{1}$, but is omitted for clarity.

A similar setup occurs for maximizing the change in scale of the formation, from Proposition 25 as

$$\frac{\partial S}{\partial t} = \frac{2}{nS\,(\mathbf{r})} \sum_{i \in V} \mathbf{q}_i^T \left(\tilde{\mathbf{u}}_i - \frac{1}{n} \sum_{j \in V} \tilde{\mathbf{u}}_j \right),$$

recalling that $\mathbf{q}_i = \mathbf{r}_i - C(\mathbf{r})$. Under the cumulative control constraint $u_{\max}$ then

$$\begin{aligned} f_s(S) &= \max_{\|\tilde{\mathbf{u}}_i\| \leq u_{\max} - |\mathcal{N}(i)|} \frac{2}{nS\,(\mathbf{r})} \sum_{i \in V} \mathbf{q}_i^T \left(\tilde{\mathbf{u}}_i - \frac{1}{n} \sum_{j \in V} \tilde{\mathbf{u}}_j \right) \\ &= 2 \sum_{i \in S} \left(u_{\max} - |\mathcal{N}(i)| \right) \|\mathbf{q}_i\|, \end{aligned} \tag{5.1.2}$$

corresponding to

$$\tilde{\mathbf{u}}_i = (u_{\max} - |\mathcal{N}(i)|)\,\hat{\mathbf{q}}_i$$

for each agent i. The control strategy corresponds to every leader applying their maximum control outward from the direction of the centroid $\hat{\mathbf{q}}_i$. The minimization of the change in scale of the formation can be similarly formulated. In fact if $\tilde{\mathbf{u}}_i$ is the solution of the maximization problem, then $-\tilde{\mathbf{u}}_i$ is the solution to the minimization of change in scale.

Set functions $f_t(S)$ and $f_s(S)$ are in fact both modular functions from Definition 10. Maximization over modular functions with cardinality constraints, e.g. $|S| \leq K$, is easy, requiring evaluation of $w(s)$ over all agents s and then selecting the K largest. Consequently, for the centroid set function $f_t(S)$ the best agent set is composed of agents with the K smallest

degrees. Similarly, the best agent set for scale manipulation based on $f_s(S)$ is composed of agents that are far from the center with small degrees. For example, if all agents have equal degree than the optimal set will be composed of the k agents furthest from the center.

5.2. Information Propagation

The detriment of the optimal leader sets of the previous section is that leader agents often have a low degree which tends to imply a small distance centrality, i.e., $\sum_{i=1}^{n} \text{dist}(i, S)$ is large. Consequently, the translation or scale information presented by agents in S can be slow to propagate through the dynamics over the graph. One approach to mitigate this effect is to supplement the set functions $f_t(S)$ and $f_s(S)$ with a centrality-promoting measure $f_{\mathcal{G}}(S)$ by optimizing over both, namely

$$f(S) = f_x(S) + f_{\mathcal{G}}(S), \tag{5.2.1}$$

where $f_x(S)$ is either $f_t(S)$ or $f_s(S)$. Here, we choose

$$f_{\mathcal{G}}(S) = -c \sum_{j=1}^{n} \text{dist}(j, S) \tag{5.2.2}$$

for some weight $c > 0$ which penalizes the set S for large distance centrality.

The set function $f_{\mathcal{G}}(S)$ falls into a class of set functions known as monotone increasing submodular functions. The submodularity of $f_{\mathcal{G}}(S)$ follows from the relation

$$\begin{aligned} f_{\mathcal{G}}(B \bigcup \{s\}) - f_{\mathcal{G}}(B) &= c \sum_{j=1}^{n} \max\{0, \text{dist}(j, B) - \text{dist}(j, s)\} \\ &\leq c \sum_{j=1}^{n} \max\{0, \text{dist}(j, A) - \text{dist}(j, s)\} \\ &= f_{\mathcal{G}}(A \cup \{s\}) - f_{\mathcal{G}}(A), \end{aligned}$$

and the monotonicity of $f_{\mathcal{G}}(S)$ follows from the observation that adding a vertex to a set can never increase the sets distance to agents in the graph.

Applying the property that the sum of a submodular function and a modular function is submodular [**20**], then Eq. (5.2.1) is also a monotone increasing, submodular function. Now, the maximization of such a monotone increasing, submodular function for $|S| \leq K$ is generally NP-hard. In fact, a special case of maximizing $f_{\mathcal{G}}(S)$ is the vertex cover problem shown to be NP-complete [**79**]. A polynomial time alternative is to apply a greedy algorithm which is provably close to the optimal [**19**], a process captured in Theorem 14. In fact, this is the best performing polynomial time algorithm over general monotone increasing submodular functions [**19**].

An alternative candidate for $f_{\mathcal{G}}(S)$ is the cut size corresponding to the partition S and $V-S$. This is the number of edges linking the input node set S to the rest of the swarm. It presents a different measure of connectedness and therefore information propagation. A special case of maximizing $f_{\mathcal{G}}(S)$ is the maximum cut problem, one of Karp's 21 NP-complete problems [**79**]. The cut size is also a monotone increasing, submodular function and so a greedy heuristic can be applied with guaranteed suboptimal performance.

5.3. Pure Translation and Scale

A consequence of the control strategies corresponding to the set functions (5.1.1) and (5.1.2) is that the formation may be inadvertently scaled when the centroid is translated; similarly centroid translation can inadvertently occur under scaling. This is particularly detrimental in the case of scale variation, as over time, $\mathbf{q}_i(\mathbf{r})$ varies with centroid location, so unless the forced additive control is applied instantaneously the optimal S under the set function (5.1.2) may not in fact be the optimal scaling set over a trajectory.

An alternative is to select $\tilde{\mathbf{u}}_i$ for all $i \in S$ such that only a pure translation or scale occurs. Formally, the control input $\tilde{\mathbf{u}}_i$ is designed such that $\frac{\partial S(\mathbf{r})}{\partial t} = 0$ and $\frac{\partial C(\mathbf{r})}{\partial t} = \mathbf{0}$ for scale and centroid invariance, respectively.

For optimal translation leader selection under this restriction, an alternative set function can be considered which optimizes for pure translation in the desired direction $\mathbf{h}$, while exhibiting no translation in other directions or scaling. The set function is defined, via an

optimization problem over all $\tilde{\mathbf{u}}_i$ such that $i \in S$, as

$$f_{t'}(S) = \max \mathbf{h}^T \sum_{i \in S} \tilde{\mathbf{u}}_i \tag{5.3.1a}$$

$$\text{s.t.} \quad \sum_{i \in S} \mathbf{q}_i^T \tilde{\mathbf{u}}_i = 0 \tag{5.3.1b}$$

$$(\mathbf{h}^{\perp})^T \sum_{i \in S} \tilde{\mathbf{u}}_i = 0 \tag{5.3.1c}$$

$$\|\tilde{\mathbf{u}}_i\| \leq u_{\max} - \mathcal{N}(i), \text{ for all } i \in S.$$

The equality constraint in Eq. (5.3.1b) mandates that the scale remains invariant while Eq. (5.3.1c) prohibits translations not aligned with $\mathbf{h}$. Unlike the set function in Eq. (5.1.1), $f_{t'}(S)$ does not have a closed form solution. Given the set S, $f_{t'}(S)$ can be solved efficiently as a semidefinite optimization problem, or more specifically as a linear cost problem with linear and quadratic constraints. Unfortunately, $f_{t'}(S)$ is not submodular and so the techniques of the previous section can not be applied to form a $1 - 1/e$ approximate leader selection algorithm with cardinality constraints on S.

The problem of leader selection under the cost $f_{t'}(S)$ can be posed as an mixed-integer quadratic programming (MIQP) problem, optimizing over $\tilde{\mathbf{u}}_1, \ldots, \tilde{\mathbf{u}}_n$ and binary variables $z_1, \ldots, z_n$, as

$$J_{t'} = \max \mathbf{h}^T \sum_{i=1}^{n} \tilde{\mathbf{u}}_i$$

$$\text{s.t.} \quad \sum_{i=1}^{n} \mathbf{q}_i^T \tilde{\mathbf{u}}_i = 0$$

$$(\mathbf{h}^{\perp})^T \sum_{i=1}^{n} \tilde{\mathbf{u}}_i = 0$$

$$\|\tilde{\mathbf{u}}_i\| \leq z_i \left(u_{\max} - \mathcal{N}(i)\right), \text{ for all } i \in V \tag{5.3.2a}$$

$$\sum_{i=1}^{n} z_i \leq K \tag{5.3.2b}$$

$$z_i \in \{0, 1\}, \text{ for all } i \in V. \tag{5.3.2c}$$

The binary variable z_i, through inequality (5.3.2a), captures whether the agent i is selected as a leader, while the inequality (5.3.2b) enforces the cardinality constraint, $|S| \leq K$. This problem is difficult to solve exactly. In fact for $u_{\max} \to \infty$, the problem becomes the 0-1 integer program which is NP-complete [**79**]. One approach is to find an approximate solution by performing an integer relaxation of constraint (5.3.2c) to $z_i \in [0, 1]$. The optimal $J_{\mathrm{t}'}$ will be generated by some contribution of all agents denoted through the magnitude of z_i. Selecting the agents which correspond to the largest K elements of z_i forms an approximate agent set S. Defining the optimal agent selection as

$$S^* = \underset{|S| \leq K}{\mathbf{argmax}} \left[f_{t'}(S) \right]$$

then

$$0 \leq f_{t'}(S) \leq f_{t'}(S^*) \leq J_{t'}.$$

Hence, we have the relation

$$\frac{f_{t'}(S^*) - f_{t'}(S)}{f_{t'}(S^*)} \leq \frac{J_{t'} - f_{t'}(S)}{f_{t'}(S)}. \tag{5.3.3}$$

Thus, for small $J_{t'} - f_{t'}(S)$, S serves as a good approximation of S^*. The additive control $\tilde{\mathbf{u}}_i$ for $i \in S$ for this centroid maneuver corresponds to the optimal solution of (5.3.1a).

A similar approach can be adopted for the selection of leader controls for pure scaling with centroid invariance using an alternative set function

$$\begin{aligned} f_{s'}(S) \quad &= \quad \max \sum_{i \in S} \mathbf{q}_i^T \tilde{\mathbf{u}}_i \\ \text{s.t.} \quad & \sum_{i \in S} \tilde{\mathbf{u}}_i = 0 \\ & \|\tilde{\mathbf{u}}_i\| \leq u_{\max} - \mathcal{N}(i), \text{ for all } i \in S. \end{aligned} \tag{5.3.4a}$$

The accompanying MIQP, which for $u_{\max} \to \infty$ is also an NP-complete 0-1 integer program, is

$$\begin{aligned} J_{s'} &= \max \sum_{i=1}^{n} \mathbf{q}_i^T \tilde{\mathbf{u}}_i \\ \text{s.t.} \quad & \sum_{i=1}^{n} \tilde{\mathbf{u}}_i = 0 \\ & \|\tilde{\mathbf{u}}_i\| \leq z_i \left(u_{\max} - \mathcal{N}(i)\right), \text{ for all } i \in V \\ & \sum_{i=1}^{n} z_i \leq K \\ & z_i \in \{0,1\}, \text{ for all } i \in V. \end{aligned}$$

The integer relaxation approach produces a similar inequality for the suboptimal scale maneuver

$$\frac{f_{s'}(S^*) - f_{s'}(S)}{f_{s'}(S^*)} \leq \frac{J_{s'} - f_{s'}(S)}{f_{s'}(S)}, \tag{5.3.6}$$

where

$$S^* = \underset{|S| \leq K}{\mathbf{argmax}} \left[f_{s'}(S)\right].$$

5.4. Examples

The leader selection algorithms were exercised on our unicycle testbed introduced in §0.5 with the objective of demonstrating the scaling leader selection process. A unicycle particle tracking dynamics coupled with dynamics (3.2.1) was implemented on the testbed, with bearing measurements $\hat{\mathbf{r}}_{ij}$ supplied to each agent i via a Vicon motion-capture system.

The dynamics was applied to three vehicles with initial vehicle positions forming a right triangle and graph $\mathcal{G}$ a complete graph. The desired formation shape, defined through the set $\Theta(\mathcal{G})$, corresponds to a right-triangle in a different orientation. The resultant trajectory is depicted in Figure 5.4.1. The final formation shape is correctly acquired and demonstrates good agreement between the particle tracking dynamics and bearing-compass dynamics.

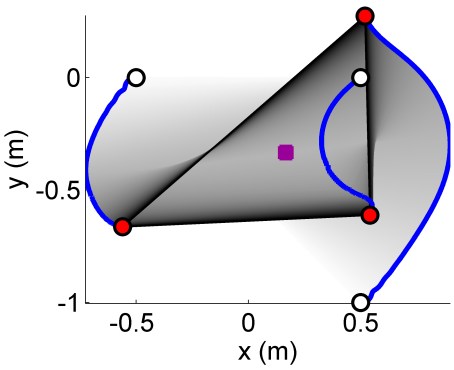

FIGURE 5.4.1. Initial and final positions are marked with empty and filled circles, respectively, and the centroid by a solid square. The trajectory of the agents is denoted with a solid line between empty and filled circles. The graph topology is indicated by lines between filled circles.

To examine the scaling leader selection process, the dynamics were applied to a 9 vehicle swarm. The initial formation shape and scale, and graph $\mathcal{G}$ are provided in Figure 5.4.2a. With the objective of maximizing the scale of the formation, a greedy leader selection algorithm was implemented over the modular cost function in Eq. (5.1.2), selecting the optimal leader set with cardinality three. The consequent formation scaling is depicted in Figure 5.4.2a with the scale motion and centroid motion illustrated in Figure 5.4.2b and 5.4.2c, respectively. As expected, the selected leaders are those furthest from the centroid with low degree. The corresponding control vectors $\tilde{\mathbf{u}}_i$, supplied for $t \in [10, 30]$, move the leader agents away from the centroid and in doing so scale the swarm. We observe an eventual 35% scaling of formation. There is also an inadvertent shift of the centroid by 15 cm.

An alternate cost function in Eq. (5.3.1) was examined so as to avoid the unwanted shift in centroid observed in Figure 5.4.2c. The proposed integer relaxed optimization problem (5.3.2) explored in §5.3 was solved to generate a sub-optimal leader set with cardinality three. The bound from Eq. (5.3.3) is

$$\frac{J_{s'} - f_{s'}(S)}{f_{s'}(S)} \leq 0.31,$$

indicating the solution is within 31% of the optimal. After examining all possible leader sets, we determined the solution is in fact optimal. The subsequent trajectory of the same

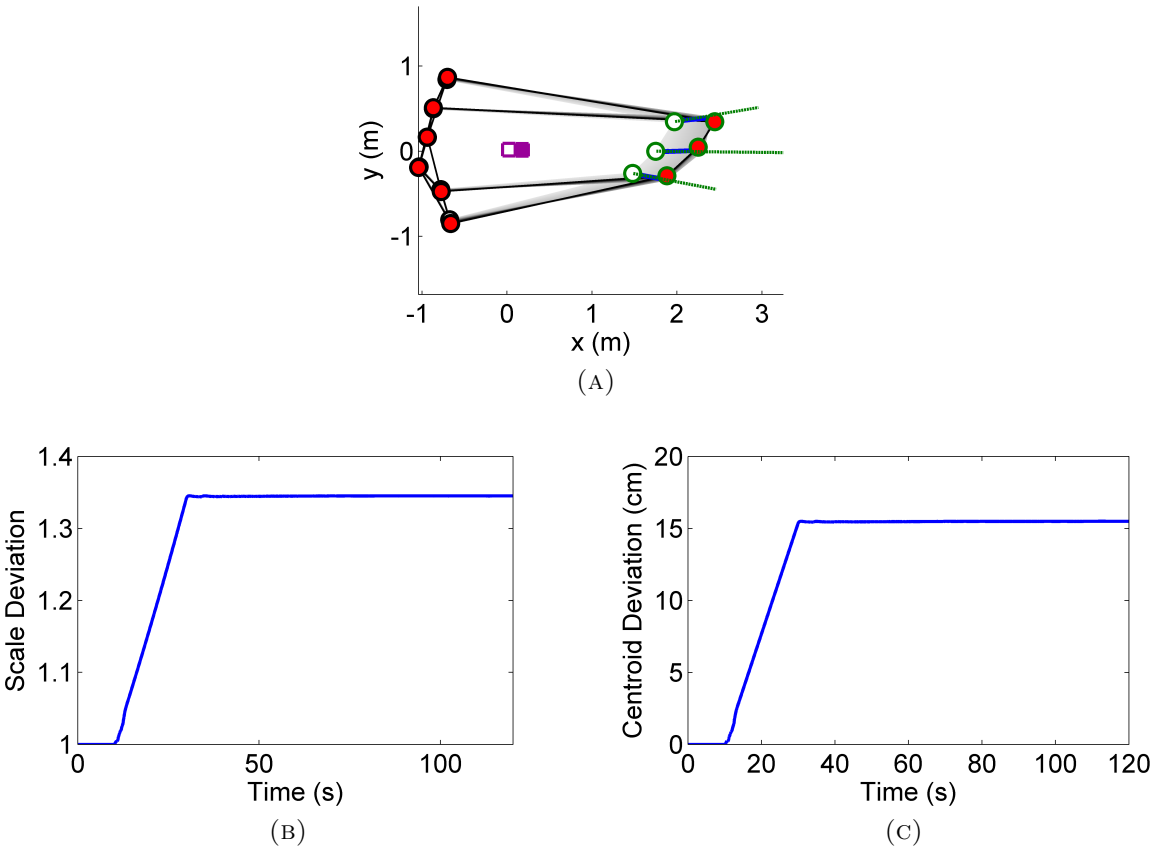

(A)

(B)

(C)

FIGURE 5.4.2. A) A 9 agent formation under scale with leader selection dictated by cost function (5.1.2). (B) and (C) The resultant scale $S(\mathbf{r})$ and centroid $C(\mathbf{r})$ deviations over time. The initial position, final position, trajectory, graph, and centroid are denoted as in Figure 5.4.1. The control vector $\tilde{\mathbf{u}}_i$ for each leader agent i is indicated with a dashed line from node i.

9 agent scenario in Figure 5.4.2 is depicted in Figure 5.4.3a. Unlike in Figure 5.4.2, the selected leaders are not those that are furthest from the centroid, but balanced around it. The corresponding leader controls, supplied for $t \in [10, 30]$, also no longer point directly away from the centroid as they must enforce the centroid invariant constraints. The scale deviation, depicted in Figure 5.4.3b, shows a scaling of 30%. Figure 5.4.3c illustrates the more favorable centroid deviation with only a 0.5 cm shift from the initial location opposed in 15 cm for cost function (5.1.2).

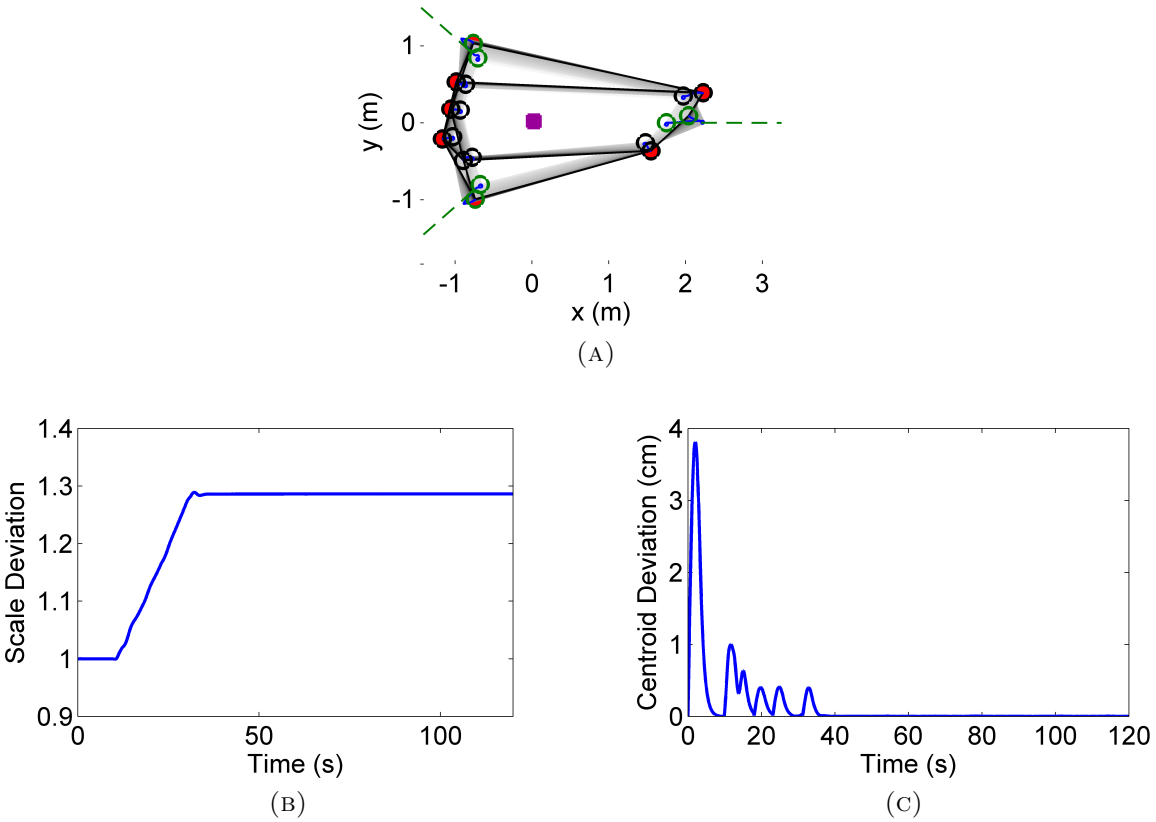

(A)

(B)

(C)

FIGURE 5.4.3. (A) A 9 agent formation under scale with leader selection dictated by cost function (5.3.5). (B) and (C) The resultant scale $S(\mathbf{r})$ and centroid $C(\mathbf{r})$ deviations over time. The initial position, final position, trajectory, graph, and centroid are denoted as in Figure 5.4.1. The control vector $\tilde{\mathbf{u}}_i$ for each leader agent i is indicated with a dashed line from node i.

5.5. Concluding Remarks

In this part we explored the properties, manipulation and leader selection problem for a bearing-compass control law. Stability and invariant features were explored for the dynamics. The criteria for leader selection were based on the effectiveness of leaders to manipulate the formation's centroid location and scale. The effectiveness of these selections was illustrated on a unicycle swarm testbed.

Part 3

Rigidity-Centered Design

In this part, we extend the exploration in Part 2 of the bearing-based dynamics to formation shape acquisition. The work examines connections between the graph topology and the performance of the dynamics. The bearing rigidity matrix is shown to be key to understanding the stability and convergence of the protocol. Examining measures over the bearing rigidity matrix, the edge selection and leader selection problems are considered in Chapters 6 and 7, respectively. The part is concluded in Chapter 8 which generalizes the rigidity based approach to studying the bearing-compass dynamics to more arbitrary relative measurements.

CHAPTER 6

Edge Selection for Network Dynamic Performance

In this section, we will discuss how a bearing-rigid formation can be obtained with minimal human interaction. Our method, visualized in Figure 0.4.2, consists of taking a coarse image provided by the human operator, partitioning the image into roughly equal-sized components, constructing a set of feasible edges from which to select, and finally selecting a subset of these edges which both meet our bearing rigidity requirements and maximize some performance metric.

To partition the image, we first produce a set of agents which will participate in the formation, and denote them by the set V. The Voronoi partitioning algorithm [**80, 81**] will return the desired agent positions $\mathbf{f} = \begin{bmatrix} \mathbf{f}_1^T & \mathbf{f}_2^T & \cdots & \mathbf{f}_n^T \end{bmatrix}^T$, such that agents are roughly distributed across the image. For example, the raw image in Figure 0.4.2a is partitioned into 25 approximately equal regions, and the desired locations for agents are returned in $\mathbf{f}$.

Given a set of desired agent positions $\mathbf{f}$, we can construct a distance graph [**2**]. This graph is denoted $\mathcal{G}_D = (V, E_D)$ is composed of edges

$$E_D = \{\{i, j\} \,:\, \|\mathbf{f}_j - \mathbf{f}_i\| \leq d_{\max}\},$$

where $d_{\max}$ is chosen to be sympathetic to communication range limits of the agents (i.e., wireless signal strength or a distance such that a monocular camera can still resolve neighboring agents).

We will use the desired agent positions $\mathbf{f}$ and the feasible edge set E_D to select some $E \subseteq E_D$ such that the dynamics (3.2.1) will both converge and be optimal over various metrics, such as maximizing convergence.

In §6.1, we will explore a necessary and sufficient condition on the bearing rigidity matrix $\mathcal{R}(\Theta)$ for the dynamics to converge. More specifically, we will select an edge set $E \subseteq E_D$

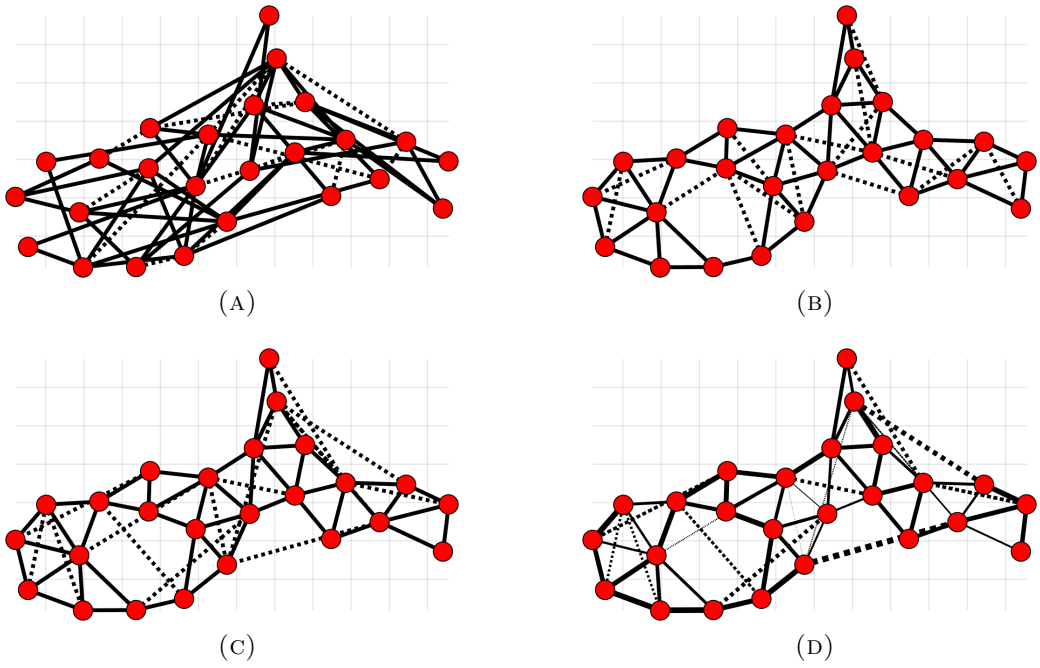

FIGURE 6.0.1. Edge selection under different metrics: A) Using $f_r(S)$ from Proposition 35, B) using $f_r(S) + \alpha f_t(S)$ from Eq. (6.2.5), C) using $f_r(S) + \alpha f_\ell(S)$ from Eq. (6.2.6), and D) same edge set as Fig. 6.0.1c but with edge weighting from §6.3.

such that the conditions on infinitesimal bearing rigidity, outlined in Theorem 29, are met, which means the formation satisfies $\mathbf{rank}\left[\mathcal{R}\left(\Theta\right)\right] = 2n - 3$.

While our formation edge set must be bearing rigid, we would also like the set to promote good performance of the dynamics. We can add additional terms to the edge selection to promote this, which we will explore in §6.2. Further, we might be given a set of edges that we must use, in which case we can optimize the weights of those edges to further improve performance. This is explored in §6.3.

An example of such a refinement can be seen in Fig. 6.0.1, where the edges have been selected from those in the distance graph in Fig. 0.4.2c.

Submodularity is key to our approach to the edge selection problem. In particular, the theorem below serves as the workhorse for the results that follow.

THEOREM 34. *Let* $S \subseteq E$ *and*

$$Q(S) = U(S)^T U(S),$$

where $U(S) = (I(S \cup S_0) \otimes I_d) U(E)$, $I(T)$ *represents the* T *columns of the identity matrix and* S_0 *is the columns of* $U(E)$ *associated with* $S = \{\emptyset\}$. *Then the following are submodular functions:*

a) $f_r(S) = \mathbf{rank}[-Q(S)]$

b) $f_t(S) = \mathbf{trace}[Q(S)]$

c) $f_\ell(S) = \mathbf{logdet}[Q(S)]$ *for* $Q(S) \succ 0$.

Furthermore, $f_t(S)$ *is, in fact, modular.*

PROOF. (a) We observe that

$$\mathbf{rank}[Q(S)] = \mathbf{rank}\left[U(S)^T U(S)\right] = \mathbf{rank}\left[U(S)^T\right].$$

The matrix $U(S)$ corresponds to the $S \cup S_0$ column pairs of $U(E)$. Maximizing $f_{\mathrm{r}}(S)$ over S is then equivalent to selecting the 2-pair columns of each $s \in S$ in $U(E)$ that maximizes the rank. This is the standard matroid rank problem and f_r is submodular [**19**].

In support of (b) and (c), observe that

$$\begin{aligned} Q(S) &= U(S)^T U(S) \\ &= U(E)^T (I(S \cup S_0) \otimes I_2)^T (I(S \cup S_0) \otimes I_2) U(E) \\ &= U(E)^T \sum_{s=\{\emptyset\}, s \in S} \left[(I(\{s\}) \otimes I_2)^T (I(\{s\}) \otimes I_2)^T \right] U(E) \\ &= Q(\emptyset) + \sum_{s \in S} Q(\{s\}). \end{aligned} \tag{6.0.1}$$

(b) As $\mathbf{trace}[Q(S)] = \sum_{s \in S} \mathbf{trace}[Q(\{s\})]$ it follows that $\mathbf{trace}[Q(S)]$ is modular.

(c) For $M \succ 0$ and $N, P \succeq 0$ then

$$\mathbf{det}(M)\,\mathbf{det}(M+N+P) \;\leq\; \mathbf{det}(M+N)\mathbf{det}(M+P)$$

from [**82**]. As $\mathbf{log}(\cdot)$ is an increasing function then

$$\begin{aligned} 0 &\leq \mathbf{log}(\mathbf{det}(M+N)\mathbf{det}(M+P)) - \mathbf{log}(\mathbf{det}M\mathbf{det}(M+N+P)) \\ &\leq \mathbf{logdet}(M+N) + \mathbf{logdet}(M+P) - (\mathbf{logdet}M + \mathbf{logdet}(M+N+P)) \\ &\leq \mathbf{logdet}(M+P)) - \mathbf{logdet}M) - (\mathbf{logdet}(M+N+P) - \mathbf{logdet}(M+N)). \end{aligned} \tag{6.0.2}$$

Consider now $A \subseteq B \subseteq \mathcal{S}$ and $s \notin B$. Assume that $Q(A) \succ 0$ as $Q(S)$ is formed by the sum of positive semidefinite matrices, then $Q(B) - Q(A), Q(\{s\}) \succeq 0$. Let $M = Q(A)$, $N = Q(B) - Q(A)$, $P = Q(\{s\})$ and applying (6.0.1) and (6.0.2) as

$$\begin{aligned} 0 &\leq \mathbf{logdet}(Q(A) + Q(\{s\}) - \mathbf{logdet}Q(A) - (\mathbf{logdet}(Q(B) + Q(\{s\}) - \mathbf{logdet}Q(B)) \\ &\leq \mathbf{logdet}Q(A \cup \{s\}) - \mathbf{logdet}Q(A) - (\mathbf{logdet}Q(B \cup \{s\}) - \mathbf{logdet}Q(B)) \end{aligned}$$

Hence, by Def. 12, $\mathbf{logdet}\left[Q\left(S\right)\right]$ is submodular. □

6.1. Selection for Bearing Rigidity

When we perform the Voronoi partitioning from §0.4, the output is the desired agent formation $\mathbf{f} = \begin{bmatrix} \mathbf{f}_1^T & \mathbf{f}_2^T & \cdots & \mathbf{f}_n^T \end{bmatrix}^T$. We then use this formation to construct the distance graph $\mathcal{G}_D$ using some maximum distance $d_{\max}$. We will be selecting subsets of these edges.

From Corollary 30, a necessary condition for dynamics (3.2.1) to converge to a formation similar to $\mathbf{f}$ is that the framework Θ is infinitesimally bearing rigid. From Theorem 29, it is then desirable to select a subset of edges $S \subseteq E_D$ so that $\mathbf{rank}\left[\mathcal{R}\right] = 2n - 3$. Representing the rigidity matrix as a matrix valued function with respect to the edges S then

$$\mathcal{R}(S) = \frac{\partial \hat{\bar{\mathbf{f}}}(S)}{\partial \mathbf{f}}$$

where $\hat{\bar{\mathbf{f}}}(S) \triangleq \begin{bmatrix} \hat{\mathbf{f}}_{\bar{s}_1}^T & \hat{\mathbf{f}}_{\bar{s}_2}^T & \cdots \end{bmatrix}^T$, for $S = \{s_1, s_2, \dots\} \subseteq E_D$. The unitless rigidity matrix $\widetilde{\mathcal{R}}(S)$ is similarly defined. We leverage this rank property in the following proposition.

Algorithm 2 Select edges which guarantee infinitesimal bearing rigidity.

Input: Graph to refine: $\mathcal{G}_D = (V, E_D)$
Ensure: $\mathbf{rank}[\mathcal{R}(E_D)] = 2n - 3$
Input: Submodular set function: $f(S), S \subseteq E_D$
1: $S \leftarrow \emptyset$
2: **while** $\mathbf{rank}[\mathcal{R}(S)] < 2n - 3$ **do**
3: $\quad e^* = \underset{e \in E_D \setminus S}{\mathbf{argmax}} \left[f(S \cup \{e\}) - f(S) \right]$ [1]
4: $\quad S \leftarrow (S \cup \{e^*\})$
5: **end while**
6: **return** S

PROPOSITION 35. *The set function*

$$f_r(S) = \mathbf{rank}\left[\mathcal{R}(S)\right] \tag{6.1.1}$$

for $S \subseteq E_D$ is submodular.

PROOF. This result follows directly from Theorem 34.a by letting $S_0 = \{\emptyset\}$ and

$$\begin{aligned} U(S) &= \mathcal{R}(S) \\ &= (I(S \cup S_0) \otimes I_2)\mathcal{R}(E_D). \end{aligned}$$

□

Since we have shown that the rank of the bearing rigidity matrix $\mathcal{R}$ is submodular over the underlying edge set E, we can apply Theorem 14 to select edges in a greedy fashion, leading to an approximately optimal edge set. This process is described in Algorithm 2.

6.2. Selection for Convergence

In §6.1, we showed how to select edges such that the resulting formation is bearing rigid. However, in large formations with many possible edges, it is likely that many such selections will meet this minimum rank requirement, and some selections might offer better performance than others. In this section, we explore ways to promote formation convergence as a part of

[1] If, as in Theorem 14, $R > 1$, then this line will select the subset $e \subseteq E_D \setminus S$ such that $|e| = R$ if $|E_D \setminus S| \geq R$ and $|e| = |E_D \setminus S|$ otherwise.

the edge selection process. The underlying Lyapunov function and the associated Lyapunov rate from Theorem 28 is $V = \frac{1}{2}\mathbf{z}^T\mathbf{z}$ and $\dot{V} \leq -S\left(\mathbf{f}\right)^{-1}\mathbf{z}^T Q\mathbf{z}$, respectively. Explicitly encoding the edges $S \subseteq E_D$ that contribute to Q then

$$Q(S) = \widetilde{\mathcal{R}}(S)^T \mathcal{D}_{\bar{k}(S)}\left[m_{\bar{k}}^2 I_2\right]\widetilde{\mathcal{R}}(S), \tag{6.2.1}$$

where $\widetilde{\mathcal{R}}(S) := \left(I(S) \otimes I_2\right)\widetilde{\mathcal{R}}$, $m_{\bar{k}}^2$ is defined as in Theorem 28,

$$\mathcal{D}_{\bar{k}(S)}\left[m_{\bar{k}}^2 I_2\right] \triangleq \left(I(S) \otimes I_2\right)\mathcal{D}_{\bar{k}}\left[m_{\bar{k}}^2 I_2\right]\left(I(S) \otimes I_2\right)^T,$$

and $\widetilde{\mathcal{R}}$ and $\mathcal{D}_{\bar{k}}\left[m_{\bar{k}}^2 I_2\right]$ are constructed from the edge set E_D.

The worst-case convergence rate to the null-space of Q is dictated by the smallest nonzero eigenvalue of Q. This also dictates the exponential convergence envelope of the dynamics. The other non-zero eigenvalues of Q also play a role in describing the convergence of the dynamics. Edge selection based on measures of these eigenvalues has the effect of improving the overall dynamics performance and is the edge optimization criterion for this section.

The first considered measure is $\mathbf{trace}\left[Q\right]$, which is proportional to the instantaneous average convergence envelope of the dynamics at time t when the initial error is $\|\mathbf{z}\left(t\right)\|$ is sampled evenly on the unit circle. This follows from the fact that for a fixed scale $S\left(\mathbf{f}\right)^{-1}$,

$$\begin{aligned}
\frac{d}{dt}\mathbb{E}_{\|\mathbf{z}(t)\|=1}V(z\left(t\right)) &\leq -S\left(\mathbf{f}\right)^{-1}\mathbb{E}_{\|\mathbf{z}(t)\|=1}\mathbf{z}^T\left(t\right)Q\mathbf{z}\left(t\right) \\
&= -S\left(\mathbf{f}\right)^{-1}\frac{1}{2n}\sum_{i=1}^{n}\lambda_i(Q)\mathbb{E}_{\|\mathbf{z}(t)\|=1}\mathbf{z}^T\left(t\right)\mathbf{z}\left(t\right) \\
&= \left(-S\left(\mathbf{f}\right)^{-1}\frac{1}{n}\mathbf{trace}\left[Q\right]\right)\mathbb{E}_{\|\mathbf{z}(t)\|=1}V(\mathbf{z}\left(t\right)).
\end{aligned}$$

Consequently, a larger $\mathbf{trace}\left[Q\right]$ will speed up the average convergence rate envelope.

An attraction of this measure is that it is modular with respect to the edge selection problem on the graph. This feature is formalized in the following proposition.

PROPOSITION 36. *Let $Q(S)$ be defined as in (6.2.1); then the set function*

$$f_t(S) = \mathbf{trace}[Q(S)] \tag{6.2.2}$$

for $S \subseteq E_D$ is modular.

PROOF. The proof follows from Theorem 34.b by letting $S_0 = \{\emptyset\}$ and

$$\begin{aligned} U(S) &= \mathcal{D}_{\bar{k}(S)}[m_{\bar{k}} I_2]\,\widetilde{\mathcal{R}}(S) \\ &= (I(S) \otimes I_2)\,\mathcal{D}_{\bar{k}}\left[m_{\bar{k}}^2 I_2\right](I(S) \otimes I_2)^T (I(S) \otimes I_2)\,\widetilde{\mathcal{R}} \\ &= (I(S) \otimes I_2)\,\mathcal{D}_{\bar{k}}\left[m_{\bar{k}}^2 I_2\right]\widetilde{\mathcal{R}} \\ &= (I(S) \otimes I_2)\,\mathcal{D}_{\bar{k}(E_D)}[m_{\bar{k}} I_2]\,\widetilde{\mathcal{R}}(E_D). \end{aligned}$$

□

A boon of the modularity of $\mathbf{trace}[Q]$ is that the greedy selection of edges under this measure provides the optimal edge selection. Interestingly, $\mathbf{trace}[Q]$ is independent of the unitless rigidity matrix $\widetilde{\mathcal{R}}(S)$. This becomes apparent by manipulating the trace of a single edge $\{s\} \in E_D$, indicating the sth row of H by $H_{\bar{s}}$; then

$$\begin{aligned} f_t(\{s\}) &= \mathbf{trace}[\widetilde{\mathcal{R}}(\{s\})^T \mathcal{D}_{\bar{k}(\{s\})}\left[m_{\bar{k}}^2 I_2\right]\widetilde{\mathcal{R}}(\{s\})] \\ &= \mathbf{trace}[(H_{\bar{s}} \otimes I_2)\mathcal{D}_{\bar{k}(\{s\})}\left[m_{\bar{k}}^2 I_2\right](H_{\bar{s}}^T \otimes I_2)] \\ &= \mathbf{trace}[m_{\bar{s}}^2(\begin{bmatrix} 1 \\ -1 \end{bmatrix} \otimes I_2) P_{\bar{s}}^2 (\begin{bmatrix} 1 & -1 \end{bmatrix} \otimes I_2)] \\ &= \mathbf{trace}[m_{\bar{s}}^2(\begin{bmatrix} 1 & -1 \end{bmatrix} \begin{bmatrix} 1 \\ -1 \end{bmatrix} \otimes I_2) P_{\bar{s}}] \\ &= \mathbf{trace}[2m_{\bar{s}}^2 P_{\bar{s}}] = 2m_{\bar{s}}^2, \end{aligned} \tag{6.2.3}$$

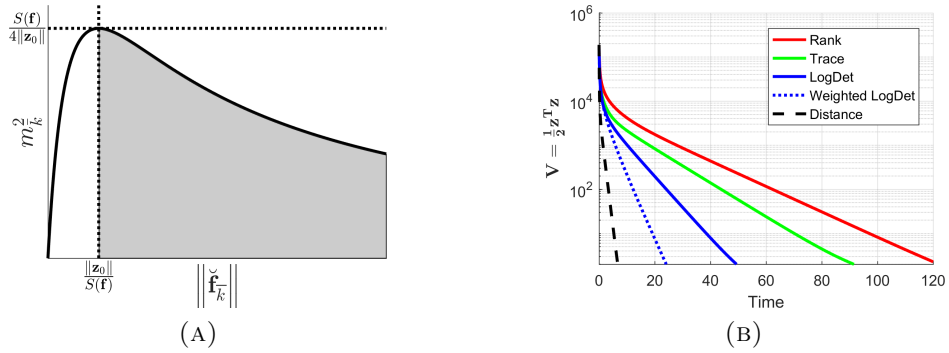

(A) (B)

FIGURE 6.2.1. A) Curve for $m_{\bar{k}}^2$ versus $\left\|\tilde{\mathbf{f}}_{\bar{k}}\right\|$ for an unweighted edge, i.e., $w_{\bar{k}} = 1$, given desired formation $\mathbf{f}$ with initial error $\mathbf{z}_0$. B) Average potential over 100 random initial conditions, where the Rank curve is the formation from Figure 6.0.1a, the Trace curve is the formation from Figure 6.0.1b, the LogDet curve is the formation from Figure 6.0.1c, and the Weighted LogDet curve is the formation from Figure 6.0.1d.

and using the property that

$$f_t(S) \quad = \quad \sum_{s \in S} f_t\left(\{s\}\right) = 2 \sum_{s \in S} m_{\bar{s}}^2,$$

as $f_t\left(S\right)$ is a modular function. The measure is therefore solely dependent on the lengths $\left\|\tilde{\mathbf{f}}_{\bar{k}}\right\|$ and weights $w_{\bar{k}}$ of the selected edges, and the initial condition $\mathbf{r}_0$. Figure 6.2.1a plots the function $m_{\bar{k}}^2$ for an unweighted edge. For the regime $\left\|\tilde{\mathbf{f}}_{\bar{k}}\right\| \geq \|\mathbf{z}_0\| \, S\left(\mathbf{f}\right)^{-1}$ for all edges $\bar{k}$, or equivalently $\|\mathbf{f}_{\bar{k}}\| \geq \|\mathbf{r}_0 - \mathbf{f}_{\mathbf{r}}\|$, where $\mathbf{f}_{\mathbf{r}} = \xi(\mathbf{r}_0, \Theta)$, then smaller $\left\|\tilde{\mathbf{f}}_{\bar{k}}\right\|$corresponds to a large $m_{\bar{k}}^2$ and therefore a larger $\mathbf{trace}\left[Q\right]$, i.e., smaller edges in the final formation shape are preferable. For the regime $\left\|\tilde{\mathbf{f}}_{\bar{k}}\right\| \leq \|\mathbf{z}_0\| \, S\left(\mathbf{f}\right)^{-1}$, the reverse is true. Examining convergence rate close to the equilibrium, namely when

$$\|\mathbf{r}_0 - \mathbf{f}\| \leq \min_{\bar{k}} \|\mathbf{f}_{\bar{k}}\|, \tag{6.2.4}$$

the optimal q-edge selection to maximize $\mathbf{trace}\left[Q\right]$ would be to select the q shortest edges $\left\|\tilde{\mathbf{f}}_{\bar{k}}\right\|$.

As $f_t(S)$ is independent of $\widetilde{\mathcal{R}}\left(S\right)$, it will not necessarily favor a maximum rank rigidity matrix which is necessary to acquire the desired formation shape. An alternative is to use

this result in conjunction with the submodular rank measure described in Proposition 35. This can be achieved by applying the additive submodular property of Proposition 13 to form the new submodular function

$$f(S) = f_r(S) + \alpha f_t(S), \tag{6.2.5}$$

where $\alpha > 0$. So as to encourage the minimal number of required edges for convergence to the desired formation associated with $f_r(S) = 2n - 3$, it may be desired to preferentially select the rigidity rank measure over the trace measure. To this end, α can be selected to ensure that $f_r(S) \in \{0, 1, 2\}$, when nonzero, dominates $f(S)$. Specifically, when $\alpha < 1/f_t(E_D)$ then as $f_t(S)$ is monotonically increasing $\alpha f_t(S) \in [0, 1)$ for all $S \subseteq E_D$. The effect of this choice results in the trace measure "breaking ties" when using the greedy selection heuristic over rank in Algorithm 2.

After sufficient edges S_R have been added to the graph such that the rigidity matrix is maximum rank, i.e.,

$$\mathbf{rank}\left[\mathcal{R}(S_R)\right] = \mathbf{rank}\left[Q(S_R)\right] = 2n - 3,$$

then to further improve performance it may be desired to add additional edges $S \in E_D \setminus S_R$. The $\mathbf{trace}\left[Q(S_R \cup S)\right]$ is one measure to accomplish this result. A limitation of this measure is that, as it is based on the average convergence, it does not favor improving the worst case convergence. The worst case convergence dictated by the smallest non-zero eigenvalue of Q, namely $\lambda_4(Q)$. The set function $f(S) = \lambda_4(Q(S_R \cup S))$ is not a submodular function, however, so does not provide greedy guarantees when Algorithm 2 is applied. An alternative measure, which promotes increasing the smallest eigenvalues of a matrix, is $\sum_{i=4}^{2n} \mathbf{log}\lambda_i(Q(S_R \cup S))$. From the discussion on the nullspace of $\mathcal{R}$ in Theorem 29, note that $\hat{\mathbf{v}}_1, \hat{\mathbf{v}}_2$ and $\hat{\mathbf{v}}_3$ span the nullspace of $Q(S_R)$ with unitary eigenvalues, i.e., $Q(S_R) + \sum_{j=1}^{3} \hat{\mathbf{v}}_j \hat{\mathbf{v}}_j^T$ is full rank and $\mathbf{log}\lambda_n(\hat{\mathbf{v}}_j \hat{\mathbf{v}}_j^T) = \mathbf{log}(1) = 0$. Hence, for $\mathbf{rank}\left[Q\left(S_R\right)\right] = 2n - 3$ it follows that

$$\sum_{i=4}^{2n} \mathbf{log}\lambda_i\left(Q\left(S_R \cup S\right)\right) \;=\; \sum_{i=4}^{2n} \mathbf{log}\lambda_i\left(Q\left(S_R \cup S\right)\right) + \sum_{j=1}^{3} \mathbf{log}\lambda_n\left(\hat{\mathbf{v}}_j \hat{\mathbf{v}}_j^T\right)$$

$$
\begin{aligned}
&= \sum_{i=1}^{2n} \mathbf{log}\lambda_i \left[Q\left(S_R \cup S\right) + \sum_{j=1}^{3} \hat{\mathbf{v}}_j \hat{\mathbf{v}}_j^T \right] \\
&= \mathbf{tracelog} \left[Q\left(S_R \cup S\right) + \sum_{j=1}^{3} \hat{\mathbf{v}}_j \hat{\mathbf{v}}_j^T \right] \ddagger \\
&= \mathbf{logdet} \left[Q\left(S_R \cup S\right) + \sum_{j=1}^{3} \hat{\mathbf{v}}_j \hat{\mathbf{v}}_j^T \right].
\end{aligned}
$$

The following proposition describes the submodularity of $\sum_{i=4}^{2n} \mathbf{log}\lambda_i\left(Q\right)$ providing the necessary features to guarantee the performance of the greedy Algorithm 2.

PROPOSITION 37. *Let $Q(S)$ be defined as in Eq. (6.2.1). The set function*

$$
f_\ell\left(S\right) = \mathbf{logdet} \left[Q\left(S_R \cup S\right) + \sum_{i=1}^{3} \hat{\mathbf{v}}_i \hat{\mathbf{v}}_i^T \right] \tag{6.2.6}
$$

and $S \subseteq E_D \setminus S_R$, where $\mathbf{rank}\left[f_\ell\left(\emptyset\right)\right] = \mathbf{rank}\left[Q(S_R)\right] = 2n-3$ is submodular.

PROOF. Following similarly to the proof of Proposition 36, then

$$
\begin{aligned}
U\left(S\right) &= \begin{bmatrix} \mathcal{D}_{\bar{k}(S_R \cup S)}\left[m_{\bar{k}} I_2\right] \widetilde{\mathcal{R}}\left(S_R \cup S\right) \\ \sum_{i=1}^{3} \hat{\mathbf{v}}_i \hat{\mathbf{v}}_i^T \end{bmatrix} \\
&= I\left(S \cup S_R \cup T\right) \otimes I_2 \begin{bmatrix} \mathcal{D}_{\bar{k}(S_R \cup E_D)}\left[m_{\bar{k}} I_2\right] \widetilde{\mathcal{R}}\left(S_R \cup E_D\right) \\ \sum_{i=1}^{3} \hat{\mathbf{v}}_i \hat{\mathbf{v}}_i^T \end{bmatrix} \\
&= \left(I\left(S \cup S_0\right) \otimes I_2\right) U\left(E_D\right),
\end{aligned}
$$

where $T = \{|E_D|+1, |E_D|+2, |E_D|+3\}$ and $S_0 = S_R \cup T$. Further as $\sum_{i=1}^{3} \hat{\mathbf{v}}_i \hat{\mathbf{v}}_i^T$ is an idempotent matrix then $U^T(S)U\left(S\right) = Q\left(S_R \cup S\right) + \sum_{i=1}^{3} \hat{\mathbf{v}}_i \hat{\mathbf{v}}_i^T$. Therefore, $U(S)$ is in the necessary form to apply Theorem 34.c and so the result follows. □

††For matrix M, $\mathbf{log}[M]$ denotes to the matrix logarithm of M.

6.3. Weight Selection

Once an edge set E has been selected to achieve infinitesimal bearing rigidity, additional performance improvement can also be garnered if edge weights $\mathbf{w}$ can be designed non-uniformly. Assuming the weights are positive continuous variables for certain selection criteria, these can be optimized using convex optimization. Examining dynamics (3.2.1b), as $\left\| \left(\hat{\mathbf{r}}_{ij}^T \hat{\mathbf{f}}_{ij}^{\perp} \right) \hat{\mathbf{r}}_{ij}^{\perp} \right\| \leq 1$, then $\left\| \mathbf{u}_{(ij)} \right\| \leq w_{ij}$ and so the edge weight w_{ij} is akin to the maximum available control effort available to correct for errors induced by the edge $\{i, j\}$. Not surprisingly, increasing edge weights has the effect of increasing the convergence rate of the dynamics. This is captured more explicitly through Corollary 30 where the worst case convergence is dictated by the smallest non-zero eigenvalue of $Q(\mathbf{w})$, namely $\lambda_4(Q(\mathbf{w}))$, and the edge weights appear linearly in the term $m_{\bar{k}}^2(w_{\bar{k}})$ within the definition of Q. Balancing the maximum control effort available at each node, defined as $u_{\max}$, and maximizing $\lambda_4(Q(w))$ then an equivalent optimization problem is:

$$\begin{aligned} &\underset{\mathbf{w}}{\text{maximize}} \ \lambda_4(Q(\mathbf{w})) \\ &\text{s.t. } w_{\bar{k}} \geq 0, \ \sum_{j \in N(i)} w_{ij} \leq u_{\max}. \end{aligned} \tag{6.3.1}$$

The control effort cap in (6.3.1) can be represented in terms of the incidence matrix of the graph as $\left| H^T \right| \mathbf{w} \leq u_{\max} \mathbf{1}$, where $|\cdot|$ for a matrix indicates the element-wise absolute value.

Applying a similar approach to Proposition 37 to remove the nullspace of Q then

$$\lambda_4(Q) = \lambda_1 \left(Q + \beta \sum_{i=1}^{3} \hat{\mathbf{v}}_i \hat{\mathbf{v}}_i^T \right). \tag{6.3.2}$$

It is assumed that β is large enough to shift the eigenvalues associated with $\sum_{i=1}^{3} \hat{\mathbf{v}}_i \hat{\mathbf{v}}_i^T$ above $\lambda_4(Q)$, i.e., $\beta \geq \lambda_4(Q)$. A sufficiently large β can be found by examining and upper bound of $\frac{1}{2n-3}\mathbf{trace}[Q]$ which is the average over the nonzero eigenvalues of Q with

$$\lambda_4(Q) \ \leq \ \frac{1}{2n-3} \sum_{i=4}^{2n} \lambda_i(Q)$$

$$
\begin{aligned}
&= \frac{1}{2n-3}\mathbf{trace}\left[Q\right] \\
&= \frac{1}{2n-3}2\sum_{\bar{k}=1}^{m} m_{\bar{k}}^2 \text{ (from equality (6.2.3))} \\
&\leq \frac{2}{2n-3}\sum_{\bar{k}=1}^{m} w_{\bar{k}}\frac{S\left(\mathbf{f}\right)}{4\left\|z_0\right\|} \text{ (from upper bound in Figure 6.2.1a)} \\
&\leq \frac{S\left(\mathbf{f}\right)}{2\left\|z_0\right\|}\frac{1}{2n-3}\frac{n}{2}u_{\max} \\
&= \frac{nu_{\max}}{4\left(2n-3\right)}\frac{S\left(\mathbf{f}\right)}{\left\|z_0\right\|} := \beta,
\end{aligned}
$$

where the final inequality follows from the maximum control cap as

$$
\begin{aligned}
\sum_{\bar{k}=1}^{m} w_{\bar{k}} &= \frac{1}{2}\sum_{i=1}^{n}\sum_{j\in N(i)} w_{ij} \\
&\leq \frac{1}{2}\sum_{i=1}^{n} u_{\max} \\
&\leq \frac{n}{2}u_{\max}.
\end{aligned}
$$

From the additive property in Eq. (6.0.1) over the edges of Q, then

$$
\begin{aligned}
Q &= \sum_{s\in E} Q\left(\{s\}\right) \\
&= \sum_{s\in E} \widetilde{\mathcal{R}}\left(\{s\}\right)^T \mathcal{D}_{\bar{k}(\{s\})}\left[m_{\bar{k}}^2 I_2\right]\widetilde{\mathcal{R}}\left(\{s\}\right) \\
&= \sum_{s\in E} w_{\bar{s}}\widetilde{\mathcal{R}}\left(\{s\}\right)^T\left[\frac{\left\|\tilde{\mathbf{f}}_{\bar{s}}\right\|}{\left(S\left(\mathbf{f}\right)^{-1}\left\|\mathbf{z}_0\right\| + \left\|\tilde{\mathbf{f}}_{\bar{s}}\right\|\right)^2} I_2\right]\widetilde{\mathcal{R}}\left(\{s\}\right) \\
&= \sum_{s\in E} w_{\bar{s}} Q_u(\{s\}),
\end{aligned}
$$

where $Q_u\left(\{s\}\right)$ is the matrix representing the unweighted contribution of edge $s \in E$. Hence, the maximization of $\lambda_4\left(Q\right)$ using (6.3.2) can be represented as a linear matrix inequality and solved as a convex optimization presented in Algorithm 3.

Algorithm 3 Algorithm to maximize $\lambda_4(Q)$ with respect to the weight vector $\mathbf{w}$ given a fixed edge set E.

$$\begin{aligned} &\underset{\mathbf{w}}{\text{maximize}} \ \delta \\ &\text{s.t.} \ \sum_{s\in E} w_{\bar{s}} Q_u(\{s\}) + \beta \sum_{i=1}^{3} \hat{\mathbf{v}}_i \hat{\mathbf{v}}_i^T \succeq \delta I, \\ &\mathbf{w} \geq \mathbf{0}, \ \left|H^T\right| \mathbf{w} \leq u_{\max} \mathbf{1} \end{aligned}$$

We note that one reasonable strategy using what we have developed is to do an initial edge selection based on the methods in §6.1 and §6.2, then apply Algorithm 3 to refine the chosen edge weights. An example of the difference can be seen in Figures 6.0.1c and 6.0.1d, with edge selections result in average convergence rates seen in Figure 6.2.1b.

This chapter built a framework for the selection of effective edges as both submodular optimization and convex optimization problems using bearing rigidity measures. A similar approach can be adopted to address the leader selection problem for dynamics. This is the subject of Chapter 7.

CHAPTER 7

Leader Selection for External Manipulation

Previously in §3.2, we studied the performance of the *forced* dynamics (3.2.1). External signals were applied from *leader* agents $V_\ell \subseteq V$ with $\tilde{\mathbf{u}}_i \neq 0$, where the selection criteria of a "favorable" leader was based on the leader's ability to translate or scale a bearing-constrained formation. The considered form of $\tilde{\mathbf{u}}_i$ was an instantaneous signal. In this section, we adapt the tools developed in the previous material to select leaders which have external signals that "ground" the formation to a certain position and scale given information from a set of anchors which behave as stationary neighbors. These *leader agents* will manipulate the formation as a whole, so we can acquire the desired formation scale and position. Taking a similar approach to Shames and Summers [**23**], we assume there are some external *anchors* that act as additional bearing constraints to any agent that can sense them. There are many examples of such signals like the VHF omni-directional range (VOR) radio navigation system used by aircraft, localizing from signals of opportunity like CDMA cellular towers [**83**], or simply letting a subset of agents have access to their position using GPS so they can measure their bearing offset from locations set *a priori*.

Let V_a be the set of n_a *anchor nodes* with corresponding positions $\mathbf{f}_a \in \mathbb{R}^{2n_a}$. Let

$$E_a(S) = \{\{i,j\} \,:\, i \in S,\, j \in V_a\}$$

be the set of edges between anchors and the leaders in set $S \subseteq V$. This set represents the possible bearing measurements a leader agent can make. In this section, we will still be selecting a subset of edges, but in contrast to previous sections, we will do so by selecting edges connected to a subset of the agents. This will result in selecting a subset of the anchor edges via selecting leaders resulting in a system which is "full rank" and exhibits "high performance".

Specifically, leaders have access to a family of n_a *anchor* reference positions. The ith anchor's position is denoted as $\mathbf{a}_i \in \mathbb{R}^2$. The graph $\mathcal{G}$ is extended to include anchor nodes V_a, or cardinality n_a, and m_a anchored edges $\{i, j\}$ with weights w_{ij} for all $i \in V_a$ and $j \in V_\ell$ with the extended neighborhood of agents V_ℓ denoted as $\mathcal{N}_a$. The agent's position vector $\mathbf{r}$ is augmented with the anchor positions with $\mathbf{r}_{n+i} = \mathbf{a}_i$ for $i = 1, \ldots, n_a$ and the desired formation $\mathbf{f}$ is similarly augmented with $\mathbf{f}_{n+i} = \mathbf{a}_i$. The leader agents forced signal is then defined using the new bearing measurements to the anchors as

$$\tilde{\mathbf{u}}_i = \sum_{j \in \mathcal{N}_a(i)} w_{ij} (\hat{\mathbf{r}}_{ij}^T \hat{\mathbf{f}}_{ij}^\perp) \hat{\mathbf{r}}_{ij}^\perp. \tag{7.0.1}$$

The attraction of this form of external leader signal is that many of the tools developed previously can be adapted to examine the *anchored* properties of these dynamics. The first notion is the anchored rigidity matrix $\mathcal{R}_a \in \mathbb{R}^{2(m+m_a)\times 2(n+n_a)}$, can be formed as $\mathcal{R}_a(\Theta) := \frac{\partial \hat{\bar{\mathbf{f}}}}{\partial \mathbf{f}}$. Noting that $\left[\frac{\partial \hat{\bar{\mathbf{f}}}}{\partial \mathbf{f}}\right]_{ij} = 0$ for $j \in V_a$, as the anchors nodes are effectively grounded, then

$$\mathcal{R}_a = \begin{bmatrix} \mathcal{R} & \mathbf{0} \\ \frac{\partial \hat{\bar{\mathbf{f}}}_a}{\partial \mathbf{f}} & \mathbf{0} \end{bmatrix}$$

where $\mathcal{R}$ is the rigidity matrix of the unanchored formation and

$$\hat{\bar{\mathbf{f}}}_a \triangleq \begin{bmatrix} \hat{\mathbf{f}}_{m+1}^T & \hat{\mathbf{f}}_{m+2}^T & \cdots & \hat{\mathbf{f}}_{m+m_a}^T \end{bmatrix}^T.$$

The anchored unitless rigidity matrix $\widetilde{\mathcal{R}}_a$ is defined similar to the unitless rigidity matrix $\widetilde{\mathcal{R}}$. Consequently, the anchors can serve as a method to remove the nullspace associated with the centroid and scale of $\mathcal{R}$. When sufficient bearing measurements are added to the dynamics, through the addition of anchors and leaders to define a unique formation $\mathbf{f}$, then the framework Θ is called *anchored infinitesimally bearing rigid*. This property manifests itself as a rank property summarized in the following theorem.

THEOREM 38. *For a framework to be anchored infinitesimally bearing rigid, we must have that*

$$\mathbf{rank}\left[\mathcal{R}_a\left(\Theta\right)\right] = 2n.$$

As the addition of an anchor grounds at most two dimensions in the null space of $\mathcal{R}$, at least two anchors are needed with associated leader agent edges for an infinitesimally bearing rigid framework to become an anchored infinitesimally bearing rigid framework. Not surprisingly, for an anchored infinitesimally bearing rigid formation, the dynamics will converge exponentially to the unique formation $\mathbf{f}$. The proof of this property echoes that of Theorem 28 using Theorem 38. The result is summarized in the following without proof, leveraging the property $\mathbf{rank}\left[\mathcal{R}_a\right] = 2n$ to show that the dynamics converge to a unique $\mathbf{f}$, rather than a formation dependent on the initial conditions as in Corollary 30.

THEOREM 39. *Let the framework $\Theta\left(\mathcal{G}, \mathbf{f}\right)$ be anchored infinitesimally bearing rigid. Under the forced dynamics (3.2.1) with $\tilde{\mathbf{u}}_i$ from Eq. (7.0.1), a Lyapunov function is $V = \frac{1}{2}\mathbf{z}^T\mathbf{z}$, where $\mathbf{z} = \mathbf{r} - \mathbf{f}$, with associated Lyapunov rate bounded as*

$$\begin{aligned} \dot{V} &\leq S\left(\mathbf{f}\right)^{-1}\mathbf{z}^T\widetilde{\mathcal{R}}_a^T\mathcal{D}_{\bar{k}}\left[m_{\bar{k}}^2 I_2\right]\widetilde{\mathcal{R}}_a\mathbf{z} \\ &\triangleq -S\left(\mathbf{f}\right)^{-1}\mathbf{z}^T Q_a\mathbf{z}, \end{aligned}$$

where $m_{\bar{k}}^2(\mathbf{r}_0)$ is as defined in Theorem 28. Consequently, $\mathbf{r}\left(t\right)$ will globally exponentially converge to $\mathbf{f}$.

7.1. Selection for Anchor Rigidity

As for the unforced dynamics, it is important to reason about effective graph topologies that meet the requirements for convergence and improve the overall performance of the forced dynamics (3.2.1). The ability to adapt the graph topologies in the forced dynamics is assumed to be restricted to the selection of a set of leader agents given at least $n_a \geq 2$ anchors. The topology selection problem is then a node selection rather than an edge selection problem.

With the objective of selecting a set of leader agents $S \subseteq V \setminus V_a$ to acquire the infinitesimally bearing rigid framework necessary for the convergence of the dynamics, the anchored rigidity matrix is

$$\mathcal{R}_a(S) = \begin{bmatrix} \mathcal{R} & \mathbf{0} \\ \frac{\partial \hat{\bar{\mathbf{f}}}_a(S)}{\partial \mathbf{f}} & \mathbf{0} \end{bmatrix}$$

where $\hat{\bar{\mathbf{f}}}_a(S) = \left\{\hat{\mathbf{f}}_{ij}\right\}$ where $i \in S$ and $j \in V_a$. Unlike the edge selection rigidity matrix problem, $2n_a$ rows are added to $\mathcal{R}_a$ for each leader selected. The matrix-valued set function $\widetilde{\mathcal{R}}_a(S)$ is defined similarly.

The following proposition establishes that the rank set function for $\mathcal{R}_a$ is submodular. Hence, the leader agents can be selected using greedy Algorithm 2 until $\mathcal{R}_a$ has rank $2n$ with the suboptimality guarantees of Theorem 14.

PROPOSITION 40. *The set function*

$$f_r(S) = \mathbf{rank}\left[\mathcal{R}_a(S)\right] \tag{7.1.1}$$

for $S \subseteq V \setminus V_a$ is submodular.

PROOF. This result follows directly from Theorem 34.a by letting

$$S_0 = \{1, 2, \ldots, 2m-1, 2m\}$$

and

$$\begin{aligned} U(S) &= \mathcal{R}_a(S) \\ &= \left(I(S \cup S_0) \otimes I_{2n_a}\right) \mathcal{R}_a(V \setminus V_a), \end{aligned}$$

where for $V \setminus V_a = \{v_1, v_2, \ldots, v_n\}$ then

$$\hat{\bar{\mathbf{f}}}_a(V \setminus V_a) = \left[\begin{array}{cccc} \hat{\bar{\mathbf{f}}}_a(\{v_1\})^T & \hat{\bar{\mathbf{f}}}_a(\{v_2\})^T & \cdots & \hat{\bar{\mathbf{f}}}_a(\{v_n\})^T \end{array}\right]^T.$$

□

7.2. Selection for Convergence

We now consider the selection of leaders under measures that promote the convergence rate of the dynamics. The matrix Q_a which appears in the Lyapunov function of Theorem 39 can be written with respect to the leader set $S \subseteq V \setminus V_a$ as

$$Q_a(S) = \widetilde{\mathcal{R}}_a(S)^T \begin{bmatrix} \mathcal{D}_{\bar{k}}\left[m_{\bar{k}}^2 I_2\right] & 0 \\ 0 & \mathcal{D}_{\bar{k}_a(S)}\left[m_{\bar{k}}^2 I_2\right] \end{bmatrix} \widetilde{\mathcal{R}}_a(S), \tag{7.2.1}$$

where $\mathcal{D}_{\bar{k}}\left[m_{\bar{k}}^2 I_2\right]$ is constructed from the edges between agents in $V \setminus V_a$,

$$\mathcal{D}_{\bar{k}_a(S)}\left[m_{\bar{k}}^2 I_2\right] \triangleq \left(I(S) \otimes I_{2n_a}\right) \mathcal{D}_{\bar{k}_a}\left[m_{\bar{k}}^2 I_2\right] \left(I(S) \otimes I_{2n_a}\right)^T,$$

and $\mathcal{D}_{\bar{k}_a}\left[m_{\bar{k}}^2 I_2\right]$ is constructed from the edges between the agent set $V \setminus V_a$ and the anchors V_a. Following a similar approach to §6.2, $\mathbf{trace}\left[Q_a(S)\right]$ is a modular function and the log of the determinant of a nullspace-removed $Q_a(S)$ is a submodular function with respect to the leader set S. This feature is summarized in the following two propositions. The proofs of these propositions are omitted due to their similarities to Propositions 36 and 37.

PROPOSITION 41. *Let $Q_a(S)$ be defined as in Eq. (7.2.1). The set function*

$$f_t(S) = \mathbf{trace}\left[Q_a(S)\right] \tag{7.2.2}$$

for $S \subseteq V \setminus V_a$ is modular.

PROPOSITION 42. *Let $Q_a(S)$ be defined as in (7.2.1). The set function*

$$f_\ell(S) = \mathbf{logdet}\left[Q_a(S_R \cup S) + \begin{bmatrix} \mathbf{0}_{2n \times 2n} & \mathbf{0}_{2n \times 2n_s} \\ \mathbf{0}_{2n_s \times 2n} & I_{2n_a} \end{bmatrix}\right], \tag{7.2.3}$$

where $S \subseteq V \setminus (V_a \cup S_R)$ and

$$\mathbf{rank}\left[f_\ell(\emptyset)\right] = \mathbf{rank}\left[Q_a(S_R)\right] = 2n,$$

is submodular.

As per §6.2, the greedy Algorithm 2 can be applied to the set function (7.2.2) to select leaders that improve the convergence performance even when then the framework is not anchored infinitesimally bearing rigid. The logdet measure is applicable as a selection criteria once S_R leaders are selected which are sufficient to establish anchored infinitesimal bearing rigidity with $\mathbf{rank}\left[Q_a(S_R)\right] = 2n$. Additionally, positive linear combinations of the set functions (7.1.1), (7.2.2) and (7.2.3) are also submodular functions by Proposition 13. The suboptimality guarantees of Theorem 14 would then apply to the greedy selection process.

7.3. Weight Selection

The edge weights $\mathbf{w}$ composed of the m initial edges and m_a anchored edges can be optimized similarly to §6.3. In the anchored case, the worst case convergence rate is dictated by the smallest nonzero eigenvalue of Q_a, namely $\lambda_{2n_a+1}(Q_a)$. Examining a reduced form of the anchored rigidity matrix defined as

$$\mathcal{R}_{ra} = \begin{bmatrix} \mathcal{R} \\ \frac{\partial \hat{\bar{\mathbf{f}}}_a(S)}{\partial \mathbf{f}} \end{bmatrix},$$

with the associated reduced unitless anchored rigidity matrix $\widetilde{\mathcal{R}}_{ra}$, then for

$$Q_{ra} \triangleq \widetilde{\mathcal{R}}_{ra}^T \mathcal{D}_{\bar{k}} \left[m_{\bar{k}}^2 I_2\right] \widetilde{\mathcal{R}}_{ra} \in \mathbb{R}^{2n \times 2n},$$

we have,

$$\lambda_{2n_a+1}(Q_a) = \lambda_1(Q_{ra}).$$

This follows from the removal of the nullspace of Q_a through the reduced anchored rigidity matrix. The dependence of Q_{ra} on $\mathbf{w}$ can be explicitly represented as

$$Q_{ra} = \sum_{s \in E} w_{\bar{s}} Q_{rau}(\{s\}),$$

where the matrix $Q_{au}(\{s\})$ represents the unweighted contribution of edge $s \in E$ to Q_{ra}. Subsequently, the maximization of $\lambda_{2n_a+1}(Q_a)$ can be represented as a linear matrix inequality (LMI) as shown in Eq. (7.3.1a).

Algorithm 4 Algorithm to maximize $\lambda_{2n_a+1}(Q_a)$ with respect to the weight vector $\mathbf{w}$ given a fixed edge set E.

$$\begin{aligned}
&\underset{\mathbf{w}}{\text{maximize}} && \delta \\
&\text{s.t.} && \sum_{s\in E} w_{\bar{s}} Q_{rau}(\{s\}) \succeq \delta I, && \text{(7.3.1a)} \\
& && \mathbf{w} \geq \mathbf{0},\ I(V\setminus V_a)^T \left|H^T\right| \mathbf{w} \leq u_{\max}\mathbf{1}, && \text{(7.3.1b)} \\
& && I(V_\ell)^T \left|H_a^T\right| \mathbf{w}_a \leq \beta u_{\max}\mathbf{1} && \text{(7.3.1c)}
\end{aligned}$$

The maximum control effort $u_{\max}$ of each agent in $V \setminus V_a$ can be distributed across the positive weights $\mathbf{w}$ through the inequalities in Eq. (7.3.1b). It is often desirable to explicitly encode the control effort limit devoted to the anchor edges $\mathbf{w}_a$ by the leader set V_ℓ. This flexibility can help avoid formation trajectories that are dominated by the anchor edges. In this direction, one approach is to upper bound the anchor edges weights contribution as $\sum_{j\in\mathcal{N}_a(i)} w_{ij} \leq \beta u_{\max}$ for $i \in V_\ell$ and $\beta \in (0,1]$. To this end, denoting the submatrix of the incidence matrix corresponding to anchor edges as H_a, the anchor edge weight bound is equivalent to (7.3.1c). For $\beta = 1$, the anchor weight bound is inactive and anchor edges are constrained in the same fashion as the other edges in the network through inequalities (7.3.1b).

An attraction of the unforced dynamics (3.2.1) is if small external signals are applied through $\tilde{\mathbf{u}}_i$ in (3.2.1a) then the formation dynamically maintains its shape as it converges to a new translated and scaled formation [**7**]. A challenge with the external controls signal adopted in Eq. (7.0.1) is that the effect of the anchor edges can represent a large external signal that dramatically warps the formation shape. This can be mitigated though an edge weight design that limits the maximum control effort due to anchor edges. Inequality (7.3.1c), when β is close to 0, has this desired effect. The drawback from this approach is that it can induce a slower convergence to the desired formation. An alternative, which is a marriage of fast convergence and small external signals in the face of a warped formation shape, is to replace the static weight w_{ij} on the anchor edges with a state-dependent edge weight $\overline{w}_{ij}$. The weight $\overline{w}_{ij}$ would ideally be small when the formation is "warped" and large otherwise. A

local measure of the alignment of the formation is the error $\|\mathbf{u}_i\|$. A proposed *state dependent* anchor weight $\overline{w}_{ij}(\|\mathbf{u}_i\|)$ for $j \in \mathcal{N}_a(i)$ where $i \in V_\ell$ is

$$\bar{w}_{ij}(\|\mathbf{u}_i\|) = \frac{I(\{i\})^T \left|H^T\right| \mathbf{w} - \|\mathbf{u}_i\|}{I(\{i\})^T \left|H_a^T\right| \mathbf{w}_a} w_{ij}.$$

Here, $I(\{i\})^T \left|H^T\right| \mathbf{w}$ and $I(\{i\})^T \left|H_a^T\right| \mathbf{w}_a$ corresponds to the maximum available control effort available to agent i and to the anchor edges, respectively. As the formation becomes well aligned, $\|\mathbf{u}_i\|$ decreases and $\overline{w}_{ij}$ increases. Similarly, as the formation locally starts to warp the external signal supplied through the anchor edges is reduced. It should be noted that as

$$\|\mathbf{u}_i\| \leq I(\{i\})^T \left|H^T\right| \mathbf{w} - I(\{i\})^T \left|H_a^T\right| \mathbf{w}_a$$

then $\overline{w}_{ij} \geq w_{ij}$. This positive weight is required for the convergence properties of Theorem (39) to be applicable. Further, the maximum control effort of $u_{\max}$ is preserved in this case as

$$\begin{aligned}
\|\mathbf{u}_i + \tilde{\mathbf{u}}_i\| &\leq \|\mathbf{u}_i\| + \|\tilde{\mathbf{u}}_i\| \text{ (from the triangle inequality)} \\
&\leq \sum_{j \in N(i)} w_{ij} + \sum_{j \in N_a(i)} \overline{w}_{ij}(\|\mathbf{u}_i\|) \text{ (as } \left\| \left(\hat{\mathbf{r}}_{ij}^T \hat{\mathbf{f}}_{ij}^\perp \right) \hat{\mathbf{r}}_{ij}^\perp \right\| \leq 1) \\
&\leq \sum_{j \in N(i)} w_{ij} + \sum_{j \in N_a(i)} \frac{I(\{i\})^T \left|H^T\right| \mathbf{w} - \|\mathbf{u}_i\|}{I(\{i\})^T \left|H_a^T\right| \mathbf{w}_a} w_{ij} \\
&= \|\mathbf{u}_i\| + \frac{I(\{i\})^T \left|H^T\right| \mathbf{w} - \|\mathbf{u}_i\|}{I(\{i\})^T \left|H_a^T\right| \mathbf{w}_a} \sum_{j \in N_a(i)} w_{ij} \\
&\leq \|\mathbf{u}_i\| + I(\{i\})^T \left|H^T\right| \mathbf{w} - \|\mathbf{u}_i\| \leq u_{\max}.
\end{aligned}$$

Bearing rigidity is a critical property when examining the bearing-compass dynamics, establishing necessary features for the dynamics to convergence to a rigidity formation. In Chapters 6 and 7, measures on the bearing rigidity matrix were leveraged to provide methods to select favorable edges and leaders for bearing formation control. The examination of bearing rigidity and its connection to the convergence of the bearing-compass dynamics can

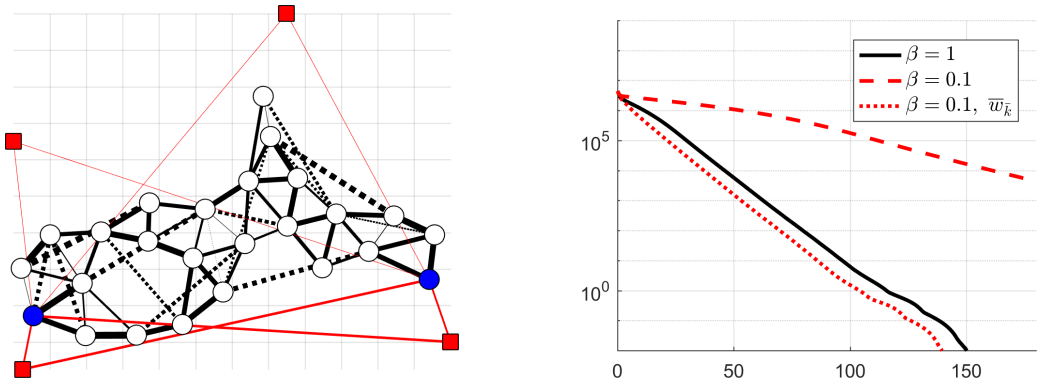

(A) (B)

FIGURE 7.3.1. A) Weighted anchor selection using the log det function $f_\ell(S)$ and B) convergence rates for aggressive anchor weights ($\beta = 1$), conservative anchor weights ($\beta = 0.1$) and state-dependent conservative anchor weights ($\beta = 0.1$, $\overline{w}_{\bar{k}}$).

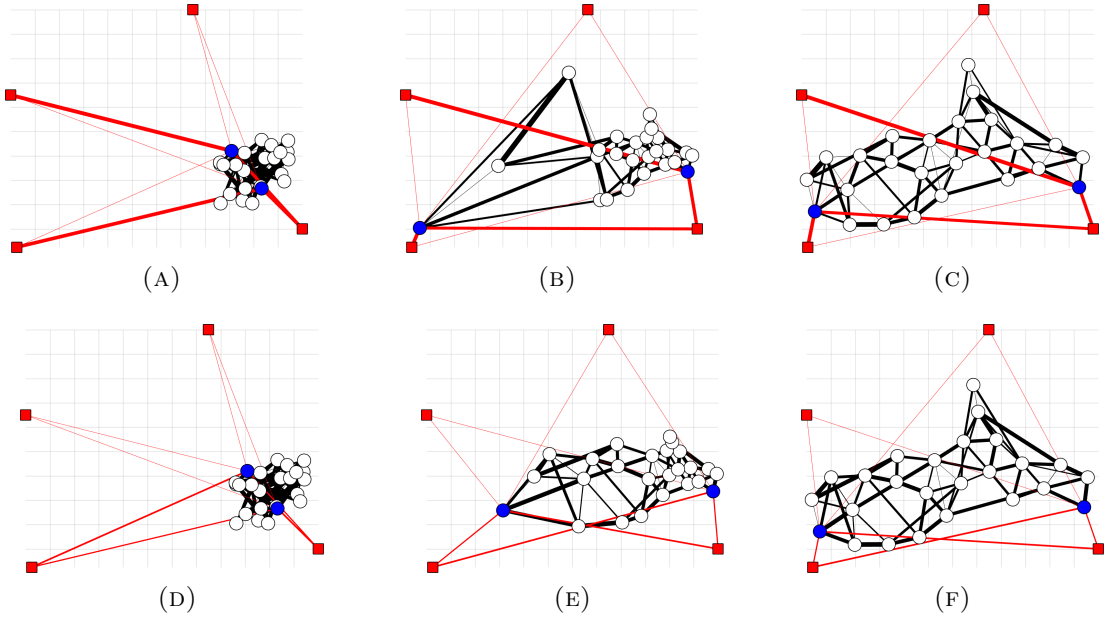

(A) (B) (C)

(D) (E) (F)

FIGURE 7.3.2. A-C) Trajectories for $\beta = 1$ and D-F) trajectories for $\beta = 0.1$ with state-dependent weighting. Anchor nodes are represented by a filled square. Note how (B) is highly distorted compared to (E).

be generalized to measurement types other than bearing measurements. This *generalized rigidity* approach is examined in the next chapter.

CHAPTER 8

Generalizing Rigidity

Establishing rigidity in bearing formation problems is necessary for establishing a unique local solution in the bearing-compass dynamics. The bearing rigidity matrix appears explicitly in the dynamics and the convergence analysis of the bearing-compass dynamics, and examining its rank provides a simple check for rigidity. In this chapter we generalize the notion of rigidity for more general relative measurements. Furthermore, inscribing a generalized rigidity matrix dynamics into a distributed protocol is shown to provide a corresponding unique state-dependent formation dynamics.

8.1. Information Content of Relative Measurements

Core to this chapter, is understanding agents formation shape when a family of measurement constraints on $\bar{\boldsymbol{r}}$ defined over the edges of the graph $\mathcal{G}$ are placed on pairs of agents.

8.1.1. Measurements on Graphs. These measurements can guide whether the agent states have acquired a desired formation $\mathbf{f} \in \mathbb{R}^{dn}$. A *framework* is defined by the graph and agent state pair as $(\mathcal{G}, \mathbf{r})$. A continuous scalar measurement function $g(\mathbf{r}_{\bar{k}}) : \mathbb{R}^d \to \mathbb{R}$ then induces on the framework $(\mathcal{G}, \mathbf{r})$, via the edge state $\overline{\mathbf{r}}$, the edge measurement function $v_g(\overline{\mathbf{r}}) : \mathrm{Im}\left(\widetilde{H}\right) \to \mathbb{R}^m$ with

$$v_g\left(\overline{\mathbf{r}}\right) = \left[g(\mathbf{r}_{\bar{1}}),\, g(\mathbf{r}_{\bar{2}}),\, \ldots,\, g(\mathbf{r}_{\bar{m}})\right]^T.$$

An indication if $\mathbf{r}$ is similar (or congruent) to a formation $\mathbf{f}$ is if $v_g\left(\overline{\mathbf{r}}\right) = v_g\left(\overline{\mathbf{f}}\right)$ defined over the frameworks $(\mathcal{G}, \mathbf{r})$ and $(\mathcal{G}, \mathbf{f})$. The concept of rigidity describes this notion of similarity and will be discussed further in §8.1.2.

A common example of a scalar measurement is the distance squared edge length $g_D(\mathbf{r}_{\bar{k}}) = \frac{1}{2}\left\|\mathbf{r}_{\bar{k}}\right\|^2$, and is a well-examined measurement type for multi-vehicle formation applications.

One method to acquire such a measurement is using a range-finder mounted on each robot pointed with measurements acquired by directing the sensor to neighboring agent in the graph. In this way, the graph $\mathcal{G}$ can be considered a sensor graph, realized through local relative measurements. Other measurement techniques to measure $g_D(\mathbf{r}_{\bar{k}})$ are time of flight signals between agents when $\mathcal{G}$ is a communication graph and on-board cameras in conjunction with knowledge of the neighboring agent's scale. Distance measurements and other relative measurements defined in Table 1 are commonly examined measurement forms. A generalized approach covering any continuous scalar measurement $g(\cdot)$ is one of the insights of this research.

An additional novelty of this work is the examination of *multiple* measurement types *concurrently* acquired by the agents. To this end, for each of the scalar measurement types $g_i(\cdot)$ forms a measurement function $v_{g_i}(\overline{\mathbf{r}}_i)$ over its framework $(\mathcal{G}_i, \mathbf{r})$ with incidence matrix of $\mathcal{G}_i$ forming the edge state vector $\overline{\mathbf{r}}_i = \widetilde{H}_i\mathbf{r}$. For each of the p measurement types, the sensor graphs $\mathcal{G}_1, \mathcal{G}_2, \cdots, \mathcal{G}_p$ each share a common vertex set V but different edge sets $E_1, E_2, \cdots, E_p$ and cardinalities $m_1, m_2, \ldots, m_p$. A composite graph is denoted $\mathcal{G} = (V, \bigcup E_i)$, which is short-hand for $\mathcal{G} = \bigcup_{i=1}^{p} \mathcal{G}_i$ where edges in $\mathcal{G}$ can appear repeatedly. The composite sensor graph can be represented as a layered graph with each layer associated with a different measurement. A corresponding composite incidence matrix $H = \left[H_1^T, H_2^T, \cdots, H_p^T\right]^T$ with $\widetilde{H} = H \otimes I_d$ can be used to from the image space of a *composite* edge measurement function $v_g(\overline{\mathbf{r}}) : \mathrm{Im}\left(\widetilde{H}\right) \to \mathbb{R}^{\sum m_i}$ where

$$v_g(\overline{\mathbf{r}}) = \left[v_{g_1}(\overline{\mathbf{r}}_1)^T, v_{g_2}(\overline{\mathbf{r}}_2)^T, \cdots, v_{g_p}(\overline{\mathbf{r}}_p)^T\right]^T.$$

The congruency of $\mathbf{r}$ and $\mathbf{f}$ is then measured over the composite edge function with $v_{g_i}(\overline{\mathbf{r}}) = v_{g_i}(\overline{\mathbf{f}})$ for all measurements i, or equivalently $v_g(\overline{\mathbf{r}}) = v_g(\overline{\mathbf{f}})$ [**38**].

A simple example that fits into the multiple measurement type setup is absolute relative measurements, i.e., $\mathbf{r}_{\bar{k}}$ is supplied directly to each neighboring pair of edges E_1 in the graph. A practical situation for a robotic swarm is when agents equipped with GPS exchange their location with neighbors in a communication graph $\mathcal{G}_1 = (V, E_1)$. The scalar measurements

Name	$g(\cdot)$	$\frac{dg}{d\mathbf{r}_{\bar{k}}}$	$\max \operatorname{rank}(\mathcal{R}_g)$
Relative position in along e_i, $g_r(\cdot)$	$e_i^T \mathbf{r}_{\bar{k}}$	e_i	$n-1$
Distance, $g_D(\cdot)$	$\frac{1}{2}\left\|\mathbf{r}_{\bar{k}}\right\|^2$	$\mathbf{r}_{\bar{k}}$	$dn - d(d+1)/2$
Bearing along e_i for $d \geq 2$, $g_{Bi}(\cdot)$	$e_i^T \hat{\mathbf{r}}_{\bar{k}}$	$\frac{1}{\|\mathbf{r}_{\bar{k}}\|}(I_d - \hat{\mathbf{r}}_{\bar{k}}\hat{\mathbf{r}}_{\bar{k}}^T)e_i$	$n-2$
Kuramoto phase for $d=1$, $g_K(\cdot)$	$\sin(e_i^T \mathbf{r}_{\bar{k}})$	$\cos(e_i^T \mathbf{r}_{\bar{k}})e_i$	$n-1$

TABLE 1. Sample of common measurement types.

would then be $g_i(\mathbf{r}_{\bar{k}}) = e_i^T \mathbf{r}_{\bar{k}}$ for $i = 1, 2, \ldots, d$ over the edges in E_1 such that $\mathcal{G}_1 = \mathcal{G}_2 = \cdots = \mathcal{G}_d$. When the layers of the composite sensor graph $\mathcal{G}$ are identical then a vector measurement $g(\cdot) = [g_1(\cdot), g_2(\cdot), \cdots, g_p(\cdot)]$ can be more compactly represented without the redundancy of $\mathcal{G}_i$'s. The strength of this formulation lies in its ability to capture the heterogeneity in the sensor layers when $\mathcal{G}_i$'s are distinct.

EXAMPLE 43. Consider the case where agents are moving in 2D, i.e., $d = 2$, and are equipped with an on-board camera. Then, as previously discussed, for agents that are close enough to resolve their scale a measurement $g_1(\mathbf{r}_{\bar{k}}) := g_D(\mathbf{r}_{\bar{k}})$ can be acquired forming an underlying sensor graph $\mathcal{G}_1$. If, in addition, agents are equipped with a compass, then the camera can be used to acquire the bearing of neighboring agents against north, specifically $\hat{\mathbf{r}}_{\bar{k}} \in \mathbb{R}^2$. As bearing resolution requires less camera resolution, the bearing sensor graph $\mathcal{G}_B$ will be larger than $\mathcal{G}_1$. The scalar measurements for bearings are then $g_2(\mathbf{r}_{\bar{k}}) = e_1^T \hat{\mathbf{r}}_k$ and $g_3(\mathbf{r}_{\bar{k}}) = e_2^T \hat{\mathbf{r}}_k$ with sensor graphs $\mathcal{G}_2 = \mathcal{G}_3 = \mathcal{G}_B$.

Example 43 can not be represented in terms of a vector measurement framework and supports the more versatile notation presented here.

8.1.2. Graph Rigidity. Rigidity theory was developed around the examination of the distance edge measurement function $v_D\overline{\mathbf{r}}$ which describes a subset of inter-agent distances within a graph. Rigidity is a property on the framework $(\mathcal{G}, \mathbf{r})$ and examines the set of all frameworks $(\mathcal{G}, \mathbf{p})$ which share the same edge function $v_D(\overline{\mathbf{r}})$. The set of frameworks $(\mathcal{G}, \mathbf{p})$ are referred to as *similar* or *congruent* to $(\mathcal{G}, \mathbf{r})$ and the set of $\mathbf{p}$ are called *target formations* [**84**]. If adding edges to $\mathcal{G}$ does not reduce the set of congruent frameworks then $(\mathcal{G}, \mathbf{r})$ is referred to as *globally rigid*. The motivation for the examination of rigidity is

to explore the information content of the family of distance constraints $v_D(\overline{\mathbf{r}}) = \mathbf{d}$, where $\mathbf{d}$ is assumed *constraint consistent* [**85**], meaning that the set $v_D^{-1}(\mathbf{d})$ is non-empty. The smaller $v_D^{-1}(v_D(\overline{\mathbf{r}}))$ the more information is contained in the measurement function. This is attractive if a particular target formation $\mathbf{f}$ is desired. For the case when $d = 2$ and $(\mathcal{G}, \mathbf{f})$ is globally rigid, for almost all $\mathbf{f}$ the set of target formations of $(\mathcal{G}, \mathbf{f})$ is a translated and rotated versions of $\mathbf{f}$.

The definition of distance rigidity can be easily adapted to other forms of measurement rigidity. Parallel rigidity is one such extension using bearing measurements and the edge measurement function $v_B(\overline{\mathbf{r}}) = \left[v_{B_1}(\overline{\mathbf{r}})^T, v_{B_2}(\overline{\mathbf{r}})^T, \cdots, v_{B_d}(\overline{\mathbf{r}})^T\right]^T$ with the sensor graph $\mathcal{G}_1 = \mathcal{G}_2 = \cdots = \mathcal{G}_d$ in common. For the case of $d = 2$ for $(\mathcal{G}, \mathbf{f})$ globally parallel rigid, for almost all $\mathbf{f}$ the set of target formation is a translated and scaled versions of $\mathbf{f}$. We introduce a generalization of global rigidity to multiple measurement types adapted from the distance rigidity definition introduced by Asimow and Roth [**86**]. The definitions are given in terms of the composite complete graph of the graph $\mathcal{G} = \bigcup_{i=1}^{p} \mathcal{G}_i$ defined as $\mathcal{K}_{\mathcal{G}} = \bigcup_{i=1}^{p} \mathcal{K}$ where $\mathcal{K}$ is the complete graph over the common sets of the graphs $\mathcal{G}_i$.

Definition 44. A framework $(\mathcal{G}, \mathbf{r})$ with edge measurement function $v_g(\overline{\mathbf{r}})$ is *globally g-rigid* if $v_g^{-1}(v_g(\overline{\mathbf{r}})) = w_g^{-1}(w_g(\overline{\mathbf{r}}))$, where $w_g(\overline{\mathbf{r}})$ is the edge measurement function on the framework $(\mathcal{K}_{\mathcal{G}}, \mathbf{r})$.

For the framework $(\mathcal{G}, \mathbf{r})$, often only target formations that are close to $\mathbf{r}$ are of concern, as these represent perturbations from $\mathbf{r}$ that share the same $v_D(\overline{\mathbf{r}})$. With this in mind, the notion of local rigidity, or just rigidity, has been examined with regard to the information contained in the measurement function within some region around $\mathbf{r}$. Similar to global rigidity we generalize this definition to multiple measurements.

Definition 45. A framework $(\mathcal{G}, \mathbf{r})$ with edge measurement function $v_g(\overline{\mathbf{r}})$ is *(locally) g-rigid* if there exists a neighborhood $\mathcal{U} \subseteq \mathbb{R}^{dn}$ of $\mathbf{r}$ such that $v_g^{-1}(v_g(\overline{\mathbf{r}})) \cap \mathcal{U} = w_g^{-1}(w_g(\overline{\mathbf{r}})) \cap \mathcal{U}$, where $w_g(\overline{\mathbf{r}})$ is the edge measurement function on the framework $(\mathcal{K}_{\mathcal{G}}, \mathbf{r})$.

Though the definitions of global and local rigidity are intuitive they can be difficult to validate. Fortunately, for a sub-class of locally rigid frameworks, a linearized version of rigidity, can be formulated which provides a simple rank check for local rigidity. This subclass is referred to as infinitesimally rigid frameworks. It is defined by examining infinitesimal motions $\delta\mathbf{r}$ applied $\mathbf{r}$ in the framework $(\mathcal{G}, \mathbf{r})$. Examining the Taylor expansion of the edge measurement function $v_g\left(\widetilde{H}\mathbf{r}\right)$ for the framework $(\mathcal{G}, \mathbf{r})$,

Examining the Taylor expansion

$$\begin{aligned} v_g\left(\widetilde{H}\left(\mathbf{r}+\delta\mathbf{r}\right)\right) &= v_g\left(\widetilde{H}\mathbf{r}\right)+\frac{\partial v_g}{\partial \mathbf{r}}\left(\widetilde{H}\mathbf{r}\right)\left(\delta\mathbf{r}\right)+\cdots+v_g\left(\mathbf{r}+\delta\mathbf{r}\right) \\ &= v_g\left(\mathbf{r}\right)+\frac{\partial v_g}{\partial \mathbf{r}}\left(\mathbf{r}\right)\delta\mathbf{r}+\frac{1}{2}\frac{\partial^2 v_g}{\partial \mathbf{r}^2}\left(\mathbf{r}\right)\delta\mathbf{r}^2+\cdots. \end{aligned}$$

Up to first order, if $\delta\mathbf{r}$ lies in the right null space of $\frac{\partial v_g}{\partial \mathbf{r}}\left(\overline{\mathbf{r}}\right)$ then the infinitesimally motion $\delta\mathbf{r}$ is undetectable through the function $v_g(\mathbf{r})$. Consequently, the matrix $\frac{\partial v_g}{\partial \mathbf{r}}$, i.e., the Jacobian of $v_g\left(\widetilde{H}\mathbf{r}\right)$, describes $v_g^{-1}\left(v_g\left(\overline{\mathbf{r}}\right)\right)$ in a neighborhood of $\overline{\mathbf{r}}$ connecting the null space of Jacobian to the definition of local rigidity. The importance of the Jacobian to rigidity theory has lead to it being called the *g-rigidity matrix* of the framework of $(\mathcal{G}, \boldsymbol{r})$ and denoted as

$$\begin{aligned} \mathcal{R}_g\left(\overline{\mathbf{r}}\right) &\triangleq \frac{\partial v_g}{\partial \mathbf{r}}\left(\overline{\mathbf{r}}\right) \\ &= \frac{\partial v_g}{\partial \overline{\mathbf{r}}}\left(\overline{\mathbf{r}}\right)\widetilde{H}. \end{aligned}$$

For a small neighborhood $\mathcal{U}$ of $\mathbf{r}$, the intuition is that the smaller the dimension of the null space of $\mathcal{R}_g\left(\overline{\mathbf{r}}\right)$ then the smaller the set $v_g^{-1}\left(v_g\left(\overline{\mathbf{r}}\right)\right)\cap\mathcal{U}$. Important to formalizing this notion is to connect the g-rigidity matrix to g-rigidity and examine the points in $\mathbb{R}^{dn}$ where the null space of $\mathcal{R}_g\left(\overline{\mathbf{r}}\right)$ is smallest.

DEFINITION 46. A point $\mathbf{r}\in\mathbb{R}^{dn}$ is a g-regular point of the graph $\mathcal{G}$ if

$$\text{rank}\mathcal{R}_g(\widetilde{H}\mathbf{r}) = \max\left\{\text{rank}\mathcal{R}_g(\widetilde{H}\mathbf{p}) \,:\, \mathbf{p}\in\mathbb{R}^{dn}\right\}.$$

Regular points are an important tool when examining the inverse map $v_g^{-1}(v_g(\bar{\mathbf{r}}))$. A result which aided in establishing rigidity is summarized in the following Proposition. Due to its similarity to [**86**, Prop. 2], the proof is only outlined.

PROPOSITION 47. *Let* $k = \max\left\{\mathbf{rank}\mathcal{R}_g(\widetilde{H}\mathbf{p}) \,:\, \mathbf{p} \in \mathbb{R}^{dn}\right\}$. *If* $\mathbf{r} \in \mathbb{R}^{dn}$ *is a g-regular point of the graph* $\mathcal{G}$, *then* $Im[v_g]$ *in some neighborhood of* $\mathbf{r}$ *is a k-dimensional manifold. Hence,* $v_g^{-1}(v_g(\bar{\mathbf{r}})) \cap \mathcal{U}$ *is a manifold of dimension* $dn - k$ *in some neighborhood* $\mathcal{U}$ *of* $\mathbf{r}$.

PROOF. The result relies on the reordering of the measurement vector as $v_g = \left\{v_g^1, v_g^2\right\}$ with $v_g^1 \in \mathbb{R}^k$ and $\text{rank}\frac{\partial v_g^1}{\partial \mathbf{r}}(\bar{\mathbf{r}}) = k$ and $v_g^2 = g\left(v_g^1\right)$ near $\mathbf{r}$ for some mapping g. The Inverse Function Theorem is then applied to v_g^1 in the neighborhood of the point $\mathbf{r}$ implying a k-dimensional manifold for $\text{Im}[v_g]$ near $\mathbf{p}$. Hence, the inverse map $v_g^{-1}(v_g(\bar{\mathbf{r}}))$ in some neighborhood of $\mathbf{r}$ has co-dimension k and so is a manifold of dimension $dn - k$. □

Regular points represent the smallest null space of $\mathcal{R}_g\left(\widetilde{H}\mathbf{r}\right)$ over all $\mathbf{r}$. Within this set of regular points lies those that induce the smallest null space over all graphs on the same number of vertices. Since the null space of $\mathcal{R}_g(\bar{\mathbf{r}})$ decreases as edges are added to a graph, then $\mathcal{K}_\mathcal{G}$ contains the edges of all other graphs, and the smallest null space of the rigidity matrix is the g-regular points of the graph $\mathcal{K}_\mathcal{G}$. If a framework shares this smallest null it is referred to as infinitesimally g-rigid and is formally defined below.

DEFINITION 48. A framework $(\mathcal{G}, \mathbf{r})$ is *infinitesimally g-rigid* if

$$\text{rank}\mathcal{R}_g\left(\widetilde{H}\mathbf{r}\right) = \max\left\{\text{rank}\mathcal{R}_g(\widetilde{H}_\mathcal{K}\mathbf{p}) \,:\, \mathbf{p} \in \mathbb{R}^{dn}\right\}$$

where $\widetilde{H}_\mathcal{K} = H_\mathcal{K} \otimes I$ and $H_\mathcal{K}$ is composite incidence matrix for the graph $\mathcal{K}_\mathcal{G}$. Further, if $\mathcal{G}$ has $\text{rank}\mathcal{R}_g\left(\widetilde{H}_\mathcal{G}\mathbf{r}\right)$ edges $(\mathcal{G}, \mathbf{r})$ is *minimally rigid*.

From the inverse function theorem then $w_g^{-1}(w_g(\mathbf{p})) \cap \mathcal{U} \subseteq v_g^{-1}(v_g(\mathbf{p})) \cap \mathcal{U}$.

Infinitesimal rigidity is closely tied to the notion of rigidity in Definition 45. The main result of [87] explored the connection between rigidity and infinitesimal rigidity when the

underlying measurement is the distance measurement. The authors showed that $(\mathcal{G}, \mathbf{r})$ is infinitesimally then $(\mathcal{G}, \mathbf{r})$ is g_D-rigid. The same result can be shown for a generalized measurement $g(\cdot)$.

THEOREM 49. *If a framework $(\mathcal{G}, \mathbf{r})$ infinitesimally g-rigid, then it is g-rigid.*

PROOF. Let $k_{\mathcal{G}} = \text{rank}\mathcal{R}_g\left(\widetilde{H}\mathbf{r}\right)$, $k_{\mathcal{K}} = \text{rank}\mathcal{R}_g(\widetilde{H}_{\mathcal{K}}\mathbf{r})$ and

$$k_{\max} = \max\left\{\text{rank}\mathcal{R}_g(\widetilde{H}_{\mathcal{K}}\mathbf{p}) \,:\, \mathbf{p} \in \mathbb{R}^{dn}\right\}.$$

As $(\mathcal{G}, \mathbf{r})$ is infinitesimally g-rigid then $k_{\mathcal{G}} = k_{\max}$ it follows that as $k_{\mathcal{G}} \leq k_{\mathcal{K}} \leq k_{\max}$ then $\mathbf{r} \in \mathbb{R}^{dn}$ is a a g-regular point of the graph $\mathcal{G}$ and a g-regular point of the graph $\mathcal{K}_{\mathcal{G}}$. From Proposition 47 then $v_g^{-1}\left(v_g\left(\overline{\mathbf{r}}\right)\right) \cap \mathcal{W}_1$ is a $(dn - k_{\mathcal{G}})$-dimensional manifold for some a neighborhood $\mathcal{U}_1$ of $\mathbf{r}$ and similarly if $w_g(\cdot)$ is the measurement function $\mathcal{K}_{\mathcal{G}}$ then $w_g^{-1}\left(w_g\left(\overline{\mathbf{r}}\right)\right) \cap \mathcal{W}_2$ is a $(dn - k_{\mathcal{K}})$-dimensional manifold for some neighborhood $\mathcal{U}_2$of $\mathbf{r}$. The space $w_g^{-1}\left(w_g\left(\overline{\mathbf{r}}\right)\right)$ is always contained in $v_g^{-1}\left(v_g\left(\overline{\mathbf{r}}\right)\right)$, and so $w_g^{-1}\left(w_g\left(\overline{\mathbf{r}}\right)\right) \cap \mathcal{W}$ is a submanifold of $v_g^{-1}\left(v_g\left(\overline{\mathbf{r}}\right)\right) \cap \mathcal{W}$ for $\mathcal{W} = \mathcal{W}_1 \cap \mathcal{W}_2$. As $k_{\mathcal{G}} = k_{\max}$ and $k_{\mathcal{G}} \leq k_{\mathcal{K}} \leq k_{\max}$ then $k_{\mathcal{K}} = k_{\max}$, and so $w_g^{-1}\left(w_g\left(\overline{\mathbf{r}}\right)\right) \cap \mathcal{W}$ and $v_g^{-1}\left(v_g\left(\overline{\mathbf{r}}\right)\right) \cap \mathcal{W}$ are both $(dn - k_{\max})$-dimensional manifolds so for some neighborhood $\mathcal{U} \subseteq \mathcal{W}$ of $\mathbf{r}$ then $w_g^{-1}\left(w_g\left(\overline{\mathbf{r}}\right)\right) \cap \mathcal{U} = v_g^{-1}\left(v_g\left(\overline{\mathbf{r}}\right)\right) \cap \mathcal{U}$, i.e., the framework is g-rigid. □

For multiple measurement types $[g_1, g_2, \cdots, g_p]$ a compositional approach can be adopted to establish rigidity and infinitesimally rigidity.

THEOREM 50. *If $(\mathcal{G}_i, \mathbf{r})$ is g_i-rigid for all $i = 1, \ldots, p$ then $(\bigcup_{i=1}^{p} \mathcal{G}_i, \mathbf{r})$ is $[g_1, g_2, \cdots, g_p]$-rigid. Further, if $(\mathcal{G}_i, \mathbf{r})$ is infinitesimally g_i-rigid and $(\bigcup_{i=1}^{p} \mathcal{K}_i, \mathbf{r})$ is a regular point then $(\bigcup_{i=1}^{p} \mathcal{G}_i, \mathbf{r})$ is infinitesimally $[g_1, g_2, \cdots, g_p]$-rigid.*

PROOF. We show the case for $p = 2$, with the case for larger p following similarly. From Theorem 49 $w_{g_i}^{-1}(w_{g_i}\left(\overline{\mathbf{r}}\right)) \cap \mathcal{U}_i = v_{g_i}^{-1}(v_{g_i}\left(\overline{\mathbf{r}}\right)) \cap \mathcal{U}_i$ for $i = 1$ and 2, hence

$$\begin{aligned} w_{[g_1,g_2]}^{-1}\left(w_{[g_1,g_2]}\left(\overline{\mathbf{r}}\right)\right) \cap \left(\mathcal{U}_1 \cap \mathcal{U}_2\right) &= \left(w_{g_1}^{-1}\left(w_{g_1}\left(\overline{\mathbf{r}}\right)\right) \cap \mathcal{U}_1\right) \cap \left(w_{g_2}^{-1}\left(w_{g_2}\left(\overline{\mathbf{r}}\right)\right) \cap \mathcal{U}_2\right) \\ &= v_{g_1}^{-1}\left(v_{g_1}\left(\overline{\mathbf{r}}\right)\right) \cap \mathcal{U}_1 \cap v_{g_2}^{-1}\left(v_{g_2}\left(\overline{\mathbf{r}}\right)\right) \cap \mathcal{U}_2 \end{aligned}$$

$$= \quad v_{[g_1,g_2]}^{-1}\left(v_{[g_1,g_2]}\left(\overline{\mathbf{r}}\right)\right) \cap \left(\mathcal{U}_1 \cap \mathcal{U}_2\right),$$

and the first rigidity result follows. If $(\mathcal{G}_i, \mathbf{r})$ is infinitesimally g_i-rigid then

$$\text{rank}\mathcal{R}_{g_i}\left(\widetilde{H}_{\mathcal{G}}\mathbf{r}\right) = \text{rank}\mathcal{R}(\widetilde{H}_{\mathcal{K}}\mathbf{r})$$

for $i = 1$ and 2 hence as

$$\text{span}(\mathcal{R}_{g_i}(\widetilde{H}_{\mathcal{G}}\mathbf{r})) \subseteq \text{span}(\mathcal{R}(\widetilde{H}_{\mathcal{K}}\mathbf{r}))$$

then $\text{span}(\mathcal{R}_{g_i}(\widetilde{H}_{\mathcal{G}}\mathbf{r})) = \text{span}(\mathcal{R}(\widetilde{H}_{\mathcal{K}}\mathbf{r}))$. Then,

$$\begin{aligned}
\text{span}\mathcal{R}_{[g_1,g_2]}\left(\widetilde{H}_{\mathcal{G}}\mathbf{r}\right) &= \text{span}\frac{\partial v_{[g_1,g_2]}}{\partial \mathbf{r}}\left(\widetilde{H}_{\mathcal{G}}\mathbf{r}\right) \\
&= \text{span}\left[\begin{array}{cc} \frac{\partial v_{g_1}}{\partial \mathbf{r}}\left(\widetilde{H}_{\mathcal{G}}\mathbf{r}\right) & \frac{\partial v_{g_2}}{\partial \mathbf{r}}\left(\widetilde{H}_{\mathcal{G}}\mathbf{r}\right) \end{array}\right] \\
&= \text{span}\left[\begin{array}{cc} \frac{\partial v_{g_1}}{\partial \mathbf{r}}\left(\widetilde{H}_{\mathcal{K}}\mathbf{r}\right) & \frac{\partial v_{g_2}}{\partial \mathbf{r}}\left(\widetilde{H}_{\mathcal{K}}\mathbf{r}\right) \end{array}\right] \\
&= \text{span}\left[\mathcal{R}_{[g_1,g_2]}\left(\widetilde{H}_{\mathcal{K}}\mathbf{r}\right)\right]
\end{aligned}$$

and $\text{rank}\mathcal{R}_{[g_1,g_2]}\left(\widetilde{H}_{\mathcal{G}}\mathbf{r}\right) = \text{rank}\mathcal{R}_{[g_1,g_2]}\left(\widetilde{H}_{\mathcal{K}}\mathbf{r}\right) = \max\left\{\text{rank}\mathcal{R}_g\left(\widetilde{H}_{\mathcal{K}}\mathbf{p}\right) : \mathbf{p} \in \mathbb{R}^{dn}\right\}$,where the final equality follows from the regularity of the point $\left(\bigcup_{i=1}^{2}\mathcal{K}_i, \mathbf{r}\right)$. The final statement of the theorem follows. □

8.2. Rigidity Based Dynamics

To formulate a control law with the objective of attaining $v_g\left(\overline{\mathbf{r}}\right) = v_g\left(\overline{\mathbf{f}}\right)$ defined over the framework $(\mathcal{G}, \mathbf{r})$, the potential function

$$\begin{aligned}
J(\overline{\mathbf{r}}, \overline{\mathbf{f}}) &= \sum_{i\in p}\sum_{\bar{k}\in E_i}\frac{1}{2}\left\|g_i(r_{\bar{k}}) - g_i(f_{\bar{k}})\right\|^2 \\
&= \frac{1}{2}\left\|v_g\left(\overline{\mathbf{r}}\right) - v_g\left(\overline{\mathbf{f}}\right)\right\|_2^2 \qquad (8.2.1)
\end{aligned}$$

is examined. The function is composed of edges costs $\frac{1}{2}\left\|g_i(r_{\bar{k}}) - g_i(f_{\bar{k}})\right\|^2$ for each measurement type i and edge $\bar{k} \in E_i$ and is zero when the objective is attained and positive otherwise. Adopting a control law in the direction of steepest descent with respect to the

agents state $\mathbf{r}$ of this function then

$$\begin{aligned}\dot{\mathbf{r}} &= -\left(\frac{\partial J}{d\mathbf{r}}\right)^T \\ &= -\left(\frac{\partial J}{\partial v_g}\frac{\partial v_g}{\partial \mathbf{r}}\right)^T \\ &= -\mathcal{R}_g\left(\overline{\mathbf{r}}\right)^T\left(v_g\left(\overline{\mathbf{r}}\right)-v_g\left(\overline{\mathbf{f}}\right)\right). \end{aligned} \tag{8.2.2}$$

The corresponding ith agent dynamics is

$$\dot{r}_i = -\sum_{i\in p}\sum_{\bar{k}\in E_i}\left(g_i(r_{\bar{k}})-g_i(f_{\bar{k}})\right)\frac{\partial g_i(r_{\bar{k}})}{\partial \bar{r}_{\bar{k}}}^T,$$

which can be realized using only local measurement $g_i(r_{\bar{k}})$ and $\frac{\partial g_i(r_{\bar{k}})}{\partial \bar{r}_{\bar{k}}}$. As the cost function is represented in terms of the edge costs it is convenient to analyze this control law as state-dependent edge dynamics using the transform $\overline{\mathbf{r}} = \widetilde{H}\mathbf{r}$, namely

$$\begin{aligned}\dot{\overline{\mathbf{r}}} &= \widetilde{H}\dot{\mathbf{r}} \\ &= -\widetilde{H}\mathcal{R}_g\left(\overline{\mathbf{r}}\right)^T\left(v_g\left(\overline{\mathbf{r}}\right)-v_g\left(\overline{\mathbf{f}}\right)\right)\end{aligned} \tag{8.2.3}$$

where the initial state $\overline{\mathbf{r}}(0) \in \mathrm{Im}\left[\widetilde{H}\right]$. The stability analysis of the problem is then defined with respect to the convergence to the set $\mathcal{E}_{\bar{r}} = \left\{\overline{\mathbf{r}} : v_g\left(\overline{\mathbf{r}}\right) = v_g\left(\overline{\mathbf{f}}\right)\right\}$ which is compact opposed to the agent state space $\mathcal{E}_r = \left\{\mathbf{r} : v_g\left(\widetilde{H}\mathbf{r}\right) = v_g\left(\overline{\mathbf{f}}\right)\right\}$, which contains points that are invariant to translation and so is non-compact. The following theorem estbalishes convergence to the set $\mathcal{E}_{\bar{r}}$.

THEOREM 51. *Under the minimally rigid framework $(\mathcal{G}, \mathbf{f})$, the dynamics (8.2.3) initialized from $\Omega(c) = \left\{\overline{\mathbf{r}}(0) \in Im\left[\widetilde{H}\right] : |J(\overline{\mathbf{r}}, \overline{\mathbf{f}}) < c\right\}$ for sufficiently small c converges exponentially to a point in the set $\mathcal{E}_{\bar{r}}$.*

PROOF. For potential function $J\left(\overline{\mathbf{r}}, \overline{\mathbf{f}}\right)$ is a continuous differentiable function such that $J\left(\overline{\mathbf{r}}, \overline{\mathbf{f}}\right) = 0$ on $\mathcal{E}_{\bar{r}}$ and $J\left(\overline{\mathbf{r}}, \overline{\mathbf{f}}\right) \geq 0$ on $\overline{\mathbf{r}} \in \mathrm{Im}\left[\widetilde{H}\right]$. The derivative of $J\left(\overline{\mathbf{r}}, \overline{\mathbf{f}}\right)$ along the

trajectories of (8.2.3) is given by

$$\begin{aligned}\dot{J}\left(\overline{\mathbf{r}},\overline{\mathbf{f}}\right) &= -\frac{\partial J}{d\overline{\mathbf{r}}}\dot{\overline{\mathbf{r}}} \\ &= -\frac{\partial J}{\partial v_g}\frac{\partial v_g}{\partial \overline{\mathbf{r}}}\widetilde{H}\mathcal{R}_g\left(\overline{\mathbf{r}}\right)^T\left(v_g\left(\overline{\mathbf{r}}\right)-v_g\left(\overline{\mathbf{f}}\right)\right) \\ &= -\left(v_g\left(\overline{\mathbf{r}}\right)-v_g\left(\overline{\mathbf{f}}\right)\right)^T\mathcal{R}_g\left(\overline{\mathbf{r}}\right)\mathcal{R}_g\left(\overline{\mathbf{r}}\right)^T\left(v_g\left(\overline{\mathbf{r}}\right)-v_g\left(\overline{\mathbf{f}}\right)\right).\end{aligned}$$

The derivative $\dot{J}\left(\overline{\mathbf{r}},\overline{\mathbf{f}}\right)$ is non-positive and so $\Omega(c)$ is a compact set that is positively invariant with respect to (8.2.3) for all finite c. Examining the matrix $\mathcal{R}_g\left(\overline{\mathbf{f}}\right)\mathcal{R}_g\left(\overline{\mathbf{f}}\right)^T \in \mathbb{R}^{mp\times mp}$ then as $(\mathcal{G},\mathbf{f})$ is minimally rigid $\text{rank}\mathcal{R}_g\left(\overline{\mathbf{f}}\right)\mathcal{R}_g\left(\overline{\mathbf{f}}\right)^T = \text{rank}(\mathcal{R}_g\left(\overline{\mathbf{f}}\right)) = mp$ and so $\mathcal{R}_g\left(\overline{\mathbf{f}}\right)\mathcal{R}_g\left(\overline{\mathbf{f}}\right)^T$ is positive definite. As the roots of a polynomial vary continuously with its coefficients, the eigenvalues of $\mathcal{R}_g\left(\overline{\mathbf{f}}\right)\mathcal{R}_g\left(\overline{\mathbf{f}}\right)^T$ corresponding to the roots of its characteristic polynomial are continuous. Hence, for c sufficiently small and some $\lambda > 0$, then $\mathcal{R}_g\left(\overline{\mathbf{r}}\right)\mathcal{R}_g\left(\overline{\mathbf{r}}\right)^T \succeq \frac{\lambda}{2}I$ is positive definite for $\overline{\mathbf{r}} \in \Omega(c)$ and so $\dot{J}\left(\overline{\mathbf{r}},\overline{\mathbf{f}}\right) = 0$ only if $\overline{\mathbf{r}} \in \mathcal{E}_{\bar{r}}$. Consequently by La Salle's Theorem [**77**], for for $\overline{\mathbf{r}}(0) \in \Omega(c)$ then $\overline{\mathbf{r}}(t)$ converges to the largest invariant set in $\mathcal{E}_{\bar{r}}$. Further

$$\begin{aligned}\dot{J}\left(\overline{\mathbf{r}},\overline{\mathbf{f}}\right) &\leq -\frac{\lambda}{2}\left\|v_g\left(\overline{\mathbf{r}}\right)-v_g\left(\overline{\mathbf{f}}\right)\right\|_2^2 \\ &= -\lambda\dot{J}\left(\overline{\mathbf{r}},\overline{\mathbf{f}}\right)\end{aligned}$$

and so by the Bellman-Gronwall Lemma [**77**] then $J\left(\overline{\mathbf{r}},\overline{\mathbf{f}}\right) \leq J\left(\overline{\mathbf{r}}\left(0\right),\overline{\mathbf{f}}\right)e^{-\lambda t}$ and so the convergence is exponential to the set $\mathcal{E}_{\bar{r}}$. Finally, as all points in $\mathcal{E}_{\bar{r}}$ correspond to $\dot{\overline{\mathbf{r}}} = \mathbf{0}$ then convergences is to a point in $\mathcal{E}_{\bar{r}}$. □

As with the bearing-compass dynamics, the generalized rigidity dynamics exhibit translation invariance. This is stated formally in the following proposition.

PROPOSITION 52. *The centroid of the dynamics (8.2.2) is invariant.*

PROOF. Examining $\widetilde{H} = H \otimes I$ with $\widetilde{H}(\mathbf{1}\otimes\mathbf{e}_i) = H\mathbf{1}\otimes\mathbf{e}_i = 0$ for $i = 1,\ldots,d$. Hence,

$$\mathbf{1}^T\otimes\mathbf{e}_i^T\dot{\overline{\mathbf{r}}} = \mathbf{1}^T\otimes\mathbf{e}_i^T\widetilde{H}^T\frac{\partial v_g}{\partial\overline{\mathbf{r}}}^T\left(v_g\left(\overline{\mathbf{r}}\right)-v_g\left(\overline{\mathbf{f}}\right)\right)$$

$$= \quad 0,$$

indicating the centroid invariance for each dimension $i = 1, \ldots, d$. □

8.3. Concluding Remarks

Understanding the role of rigidity in formation dynamics is critical to analyzing and controlling formations. To this end, measures on the bearing rigidity matrix were used in Chapters 6 and 7 to favorably select edges and leaders for the bearing-compass dynamics. The final chapter of this part examines a generalized rigidity theory for formation problems. The machinery was shown to produce a broad class of formation distributed controllers applicable for a mixture of different measurement methods between agents in the network.

Final Remarks

CHAPTER 9

Conclusion and Future Work

Concluding Remarks

Concluding remarks are broken into the three respective parts of the dissertation.

Testbed and Supporting Hardware. In this section, we presented a summary of the hardware developed to support the theoretical results presented in this research. A swarm of ground vehicles was developed and exercised on a subset of the protocols explored in the dissertation. With the objective of exploring distributed measurements, a novel agent beacon was developed which can simultaneously perform relative measurements between agents as well as be used a means of distributed communications.

Part I. Analysis of Existing Protocols. This part examined properties of the linear advection dynamics that were suitable for coarse input control. Of particular interest was the invariant features of the dynamics which linked closely to the underlying network topology structure. Simple edge reweighting mechanisms were shown to be effective at coarsely controlling the performance of the dynamics.

We also analyzed the balanced equilibria in the graph Ginzburg-Landau equations and considered the problem of pattern control. Typically a challenging problem due to the nonlinear landscape of the dynamics, we proposed a novel topological rewiring approach to acquire a desired balanced equilibrium. Leveraging the more easily acquirable equilibria over smaller subgraphs, an optimal MDP policy for graph switching was formulated.

Part II. Bearing Measurements and Intuitive Manipulation. In this part, we used a common bearing-only control law applied to many agents in a decentralized network and found several properties of the system that are useful to a human operator. The invariant

properties show that the centroid and scale of an arbitrary system are conserved under unforced dynamics. We have shown that we can manipulate the formation to cause rotations, changes in scale, and change in position using one, two, or all agents. Further, we have demonstrated strong convergence guarantees for both the static and the rotating case.

In this work we examined the leader selection problem for a bearing-compass control law. The criteria for selection were based on the effectiveness of leaders to manipulate the formation's centroid location and scale. The formulation of the problem as the maximization of a monotone increasing submodular function and a relaxed integer program provides methods to efficiently select good leader sets. The effectiveness of these selections was illustrated on a unicycle swarm testbed. The subsequent testbed implementation demonstrated the merits of the proposed selection methods providing good human operator interfaces to the swarm.

Part III. Designing for Bearing Rigidity. In this part, we built on our previous part's exploration of the bearing-based dynamics for formation shape acquisition. The work examined connections between the graph topology and the performance of the dynamics. A bearing rigidity matrix weighted by the edge lengths on the underlying graph was shown to be critical in dictating stability and convergence of the resulting protocol. These connections allowed submodular optimization to be leveraged to select favorable edges based on guaranteeing bearing rigidity and promoting fast convergence. Further, the worst case convergence of the dynamics was examined in relation to the edge weights on the graph and a convex optimization framework was presented to select optimal edge weights.

An anchored version of the dynamics was also presented whereby a subset of the agents, called leaders, had access to bearing measurements to fixed landmarks. Anchored infinitesimally bearing rigidity was proven to be a necessary and sufficient condition for the convergence of the dynamics to a unique formation. The stability and convergence of the anchored dynamics was shown to be dependent on submodular set function on the selected leader agents, proving the greedy leader selection process exhibited close to optimal performance. A similar convex optimization problem to the unanchored case was presented to select optimal edge weights to improve the worst-case convergence of the anchored dynamics. With

the motivation of preserving the formation shape in transients, a state-dependent weighted version of the anchored dynamics was proposed. In support of the dynamic weight selection, anchored bearing simulations demonstrated that the formation shape was more readily preserved compared to fixed edge weights.

On a more general front, the underlying machinery of the bearing-compass dynamics is rigidity theory. The part was concluded with a generalization of this rigidity-based dynamics approach. The newly derived protocols produce a broad class of formation distributed controllers applicable for a mixture of different measurement methods between agents in the network.

Future Work

Testbed and Supporting Hardware. Still outstanding and worthy of future work is the explicit inclusion of the beacon into the testbed implementations. A first step in this direction is to develop a nonlinear Kalman filter to acquire the relative position of agents using the beacon sensors. An attraction of the bearing-compass dynamics is that it can be easily extended to higher dimensions. An expansion of the testbed to include aerial vehicles would allow for a demonstration of the bearing-compass dynamics in 3D. On another front, the specific flavor of the beacon measurements can be used to form rigidity-based dynamics using the approach adopted in Part 3. This presents an interesting research flow whereby the hardware itself generates a novel state-dependent network protocol.

Pattern control without a Lyapunov Potential. The pattern control of the Ginzburg-Landau dynamics, a canonical oscillator dynamics, was investigated in Chapter 2. An attraction is examining these dynamics is that a known global Lyapunov function, formed from the Ginzburg-Landau free energy, was available. The Lyapunov function was then used to find a family of balanced equilibria which became the states of the MDP.

Potential extensions are alternative methods to approximate the transition probability required for the MDP. One promising direction is using the curvature of the dynamics Lyapunov function as an indication of transition directions. Variations of the MDP implementation

can also be explored including robust MDP to accommodate uncertainty in the transition probabilities. This framework shows promise for pattern control in generalized multi-stable dynamics where dimensionality of the dynamics causes difficulties for traditional pattern control techniques.

In general, a global Lyapunov function is challenging to find. One proposed alternative to acquire the equilibria of a nonlinear oscillator dynamics is to build the catalog of equilibrium states as system is probed stochastically to form the MDP transition probabilities. In effect, the sampling information on the regions of attraction simultaneously provides the MDP transition probabilities and MDP states.

We have briefly explored this approach for a system of coupled nanoelectromechanical oscillators, dubbed the NEMs dynamics [**41**], demonstrating its effectiveness without the *a priori* knowledge of a nonlinear landscape of the dynamics via a known Lyapunov function. The dynamics for each oscillator $i \in 1, \ldots, n$

$$\dot{x}_i = -\frac{1}{2}x_i + i\alpha \left|x_i\right|^2 x_i + \frac{1}{2\left|x_i\right|}x_i + i\beta \mathcal{L}_i(\mathcal{G})x.$$

Probing the NEMs dynamics exhibit a rotating limit cycle version of the balanced states found for the Ginzburg-Landau dynamics. The transition probabilities were established in concert with these equilibria with a subset of transition probabilities, displayed in Figure 9.0.1. As with the Ginzburg-Landau dynamics, an optimal transition policy based on these probabilities can be formed. A sample policy which represents a topological switching controller graphically is depicted in Figure 9.0.2a with a sample run appearing in Figure 9.0.2b. The desired state 21 is successfully acquired after 9 actions.

Designing for Rigidity. The state-dependent weights on the anchor edges introduced in the final section of this rigidity work can be considered as a local memory-less feedback approach to preserve the formation scale. A direction of future work is to consider dynamic edge weights based on performance history. The objective would be to have a *learned* formation shape-preservation measure which would be used to inform the weight selection.

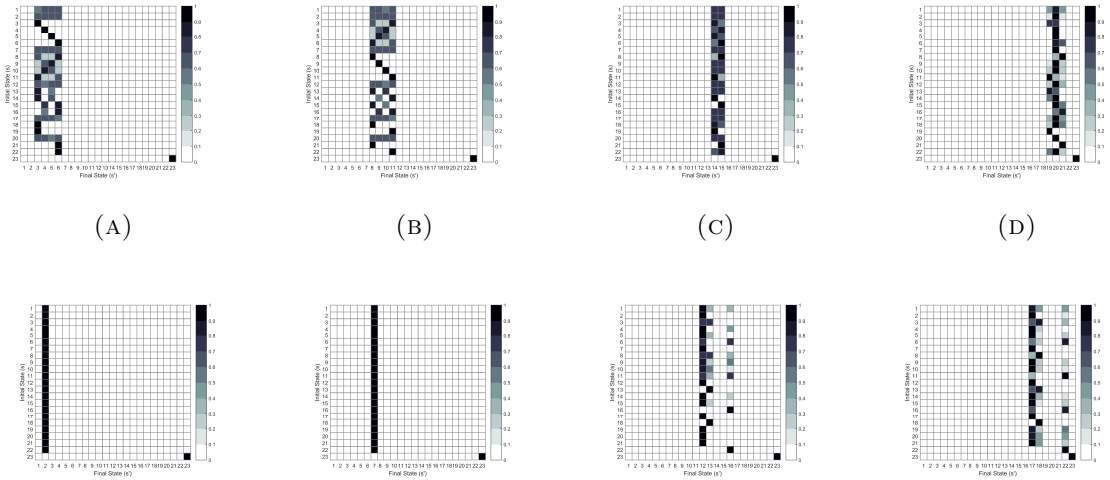

(A) (B) (C) (D)

(E) (F) (G) (H)

FIGURE 9.0.1. Transition probabilities for the NEMs dynamics.

The intersection of learning and local estimation and control presents a fruitful area at the forefront of control and worthy of study.

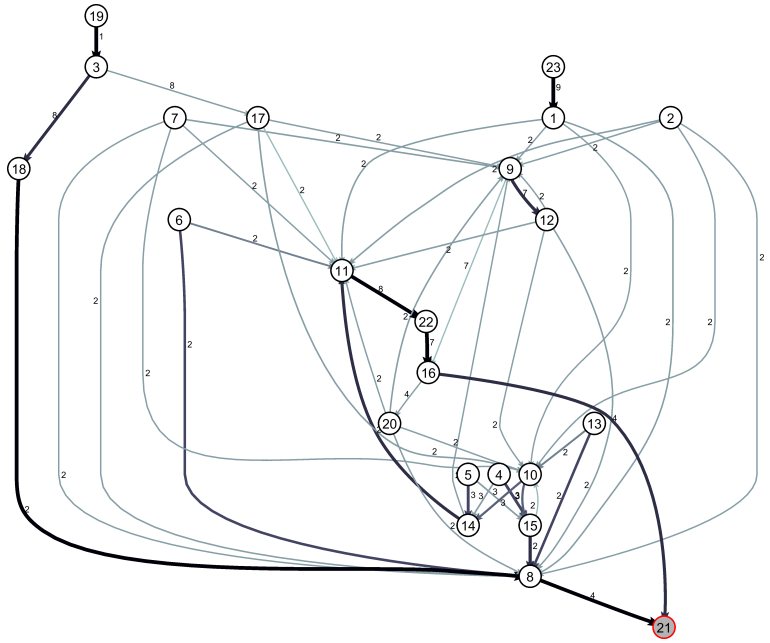

(A)

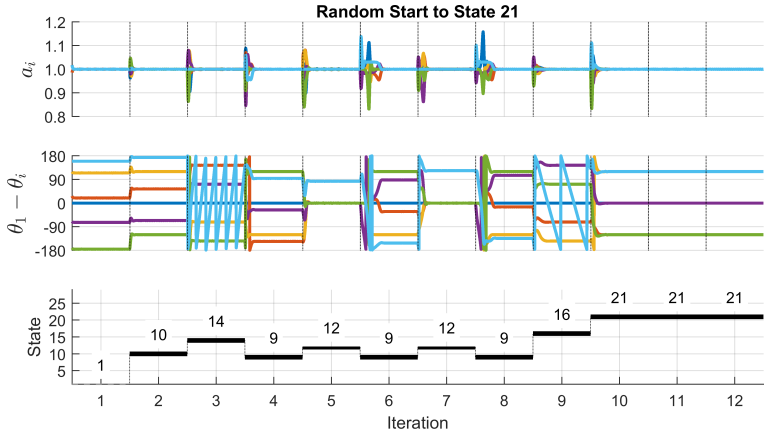

(B)

FIGURE 9.0.2. Given the NEMs dynamics, optimal policy for reaching state 21 from any initial state. A) Transition graph (low probability edges are omitted for clarity) and B) topological switching controller implemented using the optimal policy.

Appendices

APPENDIX A

Bearing Rigidity Matrix Derivation

In this chapter, we present a detailed derivation of the bearing rigidity matrix, defined in §3.1. We start with the definition for the bearing rigidity matrix

$$\mathcal{R}(\Theta) = \frac{\partial \hat{\bar{\mathbf{f}}}}{\partial \mathbf{f}}. \tag{A.1.1}$$

Our first observation is that we can write

$$\frac{\partial \hat{\bar{\mathbf{f}}}}{\partial \mathbf{f}} = \frac{\partial \hat{\bar{\mathbf{f}}}}{\partial \bar{\mathbf{f}}} \frac{\partial \bar{\mathbf{f}}}{\partial \mathbf{f}}. \tag{A.1.2}$$

If we expand $\partial \hat{\bar{\mathbf{f}}} / \partial \bar{\mathbf{f}}$, we get

$$\frac{\partial \hat{\bar{\mathbf{f}}}}{\partial \bar{\mathbf{f}}} = \begin{bmatrix} \frac{\partial \hat{\mathbf{f}}_{\bar{1}}}{\partial \mathbf{f}_{\bar{1}}} & \frac{\partial \hat{\mathbf{f}}_{\bar{1}}}{\partial \mathbf{f}_{\bar{2}}} & \cdots & \frac{\partial \hat{\mathbf{f}}_{\bar{1}}}{\partial \mathbf{f}_{\bar{m}}} \\ \frac{\partial \hat{\mathbf{f}}_{\bar{2}}}{\partial \mathbf{f}_{\bar{1}}} & \frac{\partial \hat{\mathbf{f}}_{\bar{2}}}{\partial \mathbf{f}_{\bar{2}}} & \cdots & \frac{\partial \hat{\mathbf{f}}_{\bar{2}}}{\partial \mathbf{f}_{\bar{m}}} \\ \vdots & \vdots & \ddots & \vdots \\ \frac{\partial \hat{\mathbf{f}}_{\bar{m}}}{\partial \mathbf{f}_{\bar{1}}} & \frac{\partial \hat{\mathbf{f}}_{\bar{m}}}{\partial \mathbf{f}_{\bar{2}}} & \cdots & \frac{\partial \hat{\mathbf{f}}_{\bar{m}}}{\partial \mathbf{f}_{\bar{m}}} \end{bmatrix} \in \mathbb{R}^{dm \times dm},$$

and can observe that $\partial \hat{\mathbf{f}}_{\bar{k}} / \partial \mathbf{f}_{\bar{\ell}} = \mathbf{0}$ for all $k \neq \ell$, and when $k = \ell$, we have

$$\begin{aligned} \frac{\partial \hat{\mathbf{f}}_{\bar{k}}}{\partial \mathbf{f}_{\bar{k}}} &= \frac{1}{\|\mathbf{f}_{\bar{k}}\|} \left(I_d - \hat{\mathbf{f}}_{\bar{k}} \hat{\mathbf{f}}_{\bar{k}}^T \right) \\ &\triangleq \frac{1}{\|\mathbf{f}_{\bar{k}}\|} P_{\bar{k}}. \end{aligned}$$

This means we can write

$$\frac{\partial \hat{\bar{\mathbf{f}}}}{\partial \bar{\mathbf{f}}} = \mathcal{D}_{\bar{k}} \left[\frac{1}{\|\mathbf{f}_{\bar{k}}\|} P_{\bar{k}} \right]. \tag{A.1.3}$$

Similarly, by noting that Eq. (0.2.4) implies that

$$\partial\bar{\mathbf{f}} = \widetilde{H}\partial\mathbf{f},$$

we can write

$$\frac{\partial\bar{\mathbf{f}}}{\partial\mathbf{f}} = \widetilde{H}. \tag{A.1.4}$$

Thus, we can write the bearing rigidity matrix in Eq. (A.1.1) using Eqs. (A.1.3) and (A.1.4) as

$$\mathcal{R}(\Theta) = \mathcal{D}_{\bar{k}}\left[\frac{1}{\|\mathbf{f}_{\bar{k}}\|}P_{\bar{k}}\right]\widetilde{H}.$$

Now, observe that $P_{\bar{k}}$ and $\widetilde{H}$ are independent of the scale of the formation, i.e. they only depend on the structure of the formation $\hat{\mathbf{f}}_{\bar{k}}$ rather than particular edge lengths $\mathbf{f}_{\bar{k}}$. As such, we can write the bearing rigidity matrix as

$$\begin{aligned}\mathcal{R}(\Theta) &= \mathcal{D}_{\bar{k}}\left[\frac{1}{\|\mathbf{f}_{\bar{k}}\|}I_d\right]\mathcal{D}_{\bar{k}}\left[P_{\bar{k}}\right]\tilde{H} \\ &\triangleq M\widetilde{\mathcal{R}}.\end{aligned}$$

Bibliography

[1] R. Olfati-Saber and R. M. Murray, "Distributed cooperative control of multiple vehicle formations using structural potential functions," in *IFAC World Congress*, 2002.

[2] M. Mesbahi and M. Egerstedt, *Graph Theoretic Methods in Multiagent Networks*. Princeton, New Jersey: Princeton University Press, 2010.

[3] R. Olfati-Saber and R. M. Murray, "Graph rigidity and distributed formation stabilization of multi-vehicle systems," in *IEEE Conference on Decision and Control*, 2002, pp. 2965–2971.

[4] N. Moshtagh, A. Jadbabaie, and K. Daniilidis, "Distributed coordination of dynamic rigid bodies," in *IEEE Conference on Decision and Control*, 2007, pp. 1480–1485.

[5] F. Dörfler and B. Francis, "Formation control of autonomous robots based on cooperative behavior," in *European Control Conference*, 2009, pp. 2432–2437.

[6] M. Basiri, A. N. Bishop, and P. Jensfelt, "Distributed Control of Triangular Formations with Angle-Only Constraints," *Systems & Control Letters*, vol. 59, no. 2, pp. 147–154, 2010.

[7] E. Schoof, A. Chapman, and M. Mesbahi, "Efficient leader selection for translation and scale of a bearing-compass formation," in *IEEE International Conference on Robotics and Automation*, 2015, pp. 1816–1821.

[8] F. Schiano, A. Franchi, D. Zelazo, and P. R. Giordano, "A rigidity-based decentralized bearing formation controller for groups of quadrotor UAVs," in *IEEE/RSJ International Conference on Intelligent Robots and Systems*, 2016, pp. 5099–5106.

[9] Y. Wan, S. Roy, and A. Saberi, "Network design problems for controlling virus spread," in *IEEE Conference on Decision and Control*, 2007, pp. 3925–3932.

[10] A. Chapman, E. Schoof, and M. Mesbahi, "Distributed online topology design for network-level disturbance rejection," in *IEEE Conference on Decision and Control*, 2013, pp. 817–822.

[11] D. Zelazo and M. Mesbahi, "Edge Agreement: Graph-Theoretic Performance Bounds and Passivity Analysis," *IEEE Transactions on Automatic Control*, vol. 56, no. 3, pp. 544–555, 2011.

[12] S. Boyd, "Convex optimization of graph Laplacian eigenvalues," *Proceedings of the International Congress of Mathematicians*, vol. 3, pp. 1311–1319, 2006.

[13] S. Patterson and B. Bamieh, "Leader selection for optimal network coherence," *IEEE Conference on Decision and Control*, pp. 2692–2697, 2010.

[14] A. Clark and R. Poovendran, "A submodular optimization framework for leader selection in linear multi-agent systems," in *IEEE Conference on Decision and Control*, 2011, pp. 3614–3621.

[15] F. Lin, M. Fardad, and M. R. Jovanović, "Algorithms for Leader Selection in Stochastically Forced Consensus Networks," *IEEE Transactions on Automatic Control*, vol. 59, no. 7, pp. 1789–1802, 2014.

[16] N. Michael, M. M. Zavlanos, V. Kumar, and G. J. Pappas, "Distributed Multi-Robot Task Assignment and Formation Control," *2008 IEEE International Conference on Robotics and Automation*, vol. 1, pp. 128–133, may 2008.

[17] H. Kawashima and M. Egerstedt, "Leader Selection via the Manipulability of Leader-Follower Networks," *2012 American Control Conference*, pp. 6053–6058, jun 2012.

[18] A. Chapman and M. Mesbahi, "Semi-autonomous consensus: network measures and adaptive trees," *IEEE Transactions on Automatic Control*, vol. 58, no. 1, pp. 19–31, 2013.

[19] G. L. Nemhauser, L. A. Wolsey, and M. L. Fisher, "An Analysis of Approximations for Maximizing Submodular Set Functions I," *Mathematical Programming*, vol. 14, pp. 265–294, 1978.

[20] L. Lovász, "Submodular Functions and Convexity," in *Mathematical Programming The State of the Art*. Berlin: Springer, 1983, pp. 235–257.

[21] T. H. Summers, F. L. Cortesi, and J. Lygeros, "On Submodularity and Controllability in Complex Dynamical Networks," *IEEE Transactions on Control of Network Systems*, vol. 3, no. 1, pp. 91–101, 2016.

[22] A. Clark, B. Alomair, L. Bushnell, and R. Poovendran, *Submodularity in Dynamics and Control of Networked Systems*. Springer International Publishing, 2016.

[23] I. Shames and T. H. Summers, "Rigid Network Design via Submodular Set Function Optimization," *IEEE Transactions on Network Science and Engineering*, vol. 2, no. 3, pp. 84–96, 2015.

[24] R. A. Horn and C. R. Johnson, *Matrix Analysis*. New York: Cambridge University Press, 1990.

[25] A. Berman and R. J. Plemmons, *Nonnegative Matrices in the Mathematical Sciences*. Academic Press, 1979.

[26] A. Chapman and M. Mesbahi, "Advection on graphs," in *Proc. 50th IEEE Conference on Decision and Control*, 2011, pp. 1461 – 1466.

[27] D. A. Paley, N. E. Leonard, R. Sepulchre, D. Grunbaum, and J. K. Parrish, "Oscillator models and collective motion," *IEEE Control Systems Magazine*, vol. 27, no. 4, pp. 89–105, 2007.

[28] F. Dörfler and F. Bullo, "Synchronization and transient stability in power networks and nonuniform Kuramoto oscillators," *SIAM Journal on Control and Optimization*, vol. 50, no. 3, pp. 1616–1642, 2012.

[29] D. B. Rodrigues, P. R. Silva, G. B. Lima, E. A. A. Coelho, and L. C. G. Freitas, "Grid Connected DC Distribution Network Deploying High Power Density Rectifier for DC Voltage Stabilization," in *IEEE Applied Power Electronics Conference and Exposition*, 2016, pp. 3585–3590.

[30] T. Pereira, "Stability of Synchronized Motion in Complex Networks," *arXiv preprint arXiv:1112.2297*, 2011.

[31] M. C. Cross and P. C. Hohenberg, "Pattern formation outside of equilibrium," *Rev. Mod. Phys.*, vol. 65, no. 3, pp. 851–1112, 1993.

[32] A. N. Pisarchik and U. Feudel, "Control of multistability," *Physics Reports*, vol. 540, no. 4, pp. 167–218, 2014.

[33] S. Boccaletti, J. Bragard, and F. T. Arecchi, "Controlling and synchronizing space time chaos," *Physical Review E*, vol. 59, no. 6, pp. 6574–6578, 1999.

[34] S. P. Cornelius, W. L. Kath, and A. E. Motter, "Realistic control of network dynamics," *Nature Communications*, vol. 4, p. 1942, 2013.

[35] L. Krick, M. E. Broucke, and B. A. Francis, "Stabilization of infinitesimally rigid formations of multi-robot networks," in *IEEE Conference on Decision and Control*, 2008, pp. 477–482.

[36] N. Moshtagh, N. Michael, A. Jadbabaie, and K. Daniilidis, "Vision-Based, Distributed Control Laws for Motion Coordination of Nonholonomic Robots," *IEEE Transactions on Robotics*, vol. 25, no. 4, pp. 851–860, 2009.

[37] A. N. Bishop, I. Shames, and B. D. O. Anderson, "Stabilization of rigid formations with direction-only constraints," in *IEEE Conference on Decision and Control and European Control Conference*, 2011, pp. 746–752.

[38] A. Franchi and P. R. Giordano, "Decentralized control of parallel rigid formations with direction constraints and bearing measurements," in *IEEE Conference on Decision and Control*, 2012, pp. 5310–5317.

[39] S. Zhao and D. Zelazo, "Bearing Rigidity and Almost Global Bearing-Only Formation Stabilization," *IEEE Transactions on Automatic Control*, vol. 61, no. 5, pp. 1255–1268, 2016.

[40] A. Huster, E. Frew, and S. Rock, "Relative position estimation for AUVs by fusing bearing and inertial rate sensor measurements," in *Oceans '02 MTS/IEEE*, 2002, pp. 1863–1870.

[41] J. Emenheiser, A. Chapman, M. Pósfai, J. P. Crutchfield, M. Mesbahi, and R. M. D'Souza, "Patterns of patterns of synchronization: Noise induced attractor switching in rings of coupled nonlinear oscillators," *Chaos*, vol. 26, no. 9, 2016.

[42] E. Schoof, A. Chapman, and M. Mesbahi, "Bearing-compass formation control: A human-swarm interaction perspective," in *American Control Conference*, 2014, pp. 3881–3886.

[43] S. Zhao and D. Zelazo, "Bearing rigidity and almost global bearing-only formation stabilization," *IEEE Transactions on Automatic Control*, vol. 61, no. 5, pp. 1255–1268, 2015.

[44] F. L. Cortesi, T. H. Summers, and J. Lygeros, "Submodularity of Energy Related Controllability Metrics," in *Proc. 54th IEEE Conference on Decision and Control*, 2014, pp. 2883 – 2888.

[45] A. N. Bishop, T. H. Summers, and B. D. O. Anderson, "Control of triangle formations with a mix of angle and distance constraints," in *IEEE International Conference on Control Applications*, 2012, pp. 825–830.

[46] G. L. Mariottini, F. Morbidi, S. Member, N. V. Valk, and G. Pappas, "Vision-Based Localization for Leader-Follower Formation Control," *IEEE Transactions on Robotics*, vol. 25, no. 6, pp. 1431–1438, 2009.

[47] E. Schoof, A. Chapman, and M. Mesbahi, "Weighted Bearing-Compass Dynamics : Edge and Leader Selection (submitted)," *IEEE Transactions on Network Science and Engineering*.

[48] A. Chapman, E. Schoof, and M. Mesbahi, "Advection on networks with an application to decentralized load balancing," *IEEE/RSJ International Conference on Intelligent Robots and Systems*, no. 2, pp. 2680–2681, oct 2012.

[49] A. Chapman, "Semi-Autonomous Networks : Effective Control of Networked Systems through Protocols, Design, and Modeling," PhD Thesis, University of Washington, 2013.

[50] R. J. Vasil, "Distributed Channel Assignment Using a Modified ALOHA Protocol," Masters Thesis, University of Washington, 2015.

[51] W. Howerton, "Cosine Kuramoto Based Distribution of a Convoy with Limit-Cycle Obstacle Avoidance Through the Use of Simulated Agents," Masters Thesis, University of Washington, 2016.

[52] G. Dudek, M. Jenkin, E. Milios, and D. Wilkes, "A taxonomy for swarm robots," *Proceedings of 1993 IEEE/RSJ International Conference on Intelligent Robots and Systems (IROS '93)*, vol. 1, no. C, pp. 441–447, 1993.

[53] G. Capi, G. Pojani, and S. I. Kaneko, "Evolution of task switching behaviors in real mobile robots," *3rd International Conference on Innovative Computing Information and Control, ICICIC'08*, pp. 8–11, 2008.

[54] M. Bonani, V. Longchamp, S. Magnenat, P. Rï¿œetornaz, D. Burnier, G. Roulet, F. Vaussard, H. Bleuler, and F. Mondada, "The MarXbot, a Miniature Mobile Robot Opening new Perspectives for the Collective robotic Research," *International Conference on Intelligent Robots and Systems, IROS, Taiwan*, pp. 4187–4193, 2010.

[55] M. Rubenstein, C. Ahler, and R. Nagpal, "Kilobot: A low cost scalable robot system for collective behaviors," *Proceedings - IEEE International Conference on Robotics and Automation*, pp. 3293–3298, 2012.

[56] R. Murray and S. Sastry, "Nonholonomic motion planning:steering using sinusoids," *IEEE Trans. on Automatic Control*, vol. 38, no. 5, pp. 700–716, 1993.

[57] M. Aicardi, G. Casalino, A. Bicchi, and A. Balestrino, "Closed Loop Steering of Unicycle-like Vehicles via Lyapunov Techniques," *IEEE Robotics & Automation Magazine*, no. March, pp. 27–35, 1995.

[58] H. G. Tanner, G. J. Pappas, and V. Kumar, "Leader-to-Formation Stability," *IEEE Transactions on Robotics and Automation*, vol. 20, no. 3, pp. 443–455, jun 2004.

[59] S. Berman, A. Halasz, M. A. Hsieh, and V. Kumar, "Optimized Stochastic Policies for Task Allocation in Swarms of Robots," *IEEE Transactions on Robotics*, vol. 25, no. 4, pp. 927–937, 2009.

[60] M. Pavone, S. Smith, and E. Frazzoli, "Load balancing for mobility-on-demand systems," in *Proceedings of Robotics: Science and Systems*, 2011.

[61] B. P. Gerkey and M. J. Mataric, "A formal analysis and taxonomy of task allocation in multi-robot systems," *International Journal of Roboitcs Research*, vol. 23, no. 9, pp. 939–954, 2004.

[62] J. Mclurkin and D. Yamins, "Dynamic Task Assignment in Robot Swarms," in *Robotics Science and Systems*, 2005.

[63] A. Kashyap, T. Basar, and R. Srikant, "Quantized consensus," *Automatica*, vol. 43, no. 7, pp. 1192–1203, jul 2007.

[64] F. A. Rodrigues, T. K. D. Peron, P. Ji, and J. Kurths, "The Kuramoto model in complex networks," *Phys. Rep.*, vol. 610, pp. 1–98, 2016.

[65] J. A. Rogge and D. Aeyels, "Stability of phase locking in a ring of unidirectionally coupled oscillators," *Journal of Physics A: Mathematical and General*, vol. 37, no. 46, pp. 11 135–11 148, 2004.

[66] X. Zhihao, M. Egerstedt, G. Droge, and K. Schilling, "Balanced deployment of multiple robots using a modified Kuramoto model," in *American Control Conference*, 2013, pp. 6138–6144.

[67] W. van Saarloos and P. Hohenberg, "Fronts, pulses, sources and sinks in generalized complex Ginzburg-Landau equations," *Physica D: Nonlinear Phenomena*, vol. 56, no. 4, pp. 303–367, 1992.

[68] A. Alonso, O. Batiste, and I. Mercader, "Numerical simulations of binary fluid convection in large aspect ratio annular containers," *European Physical Journal: Special Topics*, vol. 146, no. 1, pp. 261–277, 2007.

[69] P. Coullet, L. Gil, and F. Rocca, "Optical vortices," *Optics Communications*, vol. 73, no. 5, pp. 403–408, 1989.

[70] T. Leweke and M. Provansal, "Model for the transition in bluff body wakes," *Physical Review Letters*, vol. 72, no. 20, pp. 3174–3177, 1994.

[71] Y. Kuramoto and S. Koga, "Turbulized Rotating Chemical Waves," *Progress of Theoretical Physics*, vol. 66, no. 3, pp. 1081–1085, 1981.

[72] A. L. Bertozzi and A. Flenner, "Diffuse Interface Models on Graphs for Classification of High Dimensional Data," *Multiscale Modeling & Simulation*, vol. 10, no. 3, pp. 1090–1118, 2012.

[73] M. L. Puterman, Ed., *Markov Decision Processes: Discrete Stochastic Dynamic Programming*. NJ, USA: John Wiley & Sons, Inc., 1994.

[74] E. A. Feinberg and A. Shwartz, Eds., *Handbook of Markov Decision Processes: Methods and Applications*. Boston, MA: Springer US, 2002, vol. 40.

[75] R. Sepulchre, D. Paley, and N. Leonard, "Group Coordination and Cooperative Control of Steered Particles in the Plane," in *Group Coordination and Cooperative Control*. Berlin/Heidelberg: Springer-Verlag, 2013, vol. 53, no. 9, pp. 217–232.

[76] M. Egerstedt and X. Hu, "Formation Constrained Multi-Agent Control," *IEEE Transactions on Robotics and Automation*, vol. 17, no. 6, pp. 3961–3966, 2001.

[77] H. K. Khalil, *Nonlinear Systems*. Prentice Hall, 2002.

[78] T. Eren, W. Whiteley, A. Morse, P. Belhumeur, and B. Anderson, "Sensor and network topologies of formations with direction, bearing, and angle information between agents," in *IEEE Conference on Decision and Control*, 2003, pp. 3064–3069.

[79] M. R. Garey and D. S. Johnson, *Computers and Intractability: A Guide to the Theory of NP-Completeness*, 1979.

[80] K. R. Guruprasad and P. Dasgupta, "Distributed Voronoi partitioning for multi-robot systems with limited range sensors," in *IEEE International Conference on Intelligent Robots and Systems*, 2012, pp. 3546–3552.

[81] J. Stergiopoulos and A. Tzes, "Convex Voronoi space-partitioning for coverage purposes in heterogeneous sensor networks," in *European Control Conference*, 2009, pp. 2361–2366.

[82] H. H. Bauschke, O. Güler, A. S. Lewis, and H. S. Sendov, "Hyperbolic polynomials and convex analysis," *Canadian Journal of Mathematics*, vol. 53, no. 3, pp. 470–488, 2001.

[83] J. Khalife, K. Shamaei, and Z. M. Kassas, "A software-defined receiver architecture for cellular CDMA-based navigation," in *Position, Location and Navigation Symposium*, 2016, pp. 816–826.

[84] Z. Sun, U. Helmke, and B. D. O. Anderson, "Rigid formation shape control in higher dimensions : an invariance principle and open problems," *IEEE Conference on Decision and Control*, pp. 6095–6100, 2015.

[85] J. M. Hendrickx, B. D. O. Anderson, J. C. Delvenne, and V. D. Blondel, "Directed graphs for the analysis of rigidity and persistence in autonomous agent systems," *International Journal of Robust and Nonlinear Control*, vol. 17, no. 10-11, pp. 960–981, 2007.

[86] L. Asimow and B. Roth, "The Rigidity of Graphs," *Transactions of the American Mathematical Society*, vol. 245, pp. 279–289, 1978.

[87] ——, "The Rigidity of Graphs II," *Journal of Mathematical Analysis and Applications*, vol. 68, pp. 171–190, 1979.